Syracuse University

SURFACE

Dissertations - ALL

SURFACE

August 2020

Investigating the Relationships Between Disorder, Structure, and Dynamics in Amorphous Systems

Ethan Stanifer
Syracuse University

Follow this and additional works at: https://surface.syr.edu/etd

Part of the Physical Sciences and Mathematics Commons

Recommended Citation

Stanifer, Ethan, "Investigating the Relationships Between Disorder, Structure, and Dynamics in Amorphous Systems" (2020). *Dissertations - ALL*. 1275.
https://surface.syr.edu/etd/1275

This Dissertation is brought to you for free and open access by the SURFACE at SURFACE. It has been accepted for inclusion in Dissertations - ALL by an authorized administrator of SURFACE. For more information, please contact surface@syr.edu.

ABSTRACT

In this thesis, we investigate the relationships between the disorder, structure, and deformation in amorphous materials. First, to understand the surprising low-frequency vibrational modes in structural glasses, and how it arises from the microscopic disorder in the system, we study the spectra of a large ensemble of sparse random matrices where disorder is controlled by the distribution of bond weights and network coordination. When there is a finite probability density of infinitesimal bond weights, we find a region in the vibrational density of states that is consistent with the low-frequency behavior in structural glasses. Next, in order to investigate structural properties of active systems, we develop a novel method to generate static, finite packings in an artificial potential that reproduce the packing structures observed in a class of point-of-interest active self-propelled particle simulations. This allows us to compute structural measures, such as the vibrational modes, in an unstable active system. Finally, we evaluate the evolution of structure during strain-induced avalanches in athermal, amorphous systems using numerical simulation of soft spheres. We find that these avalanches can be decomposed into a series of bursts of localized deformations, and we develop an extension of persistent homology to isolate these bursts of localized deformations. Further, we extend existing tools for the structural evaluation of mechanically stable systems to generically unstable systems to identify how soft regions evolve and change throughout an avalanche.

INVESTIGATING THE RELATIONSHIPS BETWEEN DISORDER, STRUCTURE, AND DYNAMICS IN AMORPHOUS SYSTEMS

BY

Ethan Stanifer

B.S., Miami University, 2013
B.S., Miami University, 2013
B.A., Miami University, 2013
M.S., Syracuse University, 2016

Dissertation
Submitted in partial completion of the requirements
for the degree of
Doctor of Philosophy in Physics.

Syracuse University
August 2020

Copyright © Ethan Stanifer 2020
All Rights Reserved

Acknowledgements

I would like to first thank my advisor, Lisa Manning, whose continued support and guidance has been invaluable throughout my PhD. Thinking scientifically is a difficult art to master and I am grateful for Lisa's mentorship as I worked to improve my skills. Her experience and insight have been a constant help in completing my research goals.

I am grateful to Peter Morse, Edan Lerner, and Alan Middleton for their helpful perspectives and advice throughout the development of the research I have conducted during my time at Syracuse University. I'm also thankful to Larne Pekowsky and the Research Computing Team at Syracuse University for their constant technical support and ingenious solutions to a host of computational problems.

I would like to thank my coworkers and fellow members of the Manning Research Group: Sven Wijtams, Michael Czajkowski, Guiseppe Passucci, Preeti Sahu, Elizabeth Lawson-Keister, Julia Giannini, David Richard, Sudeshna Roy, Varda Faghir Hagh, and Amanda Parker. Thank you for your encouragement and friendship; you've all been fun to be around.

I would also like to thank my committee members – James Henderson, Jennifer Ross, Christian Santangelo, Alison Patteson, and Jennifer Schwarz – for taking time out of their schedules to serve on my thesis defense committee.

To my wife, my parents, and our entire family: I've only been able to make it this far because of you're constant help and support. Thank you for everything.

In the current state of the world, I feel it is important to take this opportunity to state self-evident truths: black lives matter, trans rights are human rights, and no human is illegal.

Contents

List of Figures viii

List of Tables xiv

1 Introduction 1

1.1 Definition of glass and disordered solids 1

1.1.1 Historical definitions 1

1.1.2 Thermodynamics of disordered systems 2

1.1.3 Structure of glassy materials 3

1.1.4 Potential energy landscape 6

1.1.5 Constraint counting 8

1.2 Applications of glass and jamming physics 10

1.3 Dynamics and material properties of disordered materials 12

1.3.1 Examples of amorphous system dynamics 12

1.3.2 Phenomenology of materials under applied shear 14

1.3.3 Linear response and vibrational modes 18

1.3.4 Thesis outline 23

1.4 Additional Work 26

1.4.1 Predicting failure in disordered solids from structural metrics 26

1.4.2 Jammed packings behave similarly under random forcing and shear . 28

2 A simple random matrix model for the vibrational spectrum of jammed packings **31**

2.1 Introduction 31
2.2 Model 32
2.3 Finite size scaling of weighted ring 34
2.4 Crossbonded ring with unifrom bond weights 35
2.5 Crossbonded ring with power-law bond weights 40
2.6 Discussion 41
2.A Extremal statistics in the two-regular graph 44
  2.A.1 Power-law distribution 46
2.B Extremal statistics in the two-regular graph with additional bonds 47
  2.B.1 Distribution of bounded regions 47
  2.B.2 Crossbonded spectrum 49
  2.B.3 Full spectrum 50
  2.B.4 Behavior of sloshing modes 51

3 A self-propelled particle model for collective motion in dynamic crowds 53

3.1 Introduction 53
3.2 Model 57
3.3 Symmetry-broken active particle simulations form static packings 59
3.4 Modified linear response in an external potential 60
3.5 Structural gradients of static crowds 63
3.6 Gradients in thermalized active packings 66
3.7 Continuing work 68
3.8 Discussion 69

4 Avalanche dynamics in athermal systems 72

4.1 Introduction 72

4.2 Model 78

4.3 Plastic motion in avalanches occurs in bursts 80

4.4 Avalanches can be decomposed into bursts of localized deformation 83

4.5 Effective linear response in unstable systems 88

4.6 The lowest “vibrational” modes change rapidly throughout minimization . . 92

4.7 Soft spots evolve during avalanches 97

4.8 Dynamic soft spots correlate with bursts of localized deformation 99

4.9 Discussion 102

5 Future directions 105

References 108

Vita 126

List of Figures

1 The volume, v, or enthalpy, h, of a liquid at constant pressure as a function of temperature T. T_m denotes the melting temperature of the crystalline solid. T_{ga} and T_{gb} denote the glass transition temperatures for a slow and fast cooling rate respectively. [4] 2

2 a) X-ray diffraction patterns of vapor-deposited CO_2 glass measured at 3 K. The red and black curves represent the glass as deposited and the glass annealed at 90 K respectively. Vertical tick marks show the peak position of crystalline CO_2. b) Pair distribution for glassy, liquid, and crystalline forms of CO_2 [8]. 4

3 Schematic representation of the energy landscape of a glassy system where the x-axis is representative of configurations of particles in the glassy system. [4] 7

4 The phase diagram for soft sphere particles. The axes are nondimensionalized parameters: temperature ($T/p\sigma^3$), stress (Σ/p), and pressure ($p\sigma^3/\epsilon$), where T is temperature, p is pressure, σ is the diameter of hard spheres, Σ is the shear stress, and ϵ is the interaction energy scale [18]. 10

5 a) The phase diagram for confluent tissues as a function of cell motility, v_0, and target shape index, p_0, in the self-propelled Voronoi model for cells. b) Examples of the fluid and solid states of the self-propelled Voronoi and the trajectories of the particles. Note the solid state particles move very little [19]. 11

6 Tensile yield strength of various materials vs the elastic strain-to-failure limit. Bulk Metallic Glasses, Glassy Alloys, are stronger and more resistant to plastic deformation than their crystalline counterparts like steels [23]. 13

7 Yielding in a mean-field elasto-plastic model. Stress, $\langle\sigma\rangle$, vs strain, γ, for increasing degree of annealing, A, from bottom to top. The lowest annealing has a smooth transformation that transitions into a smooth stress overshoot and continues to transition to a discontinuous transition. (Inset) The magnitude of the discontinuous stress drop, $\Delta\langle\sigma\rangle$, as a function of the degree of annealing. Low values of A indicate large annealing [29]. 16

8 a) Schematic of three distributions, $P_0(x)$, of stress to instability, x, for elements in an elastoplastic model for 1) a poorly annealed glass, 2) a moderately annealed glass, and 3) a well annealed glass. b) Stress versus strain curves for these three distributions of initial stabilities. c) Snapshots of the plastic strain during the yielding transition indicated by red circles. 18

9 a) DOS for N = 8192 in d = 3 to 7, averaged over 30 to 50 configurations of soft sphere packings in high dimensions agree with the infinite-dimensional result of $D(\omega) \propto \omega^2$ in the low frequency regime [38]. b) The same DOS for higher pressures. Detailed simulations over thousands of configurations in two- (c), three- (d), and four- (e) dimensional systems find ω^4 scaling for the lowest vibrational modes [39]. 20

10 Log-log representation of the simulated density of states for a cubic lattice of coupled, randomly-oriented oscillators. The arrows indicate the two characteristic frequencies ω_b, the boson peak, and ω_c, the frequency above which the system returns to ω^2 scaling [43]. 22

11 The rescaled density of states, $D(\omega')$, for the two-regular graph with N=16, 64, 256, 1024, and 4096 and $\alpha = 0$, normalized by system size, N, averaged over at least 10^6 matrices. The analytic prediction for the low-frequency scaling is shown as the black dashed line. In the upper-left we have a sketch of a 1d chain with periodic boundary conditions (the open circles are the same node) **Inset:** Unscaled density of states, $D(\omega)$. 34

12 The density of states for fixed system size (N=1000) and changing $\delta z = 0.1, 0.168, 0.282, 0.476, 0.8$ In the upper-left we have a sketch of a 1d chain with periodic boundary conditions (the open circles are the same node) with additional bonds. **Inset:** The density of states, $D(\omega)$, for fixed $\delta z = 0.1$ and changing system size N = 20, 60, 120, 240, 500, 1000, 2000, and 4000. . . . 36

13 **a)**The density of states, $D(\omega)$, rescaled by δz. The blue dashed line indicates the transition from the ω^3 regime to the ω^4 regime while the black dashed line indicates the transition to the plateau. The inset shows the scaling of ω^* and ω_e with δz is linear. **b)**The inverse participation ratio, IPR, rescaled by δz. The IPR approaches a quasilocalized plateau in the ω^3 region. 38

14 The density of states for $\alpha = -0.4, -0.2, 0, 0.25, 0.5, 1$, and 2, with $\delta z = 0.1$. **Inset:** $D(\omega' = A\omega^{4\alpha+3})$ for the same values of α as in the main figure, where A is the coefficient predicted in Appendix B. The black dashed line is the predicted scaling for the low frequency regime. 40

15 A ring or periodic 1d spring system with the two weakest bonds highlighted as springs. 44

16 A sketch of a crossbonded network with 56 particles and 7 crossbonds. The green arrows delineate the regions between crossbonds where 2 edges can disconnect the network. The red arrows point out edges that can't disconnect the network. The yellow arrows point out sets of edges that would disconnect the network that aren't between crossbonded nodes. 48

17 The BIPR rescaled by δz. The blue dashed line indicates ω_e while the black dashed line indicates ω^* 51

18 Snapshots of a crowd as it forms over time are shown in A, B, C, and D. E) The maximum unbalanced force in a simulation over time. The red shapes indicate the times at which each corresponding snapshot of the crowd was taken. 59

19 A) Pressure on members of the crowd as a function of radius averaged of 15 crowds. B) A sketch of the pressure in an example crowd. C) Vibrability on members of the crowd as a function of radius averaged of X crowds. D) A sketch of the vibrability in an example crowd. E) Non-affine vibrability on members of the crowd as a function of radius averaged of 15 crowds. F) A sketch of the non-affine vibrability in an example crowd. 64

20 A) The mean squared displacement at 10 τ as a function of radius for 6 different effective temperatures. B, C, and D are snapshots of a thermally active crowd at 10 τ at effective temperatures 6.6125, 1.8 and 0.1125 respectively. 66

21 Snapshots of the D^2_{min} field over time are shown in A, B, and C. D) The maximum D^2_{min} as a function of time for an example avalanche. Red symbols indicate the times at which the snapshots were extracted. 82

22 A) A portion of the persistent clustering tree diagram for a single avalanche. The y-coordinate indicates the D^2_{min} value at which the cluster forms. The clusters are colored by their volume. B) The mutual information between the clusters identified at different volume thresholds. 85

23 A) The clusters identified by the persistent clustering analysis in one example. B) The plot of the maximum D^2_{min} over time highlighting the D^2_{min} of each cluster in A. 86

24 A) The distribution of the size of the identified bursts of localized deformation in 100 avalanches. The dashed line shows a log normal distribution. B) The distribution of the duration of bursts of localized deformation. The dashed line shows a lognormal distribution with the same mean and standard deviation as the duration histogram. C) The relationship between the duration and the size of the burst of localized deformation identified in 100 avalanches. The dashed line shows the threshold for the spacetime volume of the clustering algorithm. 87

25 A) The lowest 10 eigenvalues of the Hessian as a function of time for a single avalanche simulation. B) The number of eigenvalues below zero as a function of time. 93

95

27 A) The average maximum correlation for each burst of localized deformation as a function of the volume threshold. B) A spacetime plot highlighting the localized soft spots found by clustering on the softness field over time for a volume threshold of 1000. Note the x- and y-directions in this system have periodic boundary conditions. 98

28 Proficiency between each soft spot with each burst of localized deformation in a single avalanche. 100

29 A) Statistics of proficiency across many avalanches for all bursts of localized deformation and soft spot (green) and the maximum proficiency for each burst of localized deformation (blue). B) The statistics of the number of soft spots with proficiency above 0.01 for each burst of localized deformation. 101

List of Tables

1 The best fit power law for the intermediate regime as a function of excess contacts for the uniform distribution of bond weights. 51

1 Introduction

1.1 Definition of glass and disordered solids

1.1.1 Historical definitions

Pliny the Elder, the great Roman natural philosopher, wrote a story about how silica glass – what we usually refer to as glass – was discovered:

> There is a story that once a ship belonging to some traders in natural soda put in here and that they scattered along the shore to prepare a meal. Since, however, no stones suitable for supporting their cauldrons were forthcoming, they rested them on lumps of soda from their cargo. When these became heated and completely mingled with the sand on the beach a strange translucent liquid flowed forth in streams; and this, it is said, was the origin of glass [1].

Humans have been working with glasses for thousands of years [1] and it has been a source of mystery and confusion for nearly as long. Primarily, the confusion is over the state of matter glasses occupy: "Is glass liquid or is it solid?" Although some references have suggested evidence exists that glass is a viscous liquid because 800-year-old cathedral windows having thicker bottoms and thus the glass has flowed under its own weight [2], this observation is incorrect because it fails to account for other windows that are thicker on top. As it turns out, 800 years ago it was fairly difficult to make flat glass panes, so they put the heavier side on the bottom for stability [3]. A brief calculation of the relaxation time shows that if glass does flow at ambient temperatures, it does so on timescales much longer than human history [3].So, asking whether glass is a solid or a liquid is quite fundamentally asking: “What does it mean to be solid?”

1.1.2 Thermodynamics of disordered systems

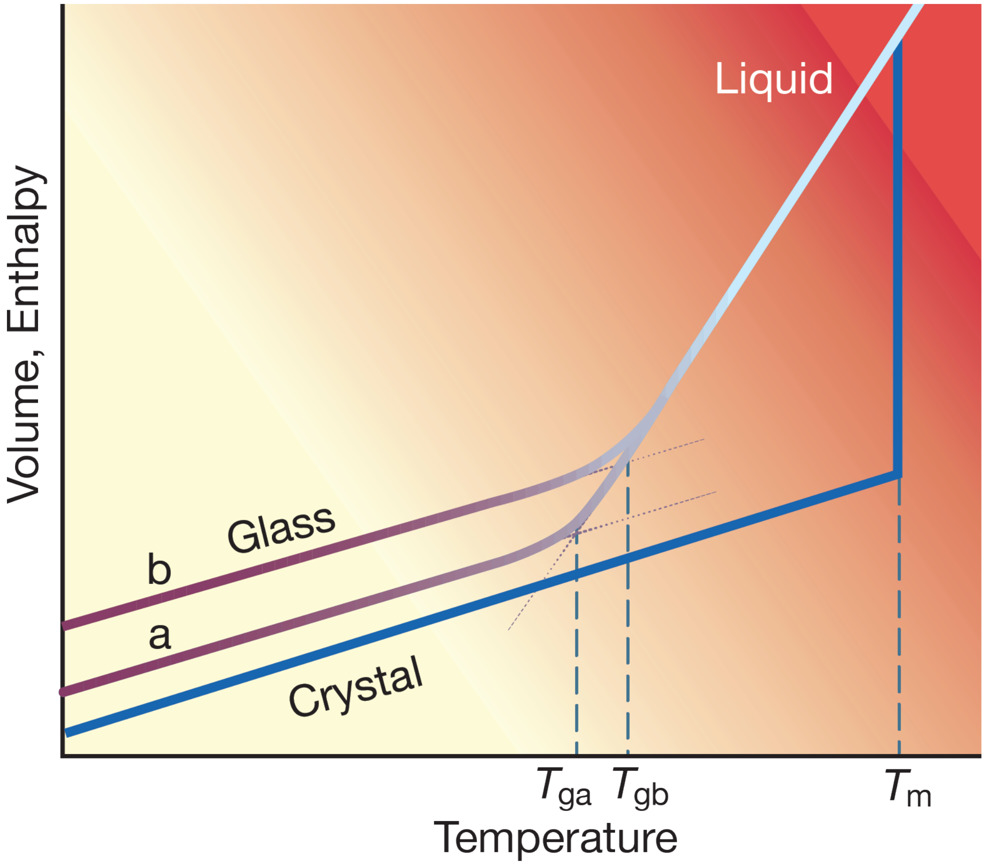

Figure 1: The volume, v, or enthalpy, h, of a liquid at constant pressure as a function of temperature T. T_m denotes the melting temperature of the crystalline solid. T_{ga} and T_{gb} denote the glass transition temperatures for a slow and fast cooling rate respectively. [4]

As the temperature is decreased, a liquid that crystallizes will suddenly change into a crystalline solid at a fixed critical temperature, T_m. This sudden transition is seen in the accompanying drops in the volume and entropy of the system. By contrast, a glass-forming liquid will remain a liquid as it is cooled well below the melting point of it’s crystalline counterpart, becoming a super-cooled liquid. In this regime, the volume and enthalpy change with temperature just as in the liquid above the melting point. Under further cooling, the behavior of the system gradually changes to become more solid-like, without crystallizing [4]. This lack of a sharp transition led to the description of glass as an “undercooled liquid” [5]. Even though this is a continuous transition, the temperature at which this transition occurs, called the glass transition temperature, can be defined by extrapolating the intersection point between the liquid and solid branches as seen in Fig.1 [4]. In addition, the glass transition temperature is not fixed; if the temperature is lowered more slowly, the glass transition temperature decreases [4].

1.1.3 Structure of glassy materials

Physical properties of materials, such as elasticity of a solid or viscosity of a fluid can often be traced back to the arrangement of the constituent particles within the material. For example, the qualitatively different behavior of glasses and crystalline solids arises from the different underlying microstructures of the systems. In a crystal, the microstructure is repeated, as described by the unit cell of the crystal. Because of this repetition many bonds are structurally equivalent. When the thermal energy reaches a critical value, all structurally-equivalent bonds break from the crystal network, defining a clear melting point. To use the crystallographic terminology, a glass can be considered a crystal with an infinitely large unit cell of infinitely-many particles. In a glass, then, each atom is structurally unique and each bond is broken at a different thermal energy. Thus, while crystals have an abrupt transition from solid to liquid, the breakdown of a glassy network is continuous [6]. Furthermore, the temperature at which this continuous transition occurs, T_g, depends on the rate at which the glassy system is cooled [7]. This analysis encapsulates why it is so difficult to discuss glasses and the glass transition: the solidification of a crystal from a liquid is abrupt, but the glass transition is a continuous rigidification that occurs over a range of temperatures.

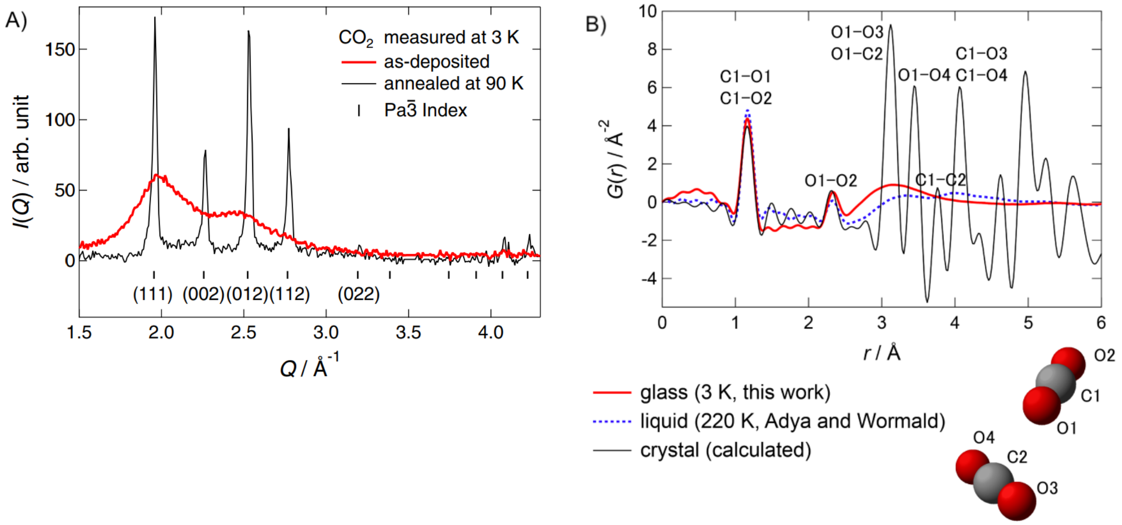

Figure 2: a) X-ray diffraction patterns of vapor-deposited CO_2 glass measured at 3 K. The red and black curves represent the glass as deposited and the glass annealed at 90 K respectively. Vertical tick marks show the peak position of crystalline CO_2. b) Pair distribution for glassy, liquid, and crystalline forms of CO_2 [8].

Using X-ray diffraction, the relative distances between particles can be extracted from materials of various states including crystalline, liquid, and glass. Using these distances, we can extract a pair-correlation function related to the probability of finding a particle at a particular distance from another particle. The distances between particles in a crystal are set by the lattice and this is reflected as bands in the diffraction pattern [9]. Crystalline systems have tight peaks in the diffraction spectrum as shown by the vertical spikes in Fig. 2a. From this diffraction pattern, information about the structure of the crystal can be extracted. For instance, the pair-correlation, $g(r)$, measures the likelihood of encountering a particle at a distance r from another particle. This can be computed directly the distribution of pairwise distances, r_{ij}, with

$$g\left(r\right) = \frac{1}{\rho}\left\langle \sum_{j\neq i} \delta\left(r - r_{ij}\right) \right\rangle_i . \tag{1}$$

The repetitive structure of crystals gives rise to a pair-correlation function which contains many peaks related to the lattice structure of the crystal such as the blue curve in Fig. 2b. Similarly, liquids also have a kind of geometrical order, having a small distribution of contacts and distances between particles [10], but the contacts are transient and constantly shifting [11]. In other words, the scattering pattern and corresponding pair-correlation function for a liquid are constantly shifting, but have general shapes for small distances related to preferred distances between nearest neighbors. Further, since liquids lack long-range order, the pair-correlation function must approach a constant value at long distances.

On the other hand, a glass doesn't show diffraction bands like a crystal as particle distances are not discrete, but it is very different from the liquid in that particles in glasses have permanent neighbors at definite distances [9, 11]. Prior to the 1930's, a common model for understanding the behavior of glasses was the "Crystallite Hypothesis" in which the microstructure of glass is crystalline, but the crystal grains are small and the orientation of crystalline planes are uncorrelated. This claimed to explain the X-ray diffraction patterns glasses produce by broadening the diffraction peaks in the crystal [5]. However, this model fails to accurately predict densities of glasses; it also fails to capture the thermal properties of glassy systems [6]. Critically, a comparison of the glass diffraction pattern to the diffraction pattern of a powder of crystalline material is radically different, showing a few broad rings rather than several sharp rings [11]. Further, silica glass is a nearly ideal elastic material, as it doesn't creep under load and recovers instantly after prolonged deformation, in experimental timescales [12]. In addition, it is not yet known how glasses are stably rigid since traditional theories of elasticity rely on crystalline structure [13]. However, attempts to calculate Young's modulus in glasses using these standard elastic theories systematically fall short [12].

Because of these problems, a new set of tools was developed to analyze the microstructure of glasses. Instead of attempting to explain glass physical properties by constructing glasses from microscopic crystals, the interparticle forces in glasses are assumed to be essentially the same as in the crystal, but the particles are not organized into a lattice [6]. In contrast to a lattice, the particles must arrange into an amorphous network, but X-ray diffraction tells us that this network is aperiodic and asymmetrical, unlike crystals [6]. At short distances, there are preferential distances due to the nearest neighbor interactions showing some correlation to the crystalline structure and, since amorphous materials lack long-range order, the pair-correlation must approach a constant value like liquid systems, but maintain contacts over time. This is reflected in how similar the glass curve, in red, and the liquid curve, in green, align in Fig. 2b. Although the microstructure of glasses shares many similarities with liquids, the mechanical properties of glasses share similarities with solids, and they exhibit anomalous behavior different from both. These ideas also explain the broadening of the diffraction peaks [5]and make predictions about the glass transition [6].

1.1.4 Potential energy landscape

A useful lens through which to view the transition and dynamics in glassy systems is the potential energy landscapes [4, 14]. For a system of N particles that interact with a known potential, the total potential energy of the system can be expressed as a function of the configuration of the system, $\Phi(\{x_{i\alpha}\})$, where $x_{i\alpha}$ is the position of particle i in the α dimension. An obvious minimum of this potential energy is the crystalline configuration of the system. However, a number of non-crystalline configurations can also be minima of

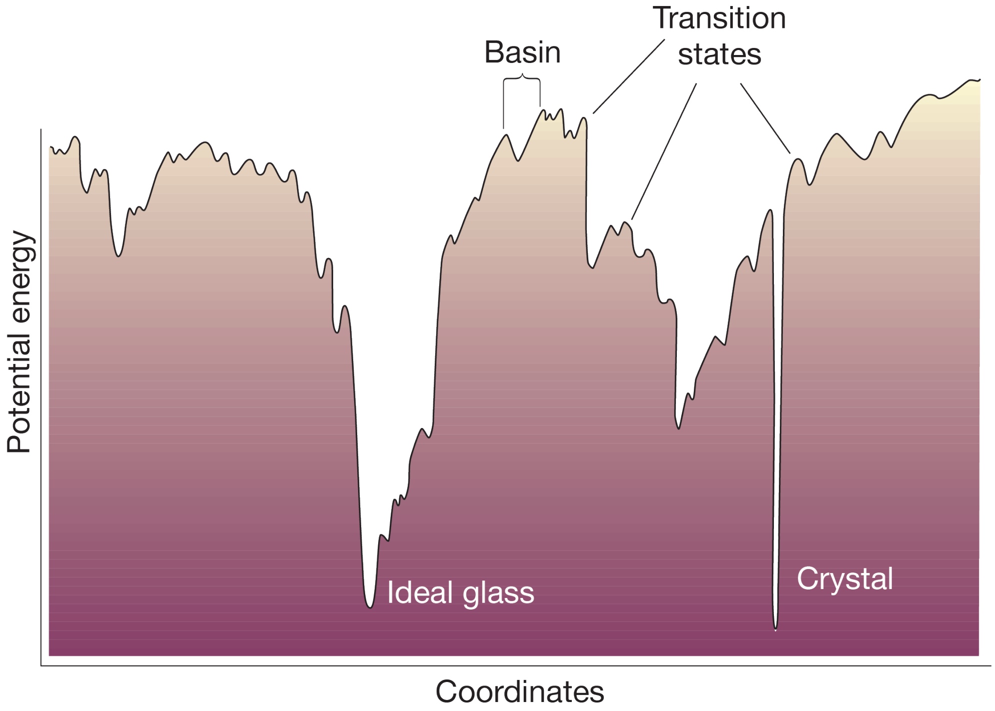

Figure 3: Schematic representation of the energy landscape of a glassy system where the x-axis is representative of configurations of particles in the glassy system. [4]

the potential energy function. Therefore, we describe the potential energy in configuration space as a landscape containing many minima with various energy barriers between them. A schematic representation of this landscape can be seen in Fig.3.

A system with thermal energy is free to move around and change its configuration so long as it has enough energy to cross the energy barriers separating nearby minima [15]. At high temperatures, many configurations are allowable and the system freely explores all available states. As the temperature is lowered, the number of thermodynamically available configurations decrease [15]. If cooled quickly, the system can become trapped in the shallow minima with high energy, since these minima take up a large portion of configuration space [15]. In this case, as the system can no longer flow freely, it behaves more like a solid, but it is non-crystalline. If cooled slowly, however, the system has enough thermal energy to escape these shallow minima near the top of the potential energy landscape, before it is trapped at some lower minimum, solidifying again but at a lower temperature.

In addition to thermal systems, there are a number of other systems which have constituent particles large enough to not fluctuate significantly with temperature. These "athermal" systems don't undergo a glass transition. Nevertheless, these systems of many loosely-connected components can rigidify under certain conditions. The parameter that controls this "jamming" transition from a free-flowing configuration of particles to a solid jammed state is not temperature, but density. As a system of many particles is compressed at some density the constituent particles must come into contact and, at some critical density, the system becomes mechanically stable. When systems jam, they haven't undergone a glass transition, nor have they crystallized, so the geometry and structure of the jammed state is very similar to that of the unjammed state in the same way that the liquid state of a glass forming liquid is very similar to its glassy state. So the origin of rigidity in disordered jammed states is similarly mysterious.

1.1.5 Constraint counting

In jammed systems, a constraint counting method, called Maxwell Constraint Counting, has been useful to understand the rigidity that arises from local mechanical stability [16]. In a system constrained to two dimensions, every particle has two translational degrees of freedom. As the particles interact, constraints are introduced such that the particles can't move without additional energy input in particular directions. For instance, if you place two pebbles in contact, one can't move toward the other without one of the pebbles deforming. The pebbles can, however, move apart or translate together without deforming.

For frictionless spherical particles, every interaction induces a constraint on motion which reduces the effective degrees of freedom available to the system. At a critical number of constraints, all degrees of freedom are constrained except the trivial translations of the entire system as a rigid body. This critical number of constraints is across the whole of the system, but local information can be assessed by the average number of contacts per particle– z – also called the average degree or coordination number, given by

$$z = \frac{2 * \#\text{ of bonds}}{\#\text{ of particles}}.$$

In a d-dimensional system of frictionless spheres, the critical value predicted by Maxwell Counting is $z_c = 2d$, when the total number of degrees of freedom, $N * d$, is equivalent to the total number of constraints, $N * d$. Numerical experiments reveal that the number of force-carrying contacts jumps from $z = 0$ to $z = 2d$ discontinuously at the jamming transition for frictionless particles [17].

One can reverse the jamming transition, or unjam a system, by increasing the volume until the density is below the critical density. A method like this is used in some grain silo constructions to induce flow by injecting air to increase the distance between grains, decreasing the local density and loosening the grains. However, this is not the only method one could use to fluidize the jammed system. If a jammed system is thermally excited, it can pass through a glassy phase and melt into a liquid phase. Additionally, one could apply stress to the system. For small stresses, the system responds as an elastic solid, but above some critical stress, the system will yield and flow. These critical points cannot be independently defined. For instance, as temperature increases, the critical yielding stress

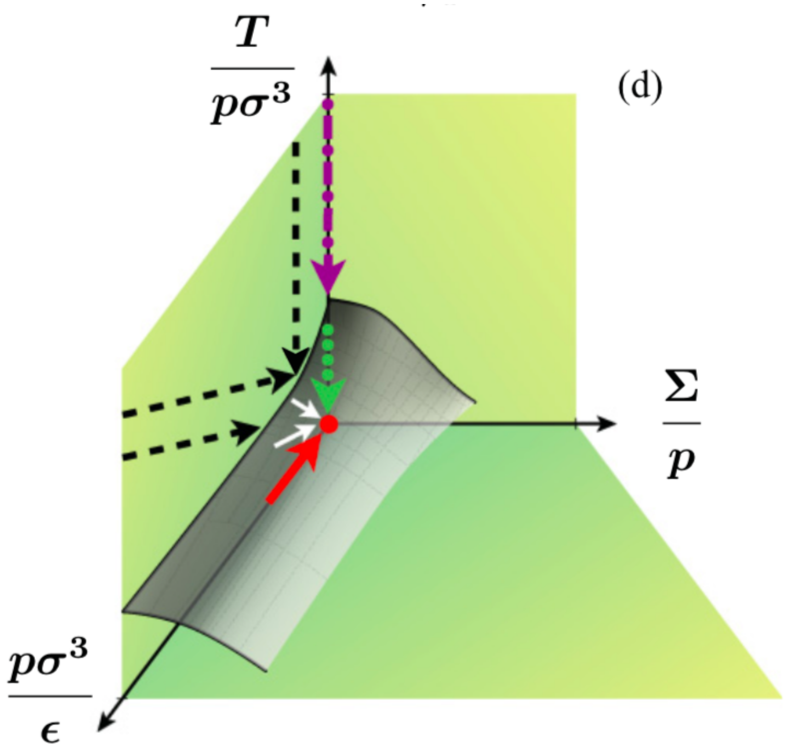

Figure 4: The phase diagram for soft sphere particles. The axes are nondimensionalized parameters: temperature ($T/p\sigma^3$), stress (Σ/p), and pressure ($p\sigma^3/\epsilon$), where T is temperature, p is pressure, σ is the diameter of hard spheres, Σ is the shear stress, and ϵ is the interaction energy scale [18].

decreases. This allows the construction of a jamming phase diagram, indicating at what parameters the amorphous system will rigidify, as in the example in Fig.4.

1.2 Applications of glass and jamming physics

Over the past several decades, amorphous solidification has been studied in a much broader class of materials than molecular glass, including granular materials, bulk metallic glasses [20], biological systems [19, 21], and even crowds of people [22]. Similar questions arise in all of these systems: "Under what conditions is the material solid-like?" and "How does the material deform under external forces?" To highlight a particularly interesting example, consider biological tissue. Epithelial tissues are thin tissues that cover surfaces

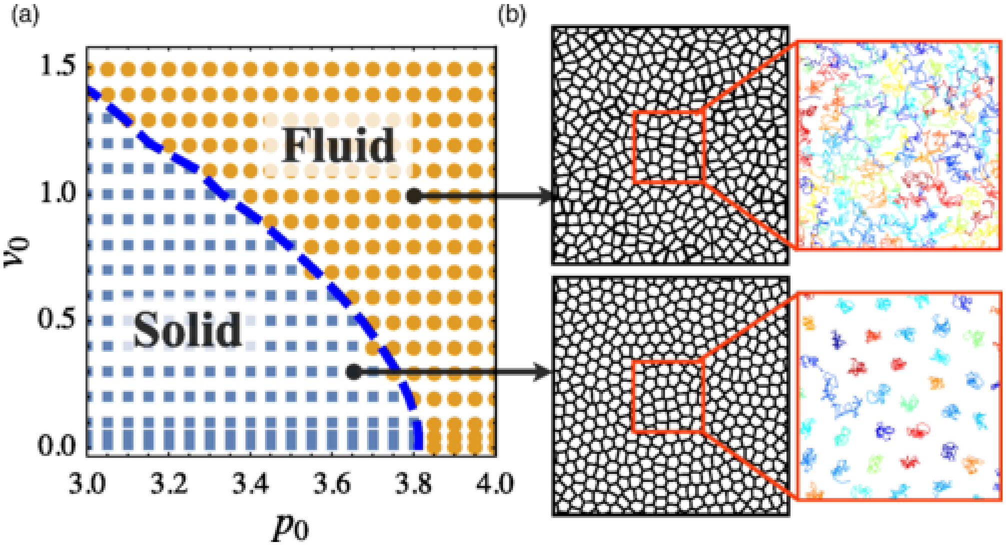

Figure 5: a) The phase diagram for confluent tissues as a function of cell motility, v_0, and target shape index, p_0, in the self-propelled Voronoi model for cells. b) Examples of the fluid and solid states of the self-propelled Voronoi and the trajectories of the particles. Note the solid state particles move very little [19].

throughout animal bodies such as the skin, lungs, and digestive tracts. This tissue is very convenient to model since it is effectively two-dimensional. It's also important to model as most cancers involve epithelial tissue. One physical model of epithelial tissue is the self-propelled Voronoi model. In this model, the area of each Voronoi cell is conserved, each cell has a preferred perimeter, and every cell has a random self-propulsion velocity. This model has been demonstrated to have a jamming transition controlled by the "preferred shape parameter"–the preferred perimeter nondimensionalized by the area of the cell–and self propulsion velocity, as seen in the phase diagram in Fig. 5a. The preferred shape parameter is particularly interesting, since it is a structural order parameter which is experimentally accessible via simple video analysis, unlike jamming in particulate systems.

1.3 Dynamics and material properties of disordered materials

1.3.1 Examples of amorphous system dynamics

Amorphous materials are not only fascinating, but their mechanical, electrical, and optical properties differ from crystalline materials in many useful ways. In this thesis, we focus on the unique mechanical properties of such materials under applied stress. Silica glasses have, for instance, been used for centuries over quartz crystals because of the ease of workability. Silica glass becomes a soft solid or a viscous liquid at temperatures much lower than the melting point of quartz, allowing ancient peoples access to the material that they otherwise could not work with. On the other hand, sometimes systems are actually much more difficult to generate and work with than the crystalline form. Bulk Metallic Glasses, for instance, when first discovered, had to be cooled evenly at speeds upwards of 1×10^6 K/s [23]. When conventional metals are cooled from the liquid state, they typically crystallize very rapidly just below the melting point. This rapid crystallization doesn't usually result in perfect crystals. For example, usually, metals form polycrystals, a solid state composed of microscopic, randomly-oriented crystalline grains. Crystalline metals tend to fracture and corrode at the boundaries between these crystal grains and other crystalline defects such as particles missing or replaced by impurities. Metallic glasses have no crystalline grain boundaries or crystalline defects. This leads to metallic glasses being much stronger than their crystalline counterparts, as shown schematically in Fig.6. However, under extreme forces, crystalline metal systems deform irreversibly without breaking, but metallic glasses can fail catastrophically [20].

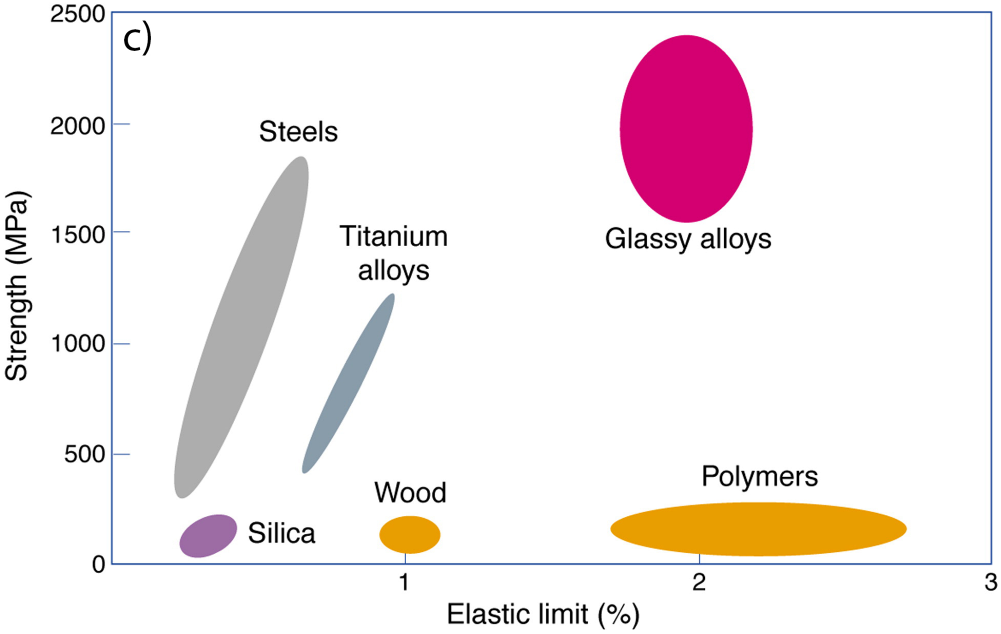

Figure 6: Tensile yield strength of various materials vs the elastic strain-to-failure limit. Bulk Metallic Glasses, Glassy Alloys, are stronger and more resistant to plastic deformation than their crystalline counterparts like steels [23].

In amorphous granular systems, small changes in density can have large changes in the number of contacts and, therefore, small perturbations to weakly-jammed systems can cause sudden, rapid collapses. For instance, oranges in a grocery store are often stacked in a crystalline packing and, so long as you pick from the upper layers, you won't cause a cascade of oranges. If, on the other hand, the oranges are thrown onto the pile at random, they can jam without crystallizing and it becomes unclear which oranges can be moved without causing the whole system to collapse. Amorphous systems are ubiquitous in the world around us, far beyond only silica glass, from the landscape to everyday items. For instance, many natural features on earth are composed of small grains like sand in desert or boulders in an earthquake fault. Nowhere is this more obvious than in an avalanche where the rocks and snow on a mountainside are perturbed in such a way that they flow down the mountain [24]. For other granular systems, we rely on their ability to flow like grain from a silo so we can transport food. Pharmaceutical processes require powder to flow and mix in order to make drugs of the correct dosages in large quantities. Understanding the way in which these systems respond to external perturbation can aid us in finding ways to predict and prevent their failure.

1.3.2 Phenomenology of materials under applied shear

Rheology is the study of how materials deform in response to external loading. Fluid-like materials flow under any loading of stress, or force per unit area. On the other hand, solid like materials, can support stress without flowing. Instead, as a small amount of stress is applied to a solid-like system, the material deforms to provide an equal and opposite force. In the linear approximation, the amount of deformation, or strain, is directly proportional to the applied stress in the same way that the compression of a spring is proportional to the force applied. The proportionality constants that compare different stresses and strains are the elastic constants which measure the material stiffness, similar to the spring constant in Hooke's law. However, real materials can only support a finite amount of stress without undergoing plastic deformation, a permanent change to the shape or structure of the material.

A yielding transition of material under applied stress refers to the change in the global mechanical response of the system from an elastic solid response to a plastic flowing response. This transition can be a smooth transition like butter or foam. Or there can be a sudden catastrophic failure like the shattering of a glass window. The primary problem understanding this transition is theoretical. Crystals are well understood to flow and fail at crystalline defects, and the details of the density and types of defects in the system. Amorphous systems, on the other hand, have no explicit defects because they have no crystalline structure and therefore extending crystalline theories is difficult.

Two of the most prominent phenomenological models for amorphous systems, shear transformation zone (STZ) theory and Soft Glassy Rheology (SGR) theory, are mesoscopic, where the relevant variables are defined on length scales larger than the constituent particle sizes but smaller than the scale of continuum elasticity. In these models, a macroscopic sample of an amorphous material is conceptually divided into mesoscopic regions and then assumptions are made about the stress and the strain in these regions. As the system is strained the stress and local strains can grow until these mesoscopic subsystems rearrange and yield. However, these models make different sets of assumptions about the mesoscopic regions to predict different phenomena in glassy dynamics. SGR theory is concerned with understanding how soft glassy systems flow under shear. It attempts to predict the nonlinear relationship of viscous stress to strain rate, and the aging process in thermally active systems that results in an increase of the elastic modulus while the loss modulus decreases [25]. To that end, SGR considers the local strain in each region or how far each region is strained from a stress-free state. As the system is strained, these local strains increase until a region yields and rearranges into a new stress-free configuration. This rearrangement is modeled as an activated proccess with an energy barrier associated with the stiffness of the region and some critical strain [25]. By using activated processes, this model captures strain-induced yielding, as a region beyond the critical strain will yield very quickly, but it also allows unstressed regions to yield at a slower rate to mimic the nonlinear couplings between regions due to the inherent disorder in the system [25]. STZ theory is concerned with the phenomenology of the yielding transition. In this model, rather than considering strain, stress is considered directly. It is assumed that the stress in each region will grow linearly with increasing shear until the stress in one region goes above some predefined critical value. Once a region is above the critical value that region yields or relaxes its stress. Such models have been useful in predicting hysteresis and shear band formation [26–28].

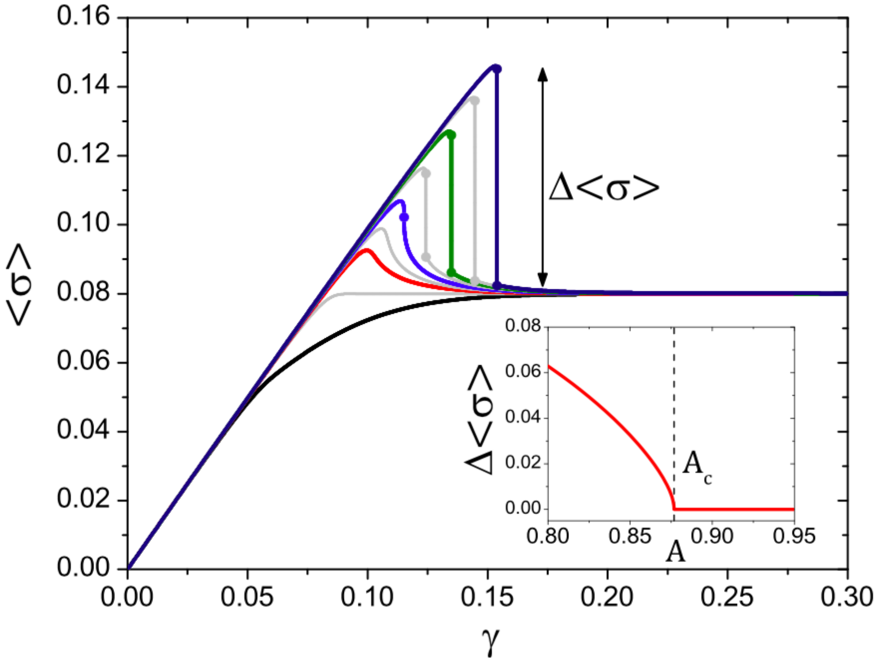

Figure 7: Yielding in a mean-field elasto-plastic model. Stress, $\langle\sigma\rangle$, vs strain, γ, for increasing degree of annealing, A, from bottom to top. The lowest annealing has a smooth transformation that transitions into a smooth stress overshoot and continues to transition to a discontinuous transition. (Inset) The magnitude of the discontinuous stress drop, $\Delta\langle\sigma\rangle$, as a function of the degree of annealing. Low values of A indicate large annealing [29].

Recent work in related models has shown that whether amorphous materials fail via ductile flow or brittle shear bands depends strongly on the system preparation protocol, or equivalently the statistics of the stresses in the mesoscopic regions [29, 30]. These works have combined analytically solvable mean-field elastoplastic models with molecular dynamics simulations of generic glass formers to investigate the effect of material preparation [29]. In these elastoplastic models, the system is divided into mesoscopic elements characterized by their current stress and their yield stress or the stress at which they will rearrange. In simulations, these yield stresses are chosen from some distribution. A schematic representation of those distributions is shown in Fig. 8a. As mentioned earlier, when glass-forming liquids are cooled quickly the system will find itself in a shallow minimum of high potential energy compared to a slowly cooled glass. Annealing is a process by which a glass in the shallow minima is warmed and cooled repeatedly so that it is able to relax to a deeper energy minimum. The degree of annealing is encoded in these elastoplastic models by the distributions, $P_0(x)$, of initial stress to instability, x. As the system is strained or additional stress is applied, the stress in the mesoscopic elements increases until the stress in one region surpasses the yield stress and begins to fail, potentially triggering other points to fail according to a non-positive-definite elastic kernel. At this point, the stress and yield stress for the original failed region are resampled from another distribution.

The resulting stress strain curves for different initial yield stress statistics, shown in Fig. 8b and Fig. 7, reveal that the qualitative yielding behavior is dependent on the initial stability. As shown by the black curve in Fig. 7 and the lightest curve in Fig. 8b, poorly annealed systems, systems in the shallow minima, have a smooth transition and describe materials like foam and mayonnaise and other soft solids. On the other end of the spectrum, for the most highly-annealed state tested, there is an accumulation of stress followed by a sudden drop in stress as the system discontinuously fails at the yielding point, as metallic and molecular glasses do. As the degree of annealing is decreased, the discontinuous jump in stress becomes weaker until it approaches zero at a particular value of the disorder [29]. These results are very similar to mean-field elastoplastic models with short range interactions, which can be solved analytically. Such models are in the Random Field Ising Model (RFIM) universality class and also exhibit a discontinuous jump in stress

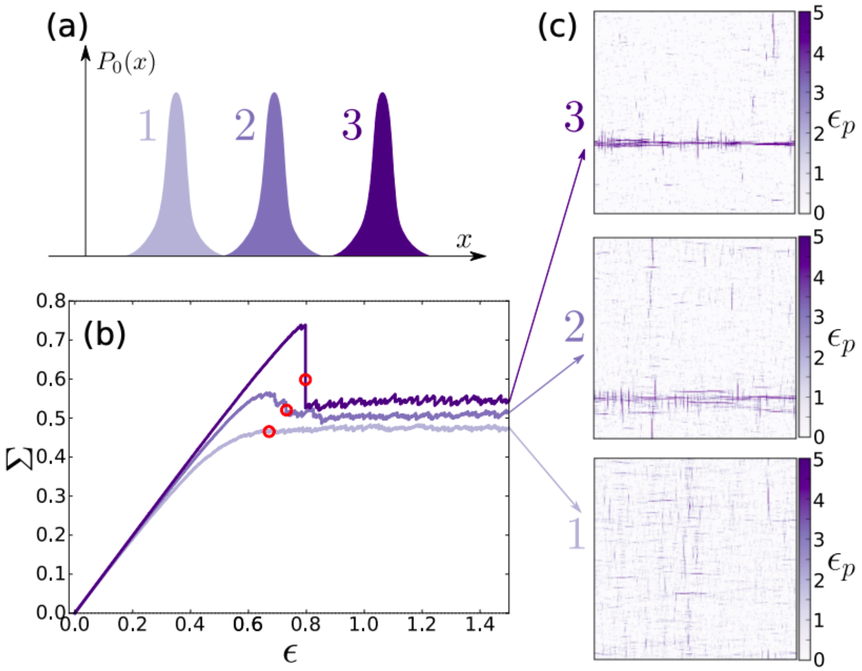

Figure 8: a) Schematic of three distributions, $P_0(x)$, of stress to instability, x, for elements in an elastoplastic model for 1) a poorly annealed glass, 2) a moderately annealed glass, and 3) a well annealed glass. b) Stress versus strain curves for these three distributions of initial stabilities. c) Snapshots of the plastic strain during the yielding transition indicated by red circles.

that terminates at a second order critical point. An open question is whether elastoplastic models with long-range interactions, as seen in experiments and simulations, is in the same universality class. This indicates that the variety of yielding behaviors of disordered materials are fairly generic across different types of particle interactions or microscopic dynamics; the transition from soft yielding to sudden catastrophic failure is controlled by the degree of annealing which controls the initial stability of the system [29].

1.3.3 Linear response and vibrational modes

One powerful method to probe the various material properties of a system, such as the elastic modulii or thermal properties, is vibrational analysis. For instance, thermal properties like the low-temperature heat transfer are mediated by phonon excitations [31] and, in the thermodynamic limit, we can understand the low-frequency vibrational properties of a crystal in terms of phonons [32]. In condensed matter systems, vibrations and other excitations have wavelengths and propagation directions dictated by the microstructure of the system. For instance, the smallest wavelength that a one-dimensional crystalline system can support is on the order of the lattice spacing between the particles, while the longest wavelength is dictated by the size of the system. The vibrational density of states, $D(\omega)$, is a measure of density of vibrational modes with frequency ω and it is useful for determining a number of physical properties, including the specific heat. For crystalline solids, Debye theory predicts the density of states should scale with ω^{d-1} in the low-frequency regime, where d is the spatial dimension [32]. This behavior is independent of the details of the microstructure of the crystal unit cell; it applies universally across crystals. In crystalline materials, this analysis leads to the canonical T^3 temperature dependence of the specific heat [32].

Amorphous materials also appear to have universal vibrational behaviors, but the spectra of amorphous materials are anomalous compared to the crystal vibrational spectrum. Glasses do not obey Debye scaling in the low-frequency regime; the density of states scales as ω^α where $\alpha \neq d-1$ [33]. This deviation from crystals will alter the low-temperature thermal behavior of glassy systems; the specific heat of glassy systems scales with T rather than the T^3 seen in crystalline systems [34]. Additionally, while the vibrational modes in a crystal are plane waves, the vibrations in glasses can be disordered and in the low-frequency regime they can also be localized. Recent work isolates localized excitations in the vibrational spectrum to identify points of failure in disordered materials [35–37].

Mean field theory for glasses using replica symmetry breaking techniques predicts an ω^2

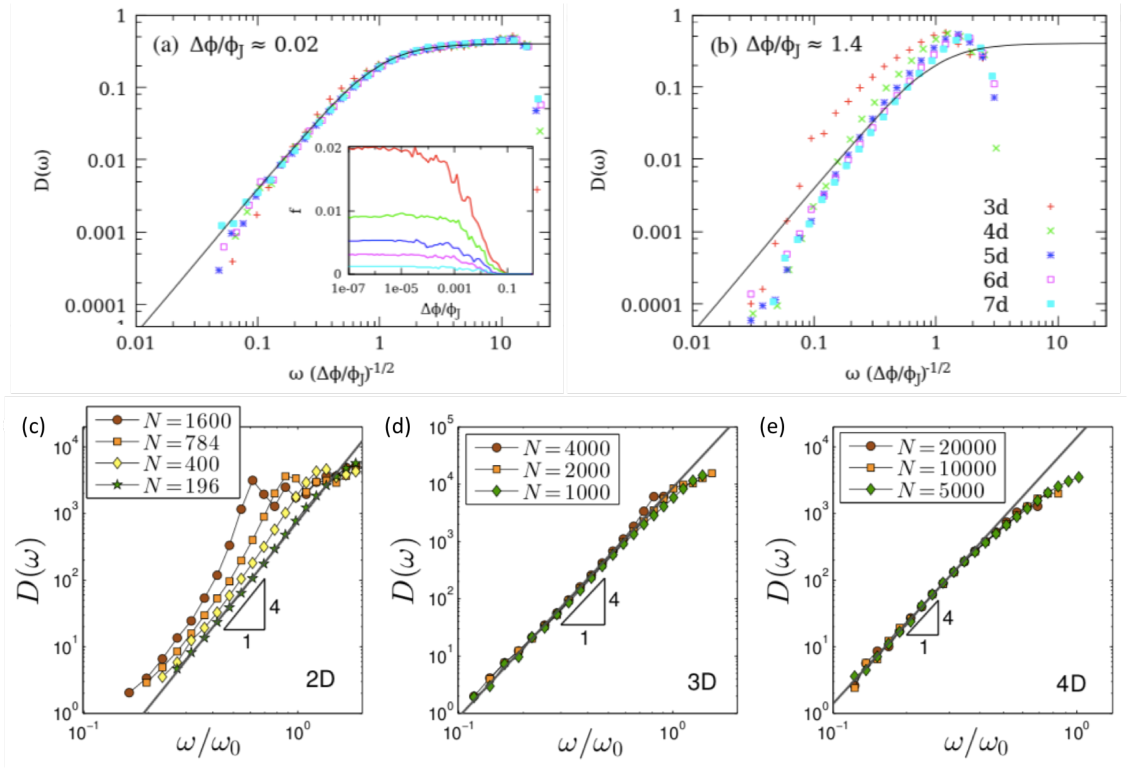

Figure 9: a) DOS for N = 8192 in d = 3 to 7, averaged over 30 to 50 configurations of soft sphere packings in high dimensions agree with the infinite-dimensional result of $D(\omega) \propto \omega^2$ in the low frequency regime [38]. b) The same DOS for higher pressures. Detailed simulations over thousands of configurations in two- (c), three- (d), and four- (e) dimensional systems find ω^4 scaling for the lowest vibrational modes [39].

scaling regime in the density of states independent of dimension [40]. This is exact in the limit of infinite spatial dimensions and some have argued that this persists in dimensions as low 3 or 4 [38, 40]. Fig 9a shows the vibrational density of states for systems just above the isostatic point with dimensionality from 3 to 7. At low compression shown in Fig 9a, the bulk of the spectrum is well described by the ω^2 prediction that transitions into a plateau. Note the fit is particularly poor for three-dimensional systems, especially far from the jamming density as seen in Fig. 9b. Recent simulations of jammed solids in low dimensions confirm that $D(\omega) \propto \omega^4$, as shown in Fig 9c,d, and e [39]. These simulations are averaged over thousands of configurations and focus explicitly on modes with lower energy than the lowest plane wave mode, in order to extract the power law exponent with high precision. This analysis finds ω^4 not only in 2d or 3d but also in 4d systems. This behavior is consistent with the earlier predictions for density of states found in the "Soft Potential Model" for soft glassy materials [41, 42].

Simultaneously, it has been observed that the low-frequency excitations are quasi-localized modes, which are vibrations that only involve the movements of a fraction of the particles in one location. One way of measuring the localization of a mode is via the Inverse Participation Ratio (IPR) of eigenvector $\overrightarrow{v}$

$$IPR(\overrightarrow{v}) = \frac{\sum_i v_i^4}{\left(\sum_i v_i^2\right)^2}.$$

For a perfectly localized mode the IPR is 1 while for a perfectly extended mode the IPR is $\frac{1}{N}$, where N is the number of particles in the system. A plane wave mode, for instance, is a very extended perturbation since a large fraction of the system participates in the passage of a plane wave. If a displacement vector–a vector that lists particle displacements from equilibrium positions–has few non-zero entries such that only a few particles are moving, then the vector is localized. Maximum localization occurs when only one particle is moving during the displacement. In quasi-localized modes, one typically finds a localized core with long range tails.

The normal modes in a perfect crystal are plane waves. Dislocations and other crystal defects can disrupt the normal modes causing localization near the defects. Similarly, in disordered materials the quasi-localized modes in the low frequency regime can help to identify the regions where we would expect deformation under external stress [35, 36].

In addition to the low-frequency anomolous behavior, there is an additional universal

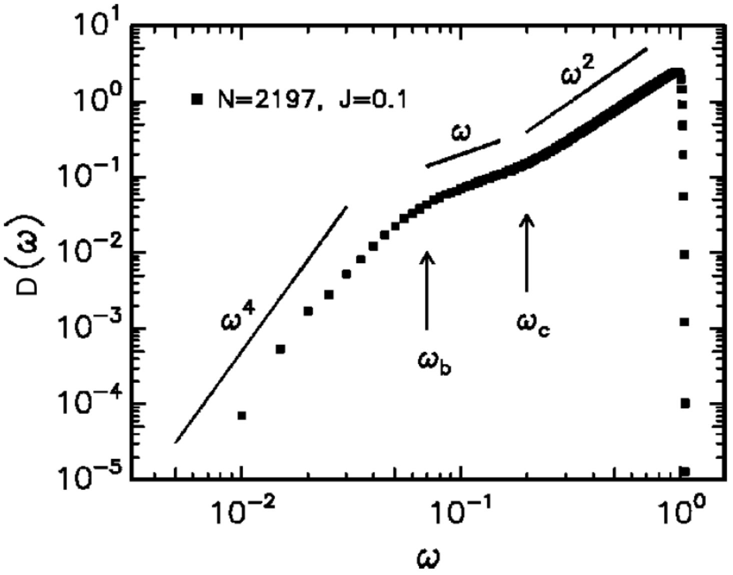

Figure 10: Log-log representation of the simulated density of states for a cubic lattice of coupled, randomly-oriented oscillators. The arrows indicate the two characteristic frequencies ω_b, the boson peak, and ω_c, the frequency above which the system returns to ω^2 scaling [43].

feature called the boson peak. This is an excess of modes in the low-frequency regime above the Debye prediction. This is seen in Fig. 10 by the transition from ω^4 scaling to linear scaling. The frequency at which the boson peak occurs, ω^*, scales with the coordination number as $\omega^* \sim z - z_c = \Delta z$, which can be explained by a length-scale cutting argument and Maxwell constraint counting discussed in 1.1.5 [44, 45].

Specifically, during compression of an amorphous system, there exists a critical density, ϕ_c, where the average number of contacts is exactly the critical number of contacts to attain mechanical stability [17]. It has been shown that compression of systems above this critical density increases the number of contacts according to a simple scaling law in 3D:$(\phi - \phi_c)^{\frac{1}{2}} \propto z - z_c$ [17]. If we compress a three-dimensional system of N particles with side length L, extra constraints are added to the system proportional to system size [44],

$$\Delta N_c = N\frac{\Delta z}{2} \sim L^3 \Delta z. \tag{2}$$

On the other hand, cutting the boundaries of a the system relaxes a number of constraints proportional to the surface area of the system, $p \sim L^2$. Because $L^2 < L^3\Delta z$ for long length scales, large compressed systems will remain overconstrained after cutting the boundary. However, if the lengthscale approaches a critical value, $l^* \sim (\Delta z)^{-1}$, the number of constraints removed via cutting is larger than the number added via compression. Since frequency scales are inversely proportional to length scales, vibrational modes with frequencies larger than $\omega^* \sim \Delta z$ are little effected by excess contacts [44].

The boson peak also has an effect on the localization of the vibrational modes. Above ω^* the modes are extended and disordered, becoming localized at the edge of the vibrational spectrum [46]. Below ω^* the vibrational modes are quasi-localized hybridizations of phonon-like modes and local excitations [46]. The eigenvector of the vibrational mode can be written as a list of displacement or polarization vectors. The vibrational modes in the boson peak have a distribution of polarization lengths that is universal and distinct from the distribution found in plane waves and Anderson localized modes [47].

1.3.4 Thesis outline

This is a very exciting time to study disordered materials because we have made significant progress in recent years. Notably, analytic results have been derived for hard spheres in infinite dimensions [48, 49]. A better understanding of how the infinite-dimensional hard sphere model extends to lower dimensions and softer materials would provide significant insight into the behavior of glasses, more complex granular materials, and biological systems [50].

Additionally there have been numerical advancements in the simulation of glassy systems. One past limitation for simulations of glassy systems is the speed at which the simulations can be cooled. Attempting to cool simulated glasses at rates corresponding to experimental glasses has previously been out of reach, limiting the kind of glasses that can be sampled and studied. Over the past few years, new numerical techniques have been developed to probe glasses and jammed packings at much higher densities than are typically achievable by slow compression or annealing. Thin films of ultra-stable glasses can be obtained by direct simulation of vapor deposition [51]. Bulk ultrastable glasses in simulations can be generated with algorithms which allow particles to change size by swapping radii or directly with some sort of chemical potential or training [52, 53]. These algorithms allow glassy systems to equilibrate at low temperatures much faster than standard Monte-Carlo simulations. When these low-temperature systems are quenched, they create bulk ultra-stable glassy systems, as the configurations being sampled are much deeper in the potential energy landscape. These new simulation tools allow for exciting investigations into the material properties of experimentally accessible molecular glasses.

In Chapter 2, we investigate the origins of the interesting low-frequency vibrational behavior of glasses and jammed solids, including a region in the density of states–$D(\omega)$–that scales as ω^4 with quasi-localized excitations important for flow and failure. To our knowledge, there are no constructive models that generate ω^4 scaling and explain the mechanism for quasi-localization. However, recent work indicates random matrix models can provide explanations for universal vibrational properties in glasses. To better understand the surprising low-frequency vibrational modes in structural glasses, we study the spectra of a large ensemble of sparse random matrices where disorder is controlled by the distribution of bond weights and network coordination. We find $D(\omega)$ has three regimes: a very-low frequency regime that can be predicted analytically using extremal statistics, an intermediate regime with quasi-localized modes, and a plateau with $D(\omega) \sim \omega^0$. In the special case of uniform bond weights, the intermediate regime displays $D(\omega) \sim \omega^4$, independent of network coordination and system size, just as recently discovered in simulations of structural glasses.

In Chapter 3, we use tools developed to understand and predict the interesting collective properties and nontrivial dynamics in unstable and active disordered materials to characterize behavior in a model for dense human crowds. While the behavior of amorphous solids under shear is relatively well-understood, the instabilities in active systems remain difficult to characterize and predict. In the context of dense crowd dynamics, existing work has analyzed position fluctuations in a self-propelled particle (SPP) model to identify Goldstone modes and soft spots in models for human crowds. This analysis requires time-resolved trajectory information in order to form predictions for collective behavior, which can be cumbersome. To address this issue, we have developed a novel method to generate static packings in an artificial potential that reproduce the packing structures in a class of point-of-interest active SPP crowd simulations. These static packings then allow us to precisely identify local structural defects that govern dynamical group behavior, so that we can predict the locations of rearrangements and "material" failures in dense, active SPP models. Unlike previous methods, these predictions can be derived from a single snapshot and could be relevant to preventing dangerous emergent phenomena in real crowd systems.

In Chapter 4, we investigate the relationship between structure and dynamics in amorphous systems during large-scale plastic deformation. At zero temperature, the deformation of an amorphous system due to applied shear strain can be separated into elastic branches where the particles do not change neighbors, and rearrangements where they do. Some rearrangement events are small and localized, while others involve large or system-spanning avalanches. Using numerical simulations of soft spheres, we find that these avalanches can be decomposed into a series of bursts of localized deformation, and we develop a novel clustering method inspired by persistent homology to isolate these bursts of localized deformation. Next, we develop a method to study the "linear response" of unstable systems during an avalanche, by extending existing tools for identifying structural defects and study how the population of structural defects evolves during an avalanche. We find that bursts of localized deformation in the avalanche correlate strongly with localized soft spots generated from the linear spectrum. These data should help to constrain elastoplastic models for glasses and granular matter.

Finally, in Chapter 5, we provide a brief outlook and discussions for future work.

1.4 Additional Work

Here we outline projects that the author has contributed to during his graduate work but are not included as chapters in this thesis.

1.4.1 Predicting failure in disordered solids from structural metrics

One reason disordered solids are so challenging to understand is that, unlike crystals, their microscopic structure lacks long-range order. In crystals it is easy to identify a defect where the crystalline order is broken, and unsurprisingly the crystal breaks at those defects. Over the past 50 years, analogous structural defects have been proposed in amorphous solids [54], but it has proven very difficult to connect them to deformation and failure. For this reason, theoretical work has largely remained disconnected from simulations. Perhaps more problematically, all these theories are phenomenological in the sense that they contain fitting parameters that we do not know how to extract from first principles, i.e. from the microstructure and interactions between the constituent parts of the material.

Fairly recently, large-scale computer simulations of glass-formers have reinvigorated the search for structural defects. Until now there have been three main drawbacks to this line of inquiry. First, there has never been a consistent methodology for evaluating whether a given metric that identifies structural defects works well for predicting deformation and failure, although efforts towards this goal have been made [55]. Second, it has not been clear whether a given method works best only on a particular model system or the interaction potential for which it was designed, or whether some methods work well universally across different disordered solids. Finally, computer generated amorphous solids have historically been vastly more ductile than those in real experiments, and so it was difficult to simulate brittle materials that exhibit catastrophic failure. Happily, a recent breakthrough based on a computational method that allows particles to swap positions with one another has addressed this last issue [52].

In this project, which is submitted and under review, we use this new computational protocol, as well as a more standard one, to study glass-formers across the brittle-to-ductile transition. As a function of the applied shear strain, we simultaneously quantify a large number of metrics for identifying structural defects in disordered solids, proposed by research groups across the world. We develop a standard methodology for comparing these metrics to one another, and to the complex deformation fields that result from the applied strain. We find that different classes of structural metrics are not always strongly correlated, suggesting that different paradigms for identifying structural defects are reporting distinct information. With a few exceptions, the metrics we investigated are excellent at predicting deformation in ductile materials over short strain scales, 10^3 in the system sizes studied, and several remain correlated beyond 10% strain, highlighting that structure really does govern deformation in these zero-temperature materials under simple shear. The quality of a given metric does not vary much between the two interaction potentials we studied, but across all metrics the undeformed state does a very poor job of predicting the shear band in very brittle glasses. Robustly across several different metrics, we demonstrate that this failure in prediction occurs because the density of defects increases dramatically in brittle solids in the pre-yielding elastic regime.

1.4.2 Jammed packings behave similarly under random forcing and shear

Shear is a necessarily global process—in order to shear a system, one pushes from the boundaries, affecting all particles within the system. Activity, however, is a local process. Active particles each have a driving mechanism that propels them in a certain direction, where that direction is subject to change on a characteristic time scale. The ways in which loads are carried in a sheared system are then fundamentally different from that of active systems. However, recent studies have noted that in granular systems the two forcing mechanisms yield viscosities [56] and large density fluctuations [57, 58] which are similar. The connection is further bolstered by a similarity in the forms of the infinite-dimensional mean-field equations dictating the response to shear, random force, and friction [59–61] due in part to their ability to be represented by memory kernels.

What is missing in the low-dimensional scenarios is a unifying picture as developed in mean-field; to develop such a picture, it is necessary to note how and where the similarities between shear and random forces diverge. For example, Liao and Xu [56] noted that particles driven with the same magnitude force in random directions will have the same viscosity curves as their sheared counterparts [62–64], albeit with different critical exponents. While constant overdamped force–thus constant velocity–and random direction is a typical assumption of active particle models [65, 66], it obscures a possible connection. The authors even note that changing the metric of velocity to be the velocity parallel to the force alters the exponents. It is possible that varying the magnitude of force may yield the shear exponents or that both perturbations fall into a broader class. Taking cues from the density of states, it has been shown that the response of particles to both random force [57, 67] and shear [68] are dominated by the lowest eigenmode. The energy landscape picture of shear response [69, 70] then suggests that the connection can be thought of as traversing similar landscapes.

In this project, soon to be submitted for publication, we show how activity and shear are related in soft sphere systems via the energy landscape. In particular, we show that the characteristics of the stress-strain curves, the avalanche statistics and the spatial sampling of saddle points in the pre-yielding regime, and the location of the yielding point have the same scaling relations found in sheared systems. Furthermore, while the correlation length of forces on particles under shear is fixed, if we vary the correlation length, we find that the magnitude of quantities such as the shear modulus change systematically with correlation length. This implies that shear can be seen as a special case of a more generic random forcing. While the macroscopic responses such as avalanche size and shear modulus obey similar scaling relationships regardless of whether the body forces follow simple shear or are randomly oriented, it is interesting to note that the spatial structure of instabilities may be quite different depending on the nature of the forcing. Brittle sheared systems clearly fail via localized shear bands, but preliminary data suggest that the lack of symmetry in the random systems might prevent such spatial organization. This will be an interesting area for future research.

2 A simple random matrix model for the vibrational spectrum of jammed packings

Abstract

To better understand the surprising low-frequency vibrational modes in structural glasses, we study the spectra of a large ensemble of sparse random matrices where disorder is controlled by the distribution of bond weights and network coordination. We find $D(\omega)$ has three regimes: a very-low frequency regime that can be predicted analytically using extremal statistics, an intermediate regime with quasi-localized modes, and a plateau with $D(\omega) \sim \omega^0$. In the special case of uniform bond weights, the intermediate regime displays $D(\omega) \sim \omega^4$, independent of network coordination and system size, just as recently discovered in simulations of structural glasses.

2.1 Introduction

The vibrational spectra of disordered glassy materials exhibit universal features. Although these features govern the mechanical response and provide insight into mechanisms for material failure, their origin remains poorly understood.

Perhaps the most well-studied feature of the density of vibrational states $D(\omega)$ is the boson peak, which is an excess of vibrational modes above the Debye prediction, $D(\omega) \propto \omega^{d-1}$ [71–73]. In jammed packings the frequency at which the peak occurs, ω^*, scales linearly with the average excess number of contacts δz above the isostatic point where the number of constraints equals the degrees of freedom [44, 72, 74]. Additionally, the eigenvector statistics of modes in the boson peak follow a universal distribution [75].

Recently, another universal feature has been identified in simulations of low-dimensional jammed systems: $D(\omega) \sim \omega^4$ below ω^* [39, 76, 77], which deviates from recent mean-field calculations for the spectra in infinite dimensions that predict $D(\omega) \sim \omega^2$ [38, 78]. This interesting behavior has also been found in Heisenberg spin glass systems [79]. Understanding this regime is important, as the vibrational modes are quasilocalized and help govern flow and failure in disordered solids [71, 79–84].

Given the success of random matrix theory in predicting universal features in other physical systems [85], it is natural to wonder if a random matrix model may also explain the ω^4 scaling in jammed packings. Other features, including the boson peak, have already been understood in terms of Euclidean random matrices, which are dynamical matrices for a set of points that are randomly and uniformly distributed in space [86].

Although there are generic arguments that the global minima of random functions should have a spectrum that scales as ω^4 [87], we would like to construct a random matrix model to provide insight into how features of the ω^4 region, such as the prefactor, or the location of the scaling regime, change with parameters such as the excess coordination δz. Such an understanding is important for predicting how material preparation protocols alter the mechanical response of glassy materials.

2.2 Model

We study matrices that share three important features with the dynamical matrix: they are symmetric, positive-semidefinite, and force balancing. In higher dimensions, force balance corresponds to d sum rules on partial sums of entries in each row of a matrix, while in 1D, the force balancing restriction simply requires the sum over all the entries in a row must be zero [71]. This rule is also obeyed by standard or weighted Laplacians, L_{ij}, which are also symmetric and positive semi-definite. They are defined by

$$L_{ij} = \begin{cases} -k_{ij} & i \text{ and } j \text{ are connected} \\ \sum_{l \neq i} k_{ik} & i = j \\ 0 & \text{Otherwise} \end{cases}, \tag{3}$$

where k_{ij} is the independently chosen random weight of the edge between particles i and j and in the special case of the standard Laplacian, $k_{ij} = 1$ [88]. Standard Laplacian matrices are well-studied and possess distinctive vibrational spectra [89], so we focus on weighted Laplacians for the remainder of this Chapter.

In order to calculate the Laplacian we must specify the topology of the underlying graph. Although recent advances have been made in analytically characterizing the spectra of Laplacians on an Erdős-Rényi graph [90], Erdős-Rényi networks are not locally isostatic, as a significant fraction of nodes are under-coordinated (fewer than isostatic coordination $z_c = 2d$), which leads to highly localized excitations that are not seen in jammed packings.

Instead, we consider the weighted Laplacian on a z_c-regular graph with a small number of additional edges, or crossbonds. Since weighted Laplacians only obey one sum rule, they are effectively 1D and $z_c = 2$. The number of additional bonds is $\delta z N$ where N is the number of points and δz is the excess coordination.

Another important control parameter is the distribution of the edge weights and, in particular, the weight of this distribution near zero. We choose to parameterize this distribution as a power law with exponent α, normalized so that the mean is 1, $\rho(k) \propto k^{\alpha}$ on $\left[0, \frac{\alpha+2}{\alpha+1}\right]$. A uniform distribution corresponds to $\alpha = 0$ and we only consider normalizable distributions,

$\alpha > -1$.

2.3 Finite size scaling of weighted ring

We first study the finite size scaling of the low frequency excitations at isostaticity, when $\delta z = 0$ and the underlying network topology is simply a ring of size N. Although this is a well-studied model, we believe its finite-size scaling can provide insight into the case with $\delta z > 0$.

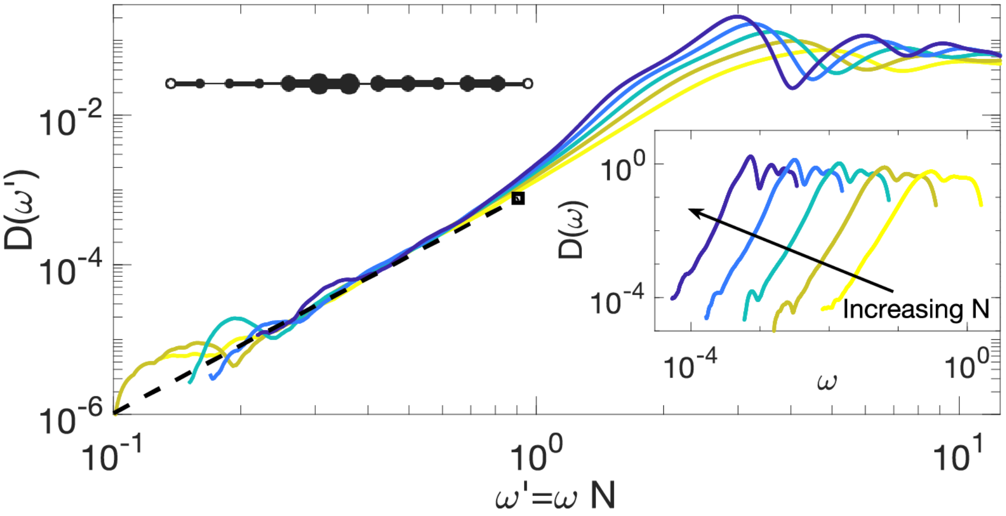

Figure 11: The rescaled density of states, $D(\omega')$, for the two-regular graph with N=16, 64, 256, 1024, and 4096 and $\alpha = 0$, normalized by system size, N, averaged over at least 10^6 matrices. The analytic prediction for the low-frequency scaling is shown as the black dashed line. In the upper-left we have a sketch of a 1d chain with periodic boundary conditions (the open circles are the same node) **Inset:** Unscaled density of states, $D(\omega)$.

The inset to Fig. 11 shows the sample averaged density of states for $\alpha = 0$, calculated via diagonalization of the matrix, as a function of system size N, averaged over 2×10^6 matrices. The main panel shows the sample averaged density of states as a function of the normalized frequency, $\omega' = \omega N$, highlighting a region of power-law scaling at the lowest frequencies that disappears in the thermodynamic limit.

We hypothesize that the lowest-energy mode on a weighted ring is well approximated by a stretching of the two weakest bonds, with all other bond lengths relatively fixed. We expect this to be the case when $\alpha \leq 0$, so that the weight of the lowest two bonds are well separated from bonds with larger values of k_{ij}, especially in the limit of low ω, $\omega < N^{-\frac{2\alpha+3}{4\alpha+3}}$.

If the two weakest bonds have strengths k_1 and k_2 and are separated by m nodes, the frequency of this mode is $\sqrt{\frac{N(k_1+k_2)}{m(N-m)}}$. As we show in Appendix A, one can use extremal statistics to find the exact distribution of the weakest bonds on the ring to predict that the low-frequency density of states scales as:

$$D(\omega) \propto N^{2\alpha+3}\omega^{4\alpha+3}. \tag{4}$$

For a uniform distribution of bond weights ($\alpha = 0$), the contribution of these modes to the density of states scales as $(N\omega)^3$. The scaling of Eq. 4, using $\alpha = 0$, is shown as the black dashed line in Fig. 11.

2.4 Crossbonded ring with unifrom bond weights

We hypothesize that adding a small number of crossbonds alters the low-frequency behavior by reducing the effective distance between the two weakest bonds. In the case of $\delta z = 0$, the two weakest bonds separate the ring into two segments that can move relative to one another at nearly zero cost, but if a crossbond connects those two segments it will significantly increase the energy of that mode. Therefore, the weak bonds that contribute to low-frequency modes must both be in a segment between crossbonds. Because there are $N\delta z$ such segments, we expect that crossbonds give rise to an extensive number of low-energy modes, so that the scaling regime described in the previous section persists in the thermodynamic limit.

We search for very low-weight edges that generate a two-cut of the network: two edges that, if removed, disconnect the network. In the supplement, we show the low-frequency density of states scales as

$$D_\alpha(\omega) \propto \frac{\omega^{4\alpha+3}}{\delta z^{2\alpha+3}}, \tag{5}$$

independent of system size.

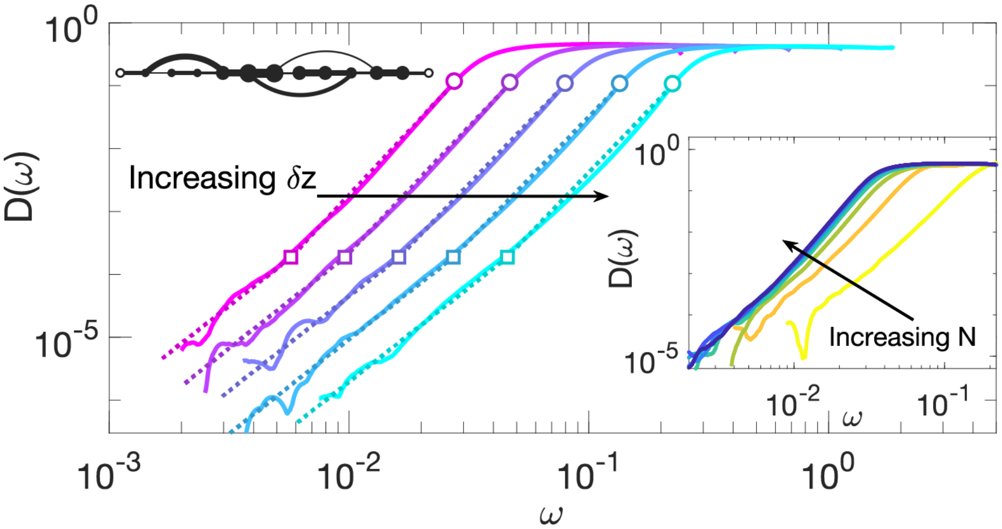

Figure 12: The density of states for fixed system size (N=1000) and changing $\delta z = 0.1, 0.168, 0.282, 0.476, 0.8$ In the upper-left we have a sketch of a 1d chain with periodic boundary conditions (the open circles are the same node) with additional bonds. **Inset:** The density of states, $D(\omega)$, for fixed $\delta z = 0.1$ and changing system size N = 20, 60, 120, 240, 500, 1000, 2000, and 4000.

To test the universal form predicted by Eq. 5, we computed the spectrum $D(\omega)$ for rings with crossbonds and uniform bond weights ($\alpha = 0$). For each value of δz and N we generated between 10^5 and 2×10^6 matrices samples [1], with independently chosen weights and uniformly random placements of the endpoints of the $N\delta z/2$ crossbonds. The inset to Fig. 12 displays plots of the sample-averaged density of states $D(\omega)$ for fixed $\delta z = 0.1$ as N increases. This example plot supports the convergence of $D(\omega)$ to a gapless distribution as $N \to \infty$. The main panel of Fig. 12 displays the computed density of states (solid lines) for large N ($N = 1000$) and varying δz. The dashed lines in Fig. 12 show fits of the form $D(\omega) \propto \omega^3$ to the low frequency region, as predicted by Eq. 5. These fits are in good agreement with the computed spectra.

---

[1] For $\delta z = 0.1$ and $N = 500$ and 1000, we calculate 2×10^6 matrices and for $N = 2000$ and 4000, we

Based on Eq. 5 and the more complete form of the density of states derived in Appendix B, we expect a collapse of $D(\omega)$ when frequencies are scaled by δz. Fig. 13(a) shows the density of states for the scaled frequency, $\omega' = \omega/\delta z$. For $\delta z = 0.168$ we numerically identify a frequency ω_e that best separates the ω^3 scaling regime from the remaining spectrum. Eq. 5 then predicts that all other cutoff frequencies should scale linearly with δz, which is in good agreement with the data as shown by the open squares in Fig 12 and 13(a).

In addition to the crossover at ω_e, there is a second crossover where $D(\omega)$ flattens to a plateau. In jammed packings at zero temperature, where the boson peak occurs at the onset of the plateau, ω^* is often defined as the frequency at which the density of states attains a fixed fraction f (typically 25 %) of its value in the plateau [91]. We use that same definition here with $f = 0.25$.

In many disordered solids, numerical evidence suggests $\omega^* \propto \delta z$ [72, 74]. To check whether this is also true for our matrices, we plot the density of states as a function of the rescaled frequency $\omega' = \omega/\delta z$, for various values of δz, shown in Fig 13(a). We see a good collapse of the three regions, suggesting that both crossovers are linear in δz, which is also

---

calculate 522240 and 261120 matrices. For all other values, we calculate 10^6 matrices.

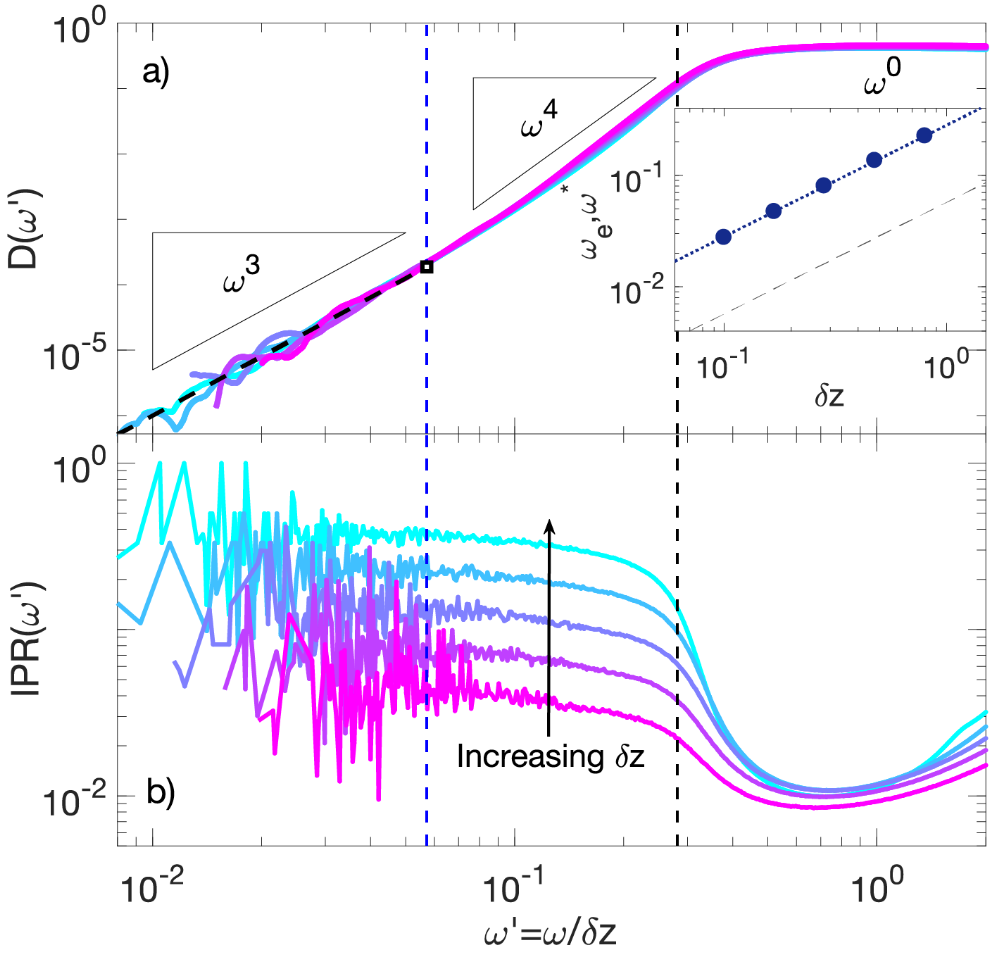

Figure 13: **a)**The density of states, $D(\omega)$, rescaled by δz. The blue dashed line indicates the transition from the ω^3 regime to the ω^4 regime while the black dashed line indicates the transition to the plateau. The inset shows the scaling of ω^* and ω_e with δz is linear. **b)**The inverse participation ratio, IPR, rescaled by δz. The IPR approaches a quasilocalized plateau in the ω^3 region.

highlighted by the inset to Fig 13(a).

Importantly, this confirms that although the intermediate region between the two crossover frequencies spans less than a decade in frequency, it is well-defined and does not change as a function of excess coordination or system size. Specifically, these results mandate the following functional form for the density of states in our random matrix model with $\alpha = 0$:

$$D(\omega) = \begin{cases} \frac{4}{L^2}\left(\frac{\omega}{\delta z}\right)^3 & \omega \leq \omega_e \\ \propto \omega^{\psi} & \omega_e \leq \omega \leq \omega^* \\ \propto \omega^0 & \omega^* \leq \omega \end{cases} . \tag{6}$$

To extract the scaling of $D(\omega)$ below the boson peak, we fit $D(\omega)$ to this functional form and extract the best-fit ψ for each value of δz (See table in supplemental materials). We find that all curves are consistent with $\psi = 4.0 \pm 0.05$ for frequencies $\omega_e \leq \omega \leq \omega^*$. This suggests $D(\omega) \propto \omega^4$, just as seen below the plateau in simulations of jammed packings.

Given the striking similarities between the density of states in this simple model and jammed packings, we would also like to know if the eigenvector statistics are similar. In jammed systems, many modes at frequencies below the boson peak are quasilocalized [91]. This is quantified by the inverse participation ratio (IPR), $IPR(\omega) = \sum_i v_i^4/(\sum_i v_i^2)^2$, where v is the vector associated with the eigenfrequency ω. In Fig 12(b), the very low-frequency regime of the IPR plateaus, and the value of this plateau scales with δz, indicating that only about $\frac{1}{\delta z}$ nodes are participating in the vibration.

Interestingly, the intermediate region exhibits values of IPR that are typically associated with quasilocalized excitations. Moreover, the size of those excitations seems to decrease as δz increases. In jammed solids, an outstanding open question is how the size of localized excitations changes as one approaches the jamming transition.

2.5 Crossbonded ring with power-law bond weights

Having a simple constructive model that reproduces many features of the vibrational modes in jammed packings is useful, because we can vary the model and ask what features are necessary to generate the ω^4 scaling in the density of states. One natural choice is to perturb the distribution of bond strengths away from the uniform distribution by changing the power-law exponent α.

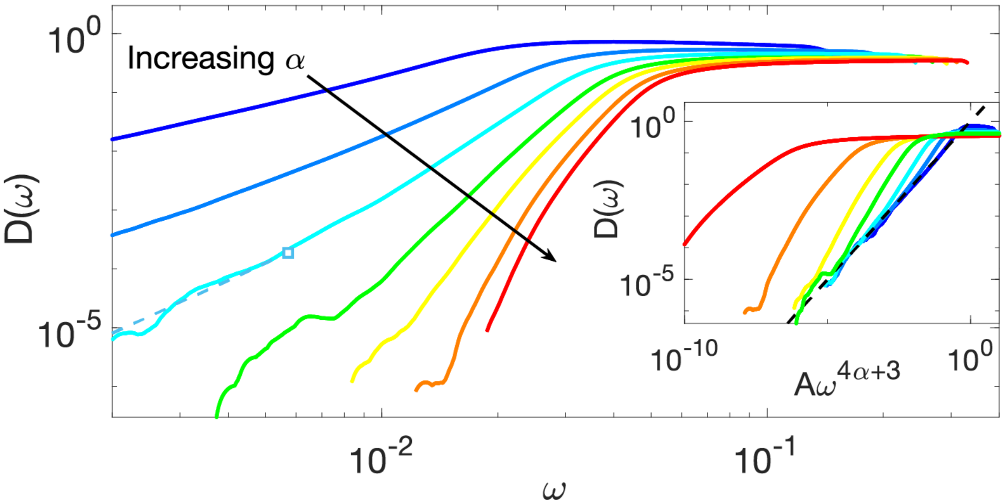

Figure 14: The density of states for $\alpha = -0.4$, -0.2, 0, 0.25, 0.5, 1, and 2, with $\delta z = 0.1$. **Inset:** $D(\omega' = A\omega^{4\alpha+3})$ for the same values of α as in the main figure, where A is the coefficient predicted in Appendix B. The black dashed line is the predicted scaling for the low frequency regime.

For $\alpha > 0$, very weak bonds become rare and the assumptions that lead to Eq. 5 break down. Numerically, we observe that a gap appears to open up in the spectrum as α increases, as seen in Fig 14. For $\alpha < 0$, we expect Eq. 5 should still hold, as shown by the numerical data in the inset of Fig 14. In this case, however, the crossover frequency no longer scales linearly with δz, and so the power-law scaling between ω_e and ω^* – the exponent ψ in Eq. 6 – is no longer independent of δz. In other words, an intermediate regime consistent with

$D(\omega) \propto \omega^4$, independent of δz, is only possible for $\alpha = 0$.

2.6 Discussion

In this Chapter, we propose a simple random matrix model that is locally nearly isostatic and captures features of the vibrational states of disordered packings that are typically associated with marginality. Specifically, the model recapitulates a plateau in the density of states above ω^*, and a regime consistent with ω^4 scaling immediately below that. Our model also has a second crossover frequency ω_e, below which $D(\omega)$ scales as ω^3.

The modes in this extremely low frequency regime are governed by extremal statistics, and so we can calculate their properties analytically. This allows us to demonstrate that ω_e scales linearly with excess coordination δz if and only if the weak bonds are uniformly distributed, suggesting that ω^4 seen in jammed packings arises due to a special, self-organized distribution of the weakest bonds.

Of course, jammed packings only exist in dimensions greater than unity. Above one dimension, the bond between particles is described by a tensor and not a scalar weight. The d by d interaction block that corresponds to a single bond in the Hessian matrix can be written as $H_{ij\alpha\beta} = -V''|u_{\parallel}|^2 - \frac{V'}{r_{ij}}|u_{\perp}|^2$. The first term is often referred to as the stiffness while the second term is called the prestress term [92].

Interestingly, observations in 3D jammed packings suggest that the ω^4 regime only exists when the V' term is unperturbed; even very small perturbations to the prestress open up a gap in the density of states [93]. This suggests that a self-organized balance between the stiffness and prestress must occur in systems near isostaticity. Moreover, the stiffness is always positive and the prestress always decreases the entries in the Hessian, so it is plausible that the prestress term is driving some interactions to be very weak near isostaticity, similar to our simple model.

While suggestive, a more concrete connection will require us to extend our analysis to higher dimensions. We see an ω^4 regime when bond strengths are uniform, but it is unclear what quantity would be analogous to a uniform bond weight in a $d \times d$ sub-block. Concurrent work by Benetti et al. focused on d-dimensional Laplacian matrices where the magnitude of each bond is unity, but the geometry of the bond is randomly distributed, and these also generate scaling consistent with ω^4 at low frequencies [94]. To better understand the connections between these models and why both generate ω^4 scaling, one could study systems with random bond weights and ordered geometries, or have both be disordered.

Furthermore, although ω^4 scaling as been observed in several glass forming systems [39], the ω^3 regime may be unique to 1D systems, as it has not been reported in simulations or in the random matrices with 3×3 sub-blocks [94]. In addition, we see about half a decade of frequency consistent with ω^4 scaling, while the most recent data from Lerner and collaborators [39, 77, 93] finds almost a full decade.

Nevertheless, the ω^3 scaling regime is interesting. Disordered rings are well-studied, but major results focus on localization caused by disorder [95, 96]. To our knowledge, the finite-size scaling effects of the vibrational spectrum have not been discussed previously. Our model demonstrates that finite size effects in the disordered ring, such as this gapless low-frequency scaling, can be promoted into properties that are maintained in the thermodynamic limit by network disorder.

Although we have excellent understanding of the ω^3 regime in this simple model, and convincing numerical evidence demonstrating $D(\omega)$ scaling as ω^4 over a window of about half of a decade in ω, we have not identified a mechanism for the ω^4 regime, where we know the assumption of two weak bonds and two rigid arms breaks down. There are many higher order modes that may contribute, and visual inspection of the eigenvector structure suggests that no single one dominates, so there is no obvious simple extension of our argument for ω^3.

One possible avenue for understanding this regime is suggested by recent numerical work that shows universality in the eigenvector statistics associated with the boson peak. Specifically, eigenstatistics in jammed packings match those from both the random matrix model described here, as well as the dense limit of this model where all nodes are connected to one another [75]. Interestingly, the eigenvector statistics are also identical in a much simpler model which is just the sum of a diagonal matrix and a Gaussian orthogonal matrix. Very recent analytic work suggests that such matrices are marginal; they are on the edge of a non-ergodic localized phase [97]. It would therefore be very interesting to extend this analytic work to sparse matrices and study the tail of the density of states.

Another way to extend our model is to alter the loop structure of the underlying graph. In our random matrix model, the loop structure is uncontrolled since we add crossbonds with uniform probability across the graph. This is different from jammed systems where neighbors of one particle are more likely to be neighbors of each other and loops are small. It is fairly straightforward to extend our analytic analysis of the ω^3 regime to random matrix models with smaller loops, and we expect that the prefactor and the onset of the scaling ω_e will change, but the ω^3 scaling will not. However, this change could impact the behavior of the ω^4 regime.

2.A Extremal statistics in the two-regular graph

In this section, we calculate the scaling for a ring of N particles and a ring with crossbonds where particles are bonded to their nearest neighbors and the strengths of those bonds, $\{b_i\}$, are chosen independently with the distribution $f(b)$. (It is also assumed that the masses of the particles are identical.)

The mode associated with exciting only the 2 weakest bonds is a very low energy mode. The calculation here is done by taking the 2 weakest bonds as they are, but assuming all other bonds are rigid.

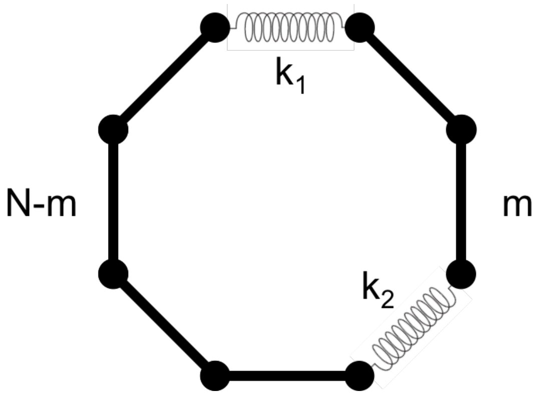

Figure 15: A ring or periodic 1d spring system with the two weakest bonds highlighted as springs.

We will call the strength of these bonds k_1 and k_2 with a distance of m nodes between the bonds. This system is equivalent to 2 masses joined by a spring which has 1 non-trivial mode with a frequency of $\sqrt{\frac{N(k_1+k_2)}{m(N-m)}} \equiv \sqrt{\frac{Ns}{m(N-m)}}$ where $s = k_1 + k_2$.

The distribution of the weakest bond strength is given by

$$\rho_1(k_1) = N * f(k_1) * (1 - F(k_1))^{N-1}, \tag{7}$$

which is just the probability density of a bond having strength k_1 multiplied by the probability that all other bonds are at least that strong [98]. The distribution of the second lowest mode is somewhat more complicated since we need to enforce that $k_2 \geq k_1$. So the distribution of k_2 given k_1 is

$$\rho_2(k_2|k_1) = \frac{(N-1)\theta(k_2-k_1)}{(1-F(k_1))^{N-1}} f(k_2)(1-F(k_2))^{N-2}. \tag{8}$$

The frequency depends on the sum $s = k_1 + k_2$. The distribution of this sum can be obtained from the convolution of the distribution of k_1 and k_2:

$$\rho_s(s) = \int_{k_{min}}^{k_{max}} \rho_1(k_1)\rho_2(s-k_1, k_1)dk_1, \tag{9}$$

$$\begin{aligned}\rho_s(s) = N(N-1)\int_{k_{min}}^{k_{max}} & f(k_1)f(s-k_1) \\ & (1-F(s-k_1))^{N-2}\theta(s-2k_1)dk_1.\end{aligned} \tag{10}$$

By changing variables and assuming m is uniformly distributed, we can obtain the distribution of the frequencies as:

$$\rho_\omega(\omega) = \sum_{m=1}^{N-1} \rho_s(\frac{m(N-m)}{N}\omega^2)\frac{2m(N-m)}{N(N-1)}\omega. \tag{11}$$

2.A.1 Power-law distribution

Let $f(b) = \frac{\alpha+1}{L^{\alpha+1}} b^{\alpha}$ and $F(b) = \left(\frac{b}{L}\right)^{\alpha+1}$ under the limit $b \in [0, L]$ and $\alpha > -1$. By substitution, we find

$$\begin{aligned}\rho_s(s) =& \frac{N(N-1)(\alpha+1)^2}{L^{2(\alpha+1)}} \int_0^L \theta(s-k_1)\theta(L-s+k_1) \\ & \theta(s-2k_1)k_1^{\alpha}(s-k_1)^{\alpha}\left(1-\left(\frac{s-k_1}{L}\right)^{\alpha+1}\right)^{N-2} dk_1.\end{aligned} \tag{12}$$

These step functions are only non-zero in the range $max(0, s-L) \leq k_1 \leq s/2$. Using this information and a change of variables, $k = sq$, we can extract the primary contribution of s:

$$\begin{aligned}\rho_s(s) =& s^{2\alpha+1} \frac{N(N-1)(\alpha+1)^2}{L^{2(\alpha+1)}} \theta(L - \frac{s}{2}) \\ & \int_{\max(0, 1-\frac{L}{s})}^{\frac{1}{2}} q^{\alpha}(1-q)^{\alpha}\left(1-\left(\frac{s(1-q)}{L}\right)^{\alpha+1}\right)^{N-2} dq.\end{aligned} \tag{13}$$

Under the assumption that s is small, such that $\left(1-\left(\frac{s(1-q)}{L}\right)^{\alpha+1}\right)^{N-2} \approx 1$ (we will discuss the range of validity of this assumption below), the density of states for large N can be found via direct integration of $\int_0^{\frac{1}{2}} (q(1-q))^{\alpha} dq = \frac{\Gamma(\alpha+1)^2}{2\Gamma(2\alpha+2)}$:

$$\rho_s(s) \approx s^{2\alpha+1} \frac{N(N-1)(\alpha+1)^2}{L^{2(\alpha+1)}} \frac{\Gamma(\alpha+1)^2}{2\Gamma(2\alpha+2)}, \tag{14}$$

$$\rho_{\omega}(\omega) \approx \frac{N\Gamma(\alpha+1)^2(\alpha+1)^2}{\Gamma(2\alpha+2)L^{2\alpha+2}} \omega^{4\alpha+3} \sum_{m=1}^{N-1} \left(\frac{m(N-m)}{N}\right)^{2\alpha+2}. \tag{15}$$

By converting the sum over m into a similar integral over $\frac{m}{N}$ we have

$$\rho_\omega(\omega) \approx \frac{\sqrt{\pi}(\alpha+1)^2(2\alpha+2)\Gamma(\alpha+1)^2}{2^{4\alpha+5}\Gamma(2\alpha+\frac{7}{2})L^{2\alpha+2}} N^{2\alpha+4}\omega^{4\alpha+3}. \tag{16}$$

Since this only applies to the lowest vibrational mode, the density of states is given by ρ_ω/N:

$$D(\omega) \approx \frac{\sqrt{\pi}(\alpha+1)^2(2\alpha+2)\Gamma(\alpha+1)^2}{2^{4\alpha+5}\Gamma(2\alpha+\frac{7}{2})L^{2\alpha+2}} N^{2\alpha+3}\omega^{4\alpha+3}. \tag{17}$$

2.B Extremal statistics in the two-regular graph with additional bonds

A more generic system is the ring with crossbonds. These crossbonds are simply additional connections between particles that are non-adjacent in the ring. See Figure 16 for an example of a crossbonded graph; although the sketch is 2-dimensional the cross bond interaction only depends on the distance along the ring not the euclidean distance across the ring.

With crossbonds, we are restricted to choosing bonds in a region between 2 crossbonded nodes. These regions are shown in Figure 16 by the green arrows.

2.B.1 Distribution of bounded regions

Let m_1 be the number of edges between crossbonded nodes.

We place the cross bonds randomly. Therefore the crossbonded nodes are chosen uniformly. If we have E crossbonds then there are $2E$ crossbonded nodes (which may not be unique). The increase in average coordination number is given by $\delta z = \frac{2E}{N}$. So the number

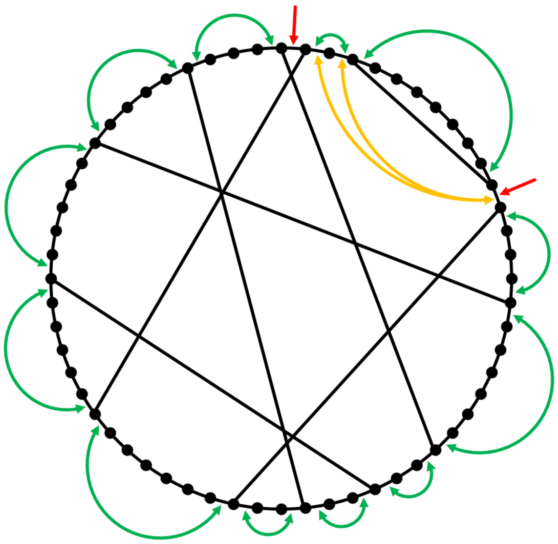

Figure 16: A sketch of a crossbonded network with 56 particles and 7 crossbonds. The green arrows delineate the regions between crossbonds where 2 edges can disconnect the network. The red arrows point out edges that can't disconnect the network. The yellow arrows point out sets of edges that would disconnect the network that aren't between crossbonded nodes.

of crossbonds and crossbonded nodes are $\frac{N\delta z}{2}$ and $N\delta z$ respectively.

Since these are uniformly placed, we can expect the distance between them to be defined via a Poisson process. We can find the distribution of the second crossbonded node where we set the first crossbonded node to 1, since we can always rotate along the ring. Order statistics provide the following result:

$$p_1(m_1) = \frac{(1 - \frac{m_1}{N})^{N\delta z - 1}}{\sum_{m=0}^{N-1}(1 - \frac{m}{N})^{N\delta z - 1}} \approx \frac{e^{\delta z} - 1}{e^{\delta z}} e^{-m_1 \delta z}. \tag{18}$$

This distribution very quickly approaches the thermodynamic expression of an exponential decay.

2.B.2 Crossbonded spectrum

For each chain of length m_1, we choose the 2 weakest bonds where the bonds are chosen from the distribution $f(b) = \frac{\alpha+1}{L^{\alpha+1}} b^\alpha$ under the limit $b \in [0, L]$ and $\alpha > -1$. We can write $\rho_s(s)$ as

$$\begin{aligned} \rho_s^{m_1}(s) =& \frac{(\alpha+1)^2 m_1(m_1-1)}{L^{2(\alpha+1)}} s^{2\alpha+1} \theta(L - \frac{s}{2}) \\ & \int_{max(0,1-\frac{L}{s})}^{\frac{1}{2}} q^\alpha (1-q)^\alpha \left(1 - \left(\frac{s(1-q)}{L}\right)^{\alpha+1}\right)^{m_1-2} dq. \end{aligned} \tag{19}$$

We assume small s, such that $\left(1 - \left(\frac{s(1-q)}{L}\right)^{\alpha+1}\right)^{m_1-2} \approx 1$. Following the same argument from the previous section where m_2 is the number of nodes between the weakest bonds, we find the distribution:

$$\begin{aligned} \rho_\omega(\omega) =& \omega^{4\alpha+3} \frac{\Gamma(\alpha+1)^2(\alpha+1)^2}{2\Gamma(2\alpha+2)L^{2\alpha+2}} \frac{e^{\delta z}-1}{e^{\delta z}} \\ & \sum_{m_1=2}^{N-1} e^{-m_1 \delta z} m_1 \sum_{m_2=1}^{m_1-1} \left(\frac{m_2(N-m_2)}{N}\right)^{2\alpha+2}. \end{aligned} \tag{20}$$

We take the thermodynamic limit and approximate the sums as integrals (over $x = \frac{m_i}{N}$ and $dx = \frac{1}{N}$) and expand the result in the low δz limit to obtain:

$$\rho_\omega(\omega) = \frac{\Gamma(2\alpha+5)\Gamma(\alpha+1)^2(\alpha+1)^2}{2(2\alpha+3)\Gamma(2\alpha+2)L^{2\alpha+2}} \frac{\omega^{4\alpha+3}}{\delta z^{2\alpha+4}}. \tag{21}$$

Importantly, this is not just for the smallest mode. Since there are several regions on the ring from which pairs can be chosen, this analysis applies to an extensive fraction of modes. On average, there are $N\delta z$ regions separated by crossbonded nodes. Therefore, we can apply this analysis for the lowest $N\delta z$ modes of a total N modes, ie. a fraction of modes δz. The density of states is given by $\rho_\omega(\omega) * \delta z$

$$D_\alpha(\omega) = \frac{\Gamma(2\alpha+5)\Gamma(\alpha+1)^2(\alpha+1)^2}{2(2\alpha+3)\Gamma(2\alpha+2)L^{2\alpha+2}} \frac{\omega^{4\alpha+3}}{\delta z^{2\alpha+3}}. \tag{22}$$

Note that $\alpha = 0$, the uniform distribution, is unique in that ω and δz have the same exponent

$$D_0(\omega) = \frac{4}{L^2}\left(\frac{\omega}{\delta z}\right)^3. \tag{23}$$

2.B.3 Full spectrum

In the full spectrum we need to identify the frequency, ω^*, at which the spectrum crosses over into a plateau. In disordered solids, there are ample examples of this cutoff scaling linearly with δz; this is also true for the disordered ring with crossbonds. ω_e only scales linearly with δz for $\alpha = 0$. Therefore it is only for $\alpha = 0$ that the scaling between ω_e and ω^*, ψ is independent of δz.

So the full spectrum of $\alpha = 0$ is given by:

$$D(\omega) = \begin{cases} \frac{4}{L^2}\left(\frac{\omega}{\delta z}\right)^3 & \omega \le \omega_e \\ \left(\frac{4\omega_e^{3-\psi}}{L^2\delta z^3}\right)\omega^\psi & \omega_e \le \omega \le \omega^* \\ c & \omega^* \le \omega \end{cases}. \tag{24}$$

In practice, ψ is consistent with 4.

δz	ψ
0.1	4.0761
0.168	4.0115
0.282	3.9606
0.476	3.9496
0.8	3.9749

Table 1: The best fit power law for the intermediate regime as a function of excess contacts for the uniform distribution of bond weights.

2.B.4 Behavior of sloshing modes

The value of the IPR for a sloshing modes depends explicitly on the distance between the active bonds. If the active bonds are separated by m particles the IPR is given by

$$IPR = \frac{1}{m} + \frac{1}{N-m} - \frac{3}{N}. \tag{25}$$

Thus the increasing of the IPR plateau with δz in the sloshing regime is indicative of a decrease in the distance between active bonds. By construction of the crossbonded system, the distance between active bonds is limited by the distance between crossbonded nodes, which decreases with δz.

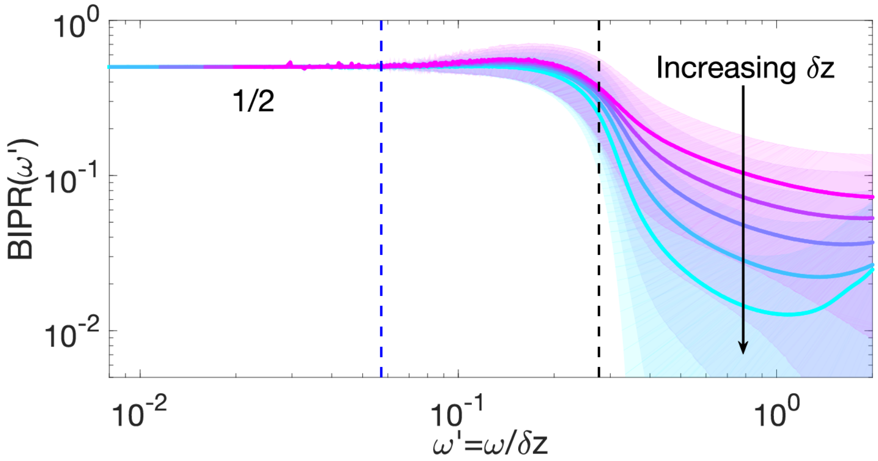

Figure 17: The BIPR rescaled by δz. The blue dashed line indicates ω_e while the black dashed line indicates ω^*

We can also measure the participation of the bonds with what we call the Bond Inverse Participation Ratio (BIPR):

$$BIPR(\omega) = \frac{\sum_{(i,j)}(v_i - v_j)^4}{(\sum_{(i,j)}(v_i - v_j)^2)^2}, \tag{26}$$

where (i, j) is an edge in the network. In the limit of low frequency, there is a plateau of $BIPR = \frac{1}{2}$ which indicates that only 2 bonds are extending or compressing for the modes in that regime. This is secondary confirmation that the sloshing mode assumption is reasonable for this simple model.

3 A self-propelled particle model for collective motion in dynamic crowds

Abstract

Unstable and active disordered materials exhibit interesting collective properties and nontrivial dynamics. While the behavior of amorphous solids under shear is relatively well-understood, instabilities that occur in active systems remain difficult to characterize and predict. In the context of dense crowd dynamics, existing work has analyzed position fluctuations in a self-propelled particle (SPP) model to identify Goldstone modes and soft spots in models for human crowds. This analysis requires time-resolved trajectory information in order to form predictions for collective behavior, which can be cumbersome. To address this issue, we have developed a novel method to generate static, finite packings in an artificial potential that reproduce the packing structures observed in a class of point-of-interest active SPP crowd simulations. These static packings then allow us to precisely identify local structural defects that govern dynamical group behavior, so that we can predict the locations of rearrangements and instabilities in dense, active SPP models. Unlike previous methods, these predictions can be derived from a single snapshot and could be relevant to preventing dangerous emergent phenomena in real crowd systems.

3.1 Introduction

In recent years, the study of the collective motion of systems comprised of active or self-propelled constituents has attracted interest from communities of physicists, biologists, and sociologists. This is because an understanding of this collective behavior is fundamentally important to many physical and biological systems across a wide range of length and activity scales including active colloidal particles, bacterial suspensions, biological tissues, flocks of birds, and the focus of this work: crowds of people [19, 22, 99–105]. Models for these active systems in simulations are very similar to molecular dynamics simulations, where motion is controlled by interactions between constituent particles, but particles in active systems are driven by an additional active force that propels each particle [101, 102]. In living systems, these interactions between constituents are often not mechanical but social in nature [101, 106, 107]. For instance, when birds form a flock they typically don't crash into each other to determine the direction of the flock [101]. Rather birds can see where their neighbors are moving and adjust their flight to align with them [101, 107]. For models of crowds of people, in particular, the constituent "particles" are self-propelled by walking, and models typically assume some interaction forces due to social rules like collision avoidance and staying near or aligning with some in-group of people [108, 109]. Although these models of social interactions are simplifications of human behavior, they qualitatively reproduce many emergent crowd dynamics such as the formation of unidirectional lanes and stop-and-go waves [22, 109]. Unfortunately, although these methods are quite good for low-density crowds where individuals are free to move towards an intended destination, a qualitative description remains elusive for collective motion in high-density crowds [104].

In extreme situations like riots or concerts, typical social forces break down as a large number of people become packed into a confined space [104]. This can be very dangerous; many people are crushed or trampled when a crowd undergoes a sudden collapse [104]. For instance, recently a human stampede during Madagascar's independence day celebration resulted in 15 people dead and 80 injured when a crowd of thousands attempted to push into a stadium [110]. It is believed that this stampede occurred because members of the crowd far from the stadium believed the stadium gates were open and began to push forward. However, there was nowhere for the crowd to go so the people towards the front of the crowd were under increasing pressure until eventually there was a collapse.

For these high-density crowds, the primary features that govern the collective motion of a crowd are the physical interactions between the members of the crowd and the movement of individuals towards a stage, a door, or some other point of interest [22]. At high densities, these crowds are no longer fluid-like and are instead better described using tools from the physics of granular solids [22, 104]. Recent work has focused on active matter models for human collective motion without terms related to social interactions [22, 104]. This model for human collective behavior is asocial, where the only forces considered are those from the physical interactions between the constituent members and the self-generated force that directs members of the crowd towards a point of interest. We also include random forces to capture noise or motion not directed toward a point of interest [22].

The primary goal of these models is to determine structural precursors to identify the location and time of a potentially dangerous rearrangement in the crowd before they occur [22]. Predictions of where the crowd will collapse or rearrange have previously involved computing the displacement correlation matrices for noisy simulations [22, 111]. This requires watching the motions in the crowd over some time window using the relative motions and correlations to determine the effective interaction potential between individuals in the crowd [111]. The rationale for studying displacement correlations comes from thermalized colloids. For colloidal systems where fluctuations are driven by thermal temperature, one can show that, provided there are no rearrangements so particles are confined to a cage by their neighbors, the infinite time limit of the displacement correlation matrix can be mapped to the linear response [22, 111]. However, it is not at all clear that such a relationship holds in human crowds where fluctuations are not thermal and rearrangements are common.

Next we want to use this information to predict rearrangements and instabilities in crowds. In a granular system, there are a number of structural measures, that have proven to be useful to predict rearrangements [35–37, 55, 112, 113]. Many of the best measures rely on the linear response of a stable packing to predict soft regions where the energy barrier to rearrangements can be low [113]. One such measure has used an approximation to the linear response, based on the displacement correlation matrix, to predict soft spots in the crowd [22]. Given the challenges highlighted above, it would be useful to have a better method to approximate the linear response. Moerover, such an analysis could be quite general and could be useful in situations other than human crowds. It could be used to model self-propelled colloidal particles in a chemical gradient, animal herds, or even nascent formation of asteroids in microgravity. However, it has not previously been possible to directly compute the linear response in a self-propelled system due to the presence of non-conservative forces [114].

To address this challenge, here we demonstrate that, in the limit where the noise contribution to the forces on individuals is negligible, we can exactly predict the linear response of a self-propelled system using a static model of passive particles augmented by an external potential. In this framework, we compute linear response to predict regions of rearrangement when the system is perturbed by noise, as in other granular systems. Our aim is to predict where people are in danger in a crowd from a single static picture of a crowd rather than an analysis of random crowd motion over time.

3.2 Model

Following previous human collective motion studies [22], we model the individuals in the crowd as simple soft-sphere particles with a self-propulsion velocity, v_0, biased towards some fixed point of interest. Particles in this system interact with a Hertzian contact potential where the potential energy as a function of distance is given by

$$V_{ij}(r_{ij}) = \frac{2k}{5}\left(1 - \frac{r_{ij}}{r_i + r_j}\right)^{5/2}, \tag{27}$$

where k is the energy scale associated with the contact potential, r_{ij} is the distance between particle i and j and r_i and r_j are the radii of particles i and j respectively [115]. In two dimensions, these systems will crystallize if there is no size disparity between constituent particles. Therefore, we simulate a binary system comprised of two species of particles with a size ratio of 1:1.4 to suppress crystallization as the system is compressed [17].

In addition to the interaction between particles, every particle has a self-propulsion velocity, v_0. The direction of self propulsion in most self-propelled systems is either randomly chosen or biased due to alignment with neighboring actors such as birds in a flock aligning with each other. By contrast, in our simulation, the self-propulsion velocity is biased towards a point of interest. Without loss of generality, we choose this point of interest to be the origin. The self-propulsion velocity has constant magnitude v_0 and moves along the unit vector, $\hat{n}_i$, which is oriented at an angle θ with the positive x-axis. Over time, this vector turns towards the attracting point on a characteristic time scale such that particles not initially facing the point of interest will turn to approach it. In this work, we choose this time scale to be vanishingly small, such that particles instantly orient themselves to propel toward the attractor such that $\hat{n}_i = -\hat{r}_{ia}$, where $\hat{r}_{ia}$ is the unit vector that points from the attractor to particle i.

The net velocity on a particle is computed as the self-propulsion velocity plus the interaction forces multiplied by some damping coefficient, Γ, which we set to unity:

$$\overrightarrow{v}_i(t) = v_0 \hat{n}_i(t) + \Gamma \overrightarrow{f}_i(t), \tag{28}$$

where $\hat{n}_i$ is the self propulsion velocity that, in this case, points from the particle i towards the attaractor at time t and $\overrightarrow{f}_i$ is the net force on particle i at time t. As the magnitude of the velocity and the radii sets the timescale, we choose v_0 and the radius of the small particles to be unity. We further choose the energy scale associated with the contact potential to be $k = 1000$ such that the overlap of particles is below 1% of the radius of the particles when driven together by self-propulsion.

We initialize the positions of the particles at very low densities such that few if any particles are interacting. This overdamped self-propelled system, at long times, coalesces into a stable packing where the net force on any particle approaches zero. We then introduce noise to these stable systems, in the form of angular or positional noise to the self-propulsion direction, to investigate random driving behaviors in a crowd from an initial reference configuration.

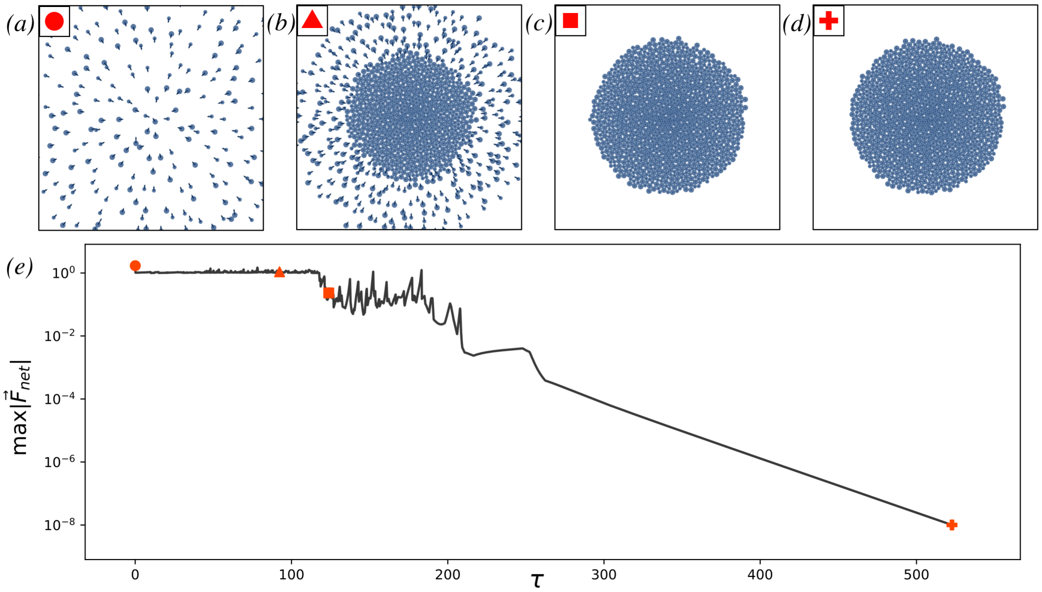

Figure 18: Snapshots of a crowd as it forms over time are shown in A, B, C, and D. E) The maximum unbalanced force in a simulation over time. The red shapes indicate the times at which each corresponding snapshot of the crowd was taken.

3.3 Symmetry-broken active particle simulations form static packings

In the noiseless limit, the self-propelled particle simulation where particles are biased towards a point of interest forms a static configuration at long times. Initially, no particles are in contact as shown in Fig. 18 A. In this configuration, the net force on any given particle–and therefore the velocity–is only the self propulsion velocity, v_0. In a subset of these simulations, a particle comes within a threshold of X to the attractor and we pin that particle to the attractor for numerical stability. We have confirmed that simulation with and without pinned particles exhibit the same behavior. Over time, members of the crowd begin to come into contact as the crowd coalesces. However, the maximum unbalanced force is still given by the particles that have yet to join the main crowd, the self-propulsion velocity. This coalescence is shown in Fig. 18 B where many members of the crowd are still isolated from each other.

After all members join the main crowd cluster, like the snapshot shown in Fig. 18 C, the maximum net force can vary wildly as the system undergoes rearrangements while compressing towards the point of interest. Finally, after a long period of time, the system stops rearranging and the maximum net force begins to decrease until the force is within precision limitations. In other words, at long times the noiseless simulations form stable jammed packings with no external boundary conditions. To our knowledge, this is the only active matter system that forms a stable solid, which is possible due to the broken symmetry.

The static configurations, like the one shown in Fig. 18 D, are circular crowds centered at the point of interest. In this limit, the self-propelled particle simulation is equivalent to steepest descent in an external potential where the external potential is a constant force pointing towards the point of interest. The total energy from this external potential is given by

$$U_{ext} = v_0 \sum_i r_{ia}, \tag{29}$$

where r_{ia} is the distance from the attractor to particle i. This implies tools from jammed packings can be useful to make predictions about the motion in the crowd.

3.4 Modified linear response in an external potential

We consider a generic example where the external potential only depends on the particle position. Let the potential be defined as

$$\mathcal{U} = \frac{1}{2} \sum_i \sum_{j \in \partial i} V(r_{ij}) + \sum_i V_e\left(\overrightarrow{x}_i\right), \tag{30}$$

where ∂i is the neighborhood of particle i, $\overrightarrow{x}_i$ is the position of particle i, and $V_e\left(\overrightarrow{x}_i\right)$ is the external potential. The first derivative is given by

$$\frac{\partial \mathcal{U}}{\partial x_{i\alpha}} = \sum_{j\in\partial i}\left(V'(r_{ij})\frac{\partial r_{ij}}{\partial x_{i\alpha}}\right) + \frac{\partial V_e\left(\overrightarrow{x}_i\right)}{\partial x_{i\alpha}}. \tag{31}$$

This force has a contribution from internal forces and a second term from the external interaction. It is crucial to note that this external force on particle i is only dependent on the position of particle i relative to the external point.

We now consider the Hessian itself to investigate the symmetry directly. The Hessian is given by

$$H_{ij\alpha\beta} = \frac{\partial^2 \mathcal{U}}{\partial x_{i\alpha}\partial x_{j\beta}} = \begin{cases} \sum_{k\in\partial i}\left(V''(r_{ik})\frac{\partial r_{ik}}{\partial x_{i\alpha}}\frac{\partial r_{ik}}{\partial x_{i\beta}} + V'(r_{ik})\frac{\partial^2 r_{ik}}{\partial x_{i\alpha}\partial x_{i\beta}}\right) & \\ \qquad + V''(r_{ei})\frac{\partial r_{ei}}{\partial x_{i\alpha}}\frac{\partial r_{ei}}{\partial x_{i\beta}} + V'(r_{ei})\frac{\partial^2 r_{ei}}{\partial x_{i\alpha}\partial x_{i\beta}} & i = j \\ V''(r_{ij})\frac{\partial r_{ij}}{\partial x_{i\alpha}}\frac{\partial r_{ij}}{\partial x_{j\beta}} + V'(r_{ij})\frac{\partial^2 r_{ij}}{\partial x_{i\alpha}\partial x_{j\beta}} & j \in \partial i \\ 0 & Otherwise \end{cases}. \tag{32}$$

This is equivalent to the Hessian due to the internal interactions, with an addition of an external term to the self-interaction blocks, $H_{ii\alpha\beta}$. Or with an external potential,

$$H_{ii\alpha\beta} = -\sum_j H_{ij\alpha\beta} + \frac{\partial V_e\left(\overrightarrow{x}_i\right)}{\partial x_{i\alpha}}\frac{V_e\left(\overrightarrow{x}_i\right)}{\partial x_{i\beta}} + \frac{\partial^2 V_e\left(\overrightarrow{x}_i\right)}{\partial x_{i\alpha}\partial x_{i\beta}} \tag{33}$$

Therefore, $H_{ii\alpha\beta} \neq -\sum_j H_{ij\alpha\beta}$ in the presence of any generic external potential, as the only requirement is that the external potential only depends on the position of one particle relative to some important point. It does not require that this external potential be applied to all particles, as a single particle with an external potential is enough to break the global translational symmetry.

To tailor this generic result to the noiseless SPP model described in the previous section, when all particles experience a velocity directly towards the attractor, we represent the attracting force as the center of a constant force spring potential:

$$V_a(r_{ia}) = \frac{v_0 r_{ia}}{\Gamma} \tag{34}$$

where v_0 is the self-propulsion velocity, Γ is the damping coefficient, and r_{ia} is the distance between particle i and the attractor. This attracting potential breaks translational symmetry for all particles and results in an athermal static packing of particles without walls to confine the particles for the usual jamming transition.

We find the force on each particle due to its interactions and the biased self-propulsion force:

$$F_{i\alpha} = -\frac{\partial \mathcal{U}}{\partial x_{i\alpha}} = -\sum_{j\in\partial i}\left(V'(r_{ij})\frac{\partial r_{ij}}{\partial x_{i\alpha}}\right) - V_a'(r_{ia})\frac{\partial r_{ia}}{\partial x_{i\alpha}} = F_{int,i\alpha} + \frac{v_0}{\Gamma}\hat{r_{ia\alpha}}, \tag{35}$$

where $\hat{r_{ia\alpha}}$ points from particle i to the attractor. The attractive force on a given particle is critically only dependent on that particle's position relative to the attractor. To compute the linear response of the system, we need to find the second derivative of the energy relative to particle displacements relative to some reference configuration at mechanical equilibrium.

When we compute the dynamical matrix, the off-diagonal elements depend only on the particle interactions but the on-diagonal or self-interaction terms depend on the particle interactions as well as the external potential proportional to v_0:

$$M_{ij\alpha\beta} = \frac{\partial^2 \mathcal{U}}{\partial x_{i\alpha} \partial x_{j\beta}} = \begin{cases} -\sum_{k \in \partial i} M_{ik\alpha\beta} + \frac{v_0}{r_{ia}} \left(\delta_{\alpha\beta} - \hat{r_{ia\alpha}} \hat{r_{ia\beta}} \right) & i = j \\ V''(r_{ij}) \frac{\partial r_{ij}}{\partial x_{i\alpha}} \frac{\partial r_{ij}}{\partial x_{j\beta}} + V'(r_{ij}) \frac{\partial^2 r_{ij}}{\partial x_{i\alpha} \partial x_{j\beta}} & j \in \partial i \\ 0 & Otherwise \end{cases} . \tag{36}$$

This alteration to the self-interaction block can dramatically effect the linear response of the system, as can be seen by the fact that this configuration is stable without walls. We compute the vibrational modes of the passive system via diagonalization of this dynamical matrix. This change in the vibrational spectrum due to the external potential alters the predictions where rearrangements are likely to occur. In our crowd model, the eigenvectors of this altered spectrum can be used to identify “soft spots” in a crowd which are susceptible to deformation. It uses only information from a static configuration rather than a long-time average of motion within the crowd, which may improve our ability to quickly identify dangerous places in the crowd.

3.5 Structural gradients of static crowds

Most glassy and jammed systems have been studied in a regime where there are no strong spatial gradients in the material properties. By contrast, crowds are more like sand piles or sedimenting granular systems where there are strong gradients. For instance, there is a pressure gradient with high pressure towards the center and low pressure on the boundary. In Fig. 19 A, we show the decrease of pressure on individual particles throughout the crowd with a dramatic decrease near the boundary of the crowd.

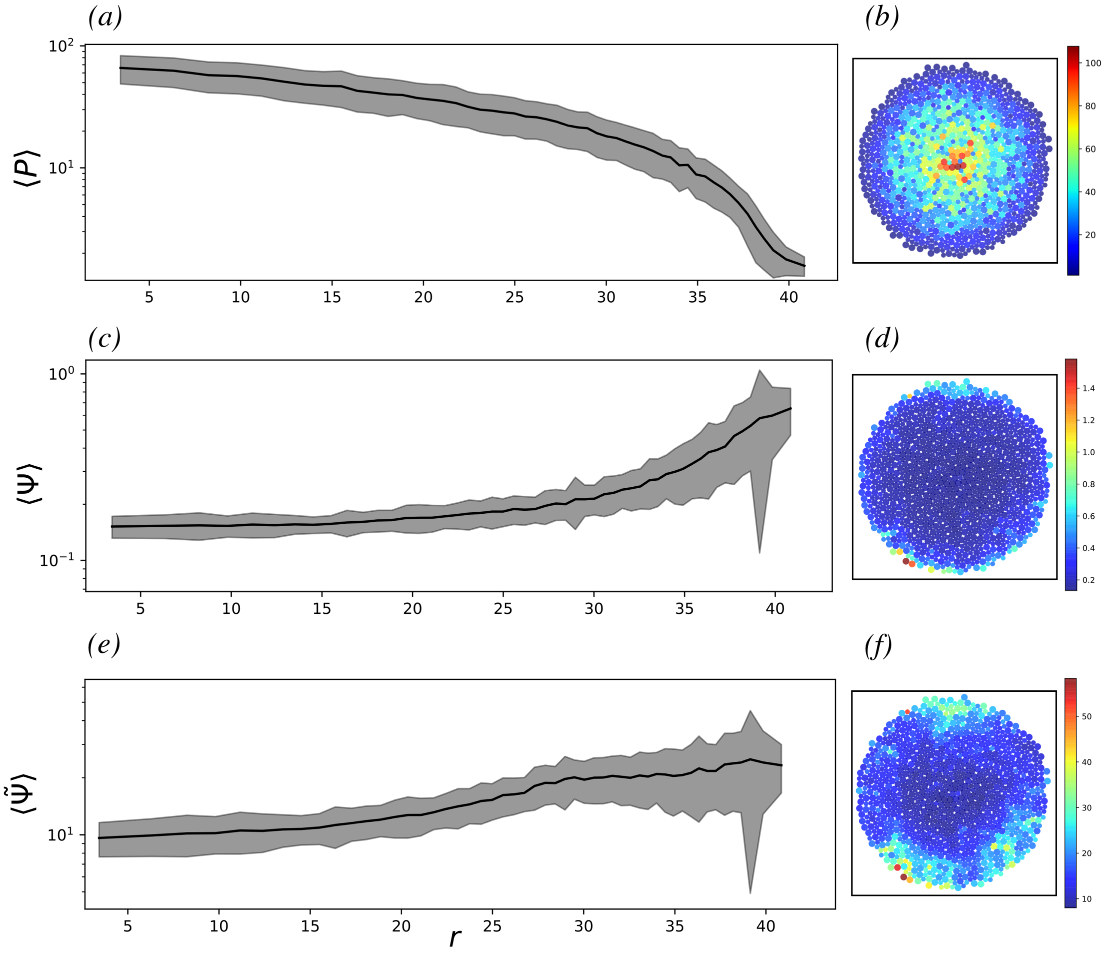

Figure 19: A) Pressure on members of the crowd as a function of radius averaged of 15 crowds. B) A sketch of the pressure in an example crowd. C) Vibrability on members of the crowd as a function of radius averaged of X crowds. D) A sketch of the vibrability in an example crowd. E) Non-affine vibrability on members of the crowd as a function of radius averaged of 15 crowds. F) A sketch of the non-affine vibrability in an example crowd.

In systems with external forces, pressure gradients can form to counteract the external force. For instance, the atmospheric pressure decreases as altitude increases to counteract the force due to gravity [116]. Similarly, the particles toward the center of the crowd must support not only their own "weight" due to self-propulsion towards the attractor but also the weight of all the particles behind them. By contrast, in the absence of external forces, a region of high pressure pushes particles outward into regions of lower pressure until the pressure equalizes throughout the system. Stable configurations in most material systems have a uniform pressure as a consequence of mechanical or thermal equilibrium.

In addition, there are structural gradients that arise from the external potential of this system. For instance, we use the dynamical matrix for interacting particles in an external potential to compute vibrational modes and structural metrics related to these modes. The vibrability uses vibrational modes to compute the propensity of mean square displacement in a particle packing as temperature is added to the system in the limit of very low temperatures [117]. The vibrability on particle i is computed from the vibrational modes:

$$\Psi_i = \lim_{T \to 0} \frac{\partial}{\partial T} \langle |\vec{u}_i|^2 \rangle = \sum_q \frac{|\hat{v}_{q,i}|^2}{\lambda_q}, \tag{37}$$

where $\vec{u}_i$ is the thermal displacement of particle i, λ_q is the q^{th} eigenvalue, $\hat{v}_q$ is the associated eigenvector, and $|\hat{v}_{q,i}|^2$ is the squared magnitude of the eigenvector on particle i. On the boundary there is little to restrain the particles from moving when thermal energy is added as the density and pressure are lower. Fig. 19 D shows the vibrability field of a crowd, which exhibits large vibrability near the surface. However, the vibrability gradient shown in Fig. 19 C penetrates deeper into the crowd than one layer of particles.

In addition to quantifying the likelihood of particles moving, researchers in granular physics are generally interested in where rearrangements are likely to occur. In the context of a crowd model, such rearrangements could be correlated with dangerous events. These rearrangements are identified as peaks in the locally non-affine motion defined by the D^2_{min} [26]. Therefore, we introduce the non-affine vibrability as a measure of the propensity for non-affine motion as temperature is added to the system:

$$\tilde{\Psi}_i = \lim_{T \to 0} \frac{\partial}{\partial T} \langle D^2_{min,i} \rangle = \sum_q \sum_{j \in \partial i} \frac{|\hat{v}_{q,j} - \hat{v}_{q,i}|^2}{\lambda_q}, \tag{38}$$

where ∂i is the neighborhood of particle i defined to be all particles within 5 particle radii of particle i. Preliminary, it seems there is a plateau in the radial gradient of the non-affine vibrability shown in Fig. 19 E, beginning at around $r = 30$ for a system of size 1024. Visually, this plateau is associated with a lighter-colored ring surrounding a dark core in the non-affine vibrability field shown in Fig. 19 F. This suggests there could be qualitatively different rearrangement behavior in the border region compared to the interior.

3.6 Gradients in thermalized active packings

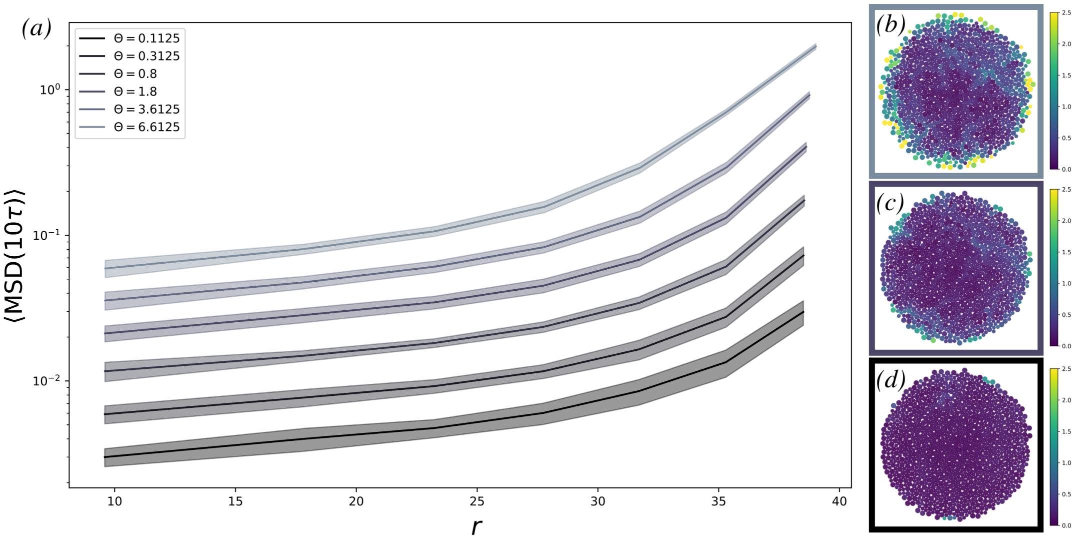

Figure 20: A) The mean squared displacement at 10 τ as a function of radius for 6 different effective temperatures. B, C, and D are snapshots of a thermally active crowd at 10 τ at effective temperatures 6.6125, 1.8 and 0.1125 respectively.

Beginning from a stable configuration, we introduce thermal translational noise to model random agitation in a crowd. The velocities of members of the thermalized crowd over time are given by

$$\overrightarrow{v}_i(t) = v_0\hat{n}_i(t) + \Gamma\overrightarrow{f}_i(t) + \overrightarrow{\eta}_i(t), \tag{39}$$

where $\overrightarrow{\eta}_i$ is the thermal noise added to the motion of the particle. This noise is uncorrelated, gaussian white noise vector with magnitude σ^2,

$$\langle\overrightarrow{\eta}_{i,\alpha}(t)\overrightarrow{\eta}_{j,\beta}(t')\rangle = \sigma^2\delta_{ij}\delta_{\alpha\beta}\delta(t-t'). \tag{40}$$

In overdamped, thermal, molecular dynamics simulations of particulate systems, at vanishingly low density, the diffusion constant, $D = \frac{\sigma^2}{2}$, is related to the physical temperature via $\frac{\sigma^2}{2} = \frac{k_BT}{\Gamma}$ where Γ is the drag coefficient. We have previously chosen the drag coefficient to be 1; therefore, the thermal energy scale, k_BT, as a function of the standard deviation of the translational noise is given by $\frac{\sigma^2}{2}$. We define a unitless effective temperature by comparing the thermal energy scale with the interaction energy scale

$$\Theta = \frac{\sigma^2}{2k}, \tag{41}$$

where k is the spring constant (energy) associated with our interparticle potential.

As thermal energy is added to the system, we measure the mean squared displacement of particles after 10 natural time units, τ, which is a local measure of the motility. Fig. 20 A shows the gradient of motility as a function of radius for six different temperatures, highlighting an increase to the mean squared displacement as radius increases. Particles near the center are more strongly caged than particles on the boundary. As temperature increases, the motility increases, but not uniformly. Particles on the boundary, which already move more than those near the center, experience a greater increase to their motility at higher temperatures.

This strong gradient in the mean square displacement is illustrated in Fig. 20 B showing the motility field for the highest temperature, $\Theta = 6.6125$. This strong gradient clearly indicates localization of motility on the particles just at the boundary. As the temperature is decreased to $\Theta = 1.8$ and $\Theta = 0.1125$, shown in Fig. 20 C and D respectively, the overall intensity decreases. These changes are consistent with the vibrability gradient noted in the previous section.

3.7 Continuing work

Models for thin films are similar to our model crowds in that they have a free boundary, but they lack an external force that confines the particles to the film [118]. Therefore, in order for thin films to have a free boundary, there must be an attractive portion to their interaction potential, such as the Lenard-Jones potential. Films formed from these attractive particles have weak pressure and softness gradients only near the surface, but the motility gradient penetrates quite far into the depth of the packing, further than the softness and relaxation gradients. This motility gradient, even in regions of constant pressure and softness, has been explained in terms of activated or Arrhenius processes where the overall rate, R, is given by

$$R = \omega e^{-\frac{\Delta E}{T}}, \tag{42}$$

where ω is the attempt frequency and ΔE is the energy barrier in the potential energy landscape. Previous work has demonstrated that the pressure and softness set the height of the energy barriers associated with rearrangements, while the distance to the surface controls the attempt frequency [118]. Both softness and the energy barriers are relatively constant in the bulk of the thin film, while the attempt frequency is much larger towards the edge of the thin film due to the lack of constraints on particles on the surface.

In our system, not only do we have the free boundary found in thin films, but we also have strong gradients in pressure and softness that penetrate through the bulk of the system. This would suggest that active particle crowds could have strong gradients in energy barriers associated with rearrangements in addition to the gradient in attempt frequency from the surface of the crowd. This feature could result in enhanced motility gradients due to the softness gradients.

We are currently working to disentangle the effects of these structural gradients to extract the gradients in energy barriers and attempt frequencies. Specifically, we are investigating how much of the motility gradient and the related rearrangement probability gradient is due to the open boundary versus having pressure gradients or softness gradients.

Additionally, we are investigating how the gradients in pressure, structure, and motility interact. For instance, since pressure and softness are anti-correlated in packings without gradients, is the vibrability gradient caused by the pressure gradient generically.

3.8 Discussion

In this chapter, we propose a symmetry-broken self-propelled particle (SPP) model that, in contrast to typical SPP systems, produces force-balanced granular packings. These packings exhibit strong radial pressure gradiant and a free boundary. Through modification of the dynamical matrix used to evaluate linear response measures with a simple external potential, we also found these packings demonstrate strong radial gradients in structural measures of softness such as in the vibrability and nonaffine vibrability. We also contrast our work to existing studies on crowd dynamics, as our novel approximation for the linear response of the system does not rely on the dynamics of individual particles evaluated over time.

Our model produces force-balanced, stable packings of self-propelled particles with a systematic bias towards a central point. We evaluate the stable packing formed in this way by modelling the self-propulsion as an external potential, allowing us to compute the linear response and vibrational spectrum of an active material, which, to our knowledge, is the first time this has been possible. These crowds show strong pressure gradients as well as structral gradients found with the vibrational spectrum such as the vibrability. These gradients are not observed in bulk glassy systems or other active matter models.

When thermal translational noise is added to the dynamics, we investigate how these gradients can be related to particle motility. Similar to results in thin glassy films, we observe a motility gradient that penetrates into the depth of the packing. However, we are still investigating how this gradient arises from structural properties of the packing and free boundary effects.

We seek to answer questions related to the interplay of gradients in our system. How much is the observed motility gradient caused by structural and free boundary effects? Does the presence of the strong pressure gradient reinforce a coupling between structure and dynamics that is not present in thin films? We study this by investigating the functional dependence of particle rearrangement probabilities on variables such as nonaffine vibrability and pressure. There are also interesting and socially relevant applications of this work which include investigating choices of external boundaries which inhibit potentially dangerous crowd motility.

4 Avalanche dynamics in athermal systems

Abstract

Under applied shear strain, granular and amorphous materials deform. At zero temperature, the deformation can be separated into elastic branches where the particles do not change neighbors and rearrangements where they do. Some rearrangement events are small and localized, while others involve large or system-spanning avalanches. Using numerical simulations of soft spheres, we find that avalanches can be decomposed into a series of bursts of localized deformations, and we develop an extension of persistent homology to isolate these bursts of localized deformations. Next, we develop a method to study the linear response of unstable systems during an avalanche, by extending existing tools for identifying structural defects using the Hessian and study how the population of structural defects evolves during an avalanche. We find that bursts of localized deformations in the avalanche correlate strongly with localized excitations in the linear spectrum. These data should help to constrain elastoplastic models for glasses and granular matter.

4.1 Introduction

Can we predict how amorphous materials, such as sand, mud, bulk metallic glasses [20, 119], colloidal suspensions [120], foams [121, 122] fail under stress? This question is important in many diverse fields from statistical physics to material science to geophysics where one hopes a fundamental explanation of this response will allow one to control failure mechanisms, such as shear band formation and avalanche dynamics [119]. Avalanches in granular systems, like rock- and mud-slides, are potentially deadly examples of this catastrophic failure phenomenon in relatively soft materials. It is crucial to understand these system-spanning rearrangements to be able to predict when and where they are likely to occur and, if possible, find methods to prevent such failure modes in manufactured materials. For instance, bulk metallic glasses are stronger and more elastic than their crystalline counterparts which would seem to make them excellent candidates for structural materials [20]. However, unlike the ductile bending of steel and other metals, when these materials fail, they fail catastrophically [20, 123]. A better understanding of the underlying mechanisms of this failure could, in principle, give material scientists the tools to better predict failure which would allow replacement or repair before the failure occurs.

Under small deformations or forces, amorphous materials respond like elastic solids where the shear stress increases with strain, although small rearrangements can occur in this regime [124]. Above some critical threshold in stress or strain, amorphous materials typically yield in irreversible plastic deformations, and the resulting macroscopic stress-strain curve approaches a constant [124]. However, different materials exhibit vastly different behaviors during this yielding transition [124]. Soft, ductile materials like foams and emulsions yield in a smooth and gradual process as the system begins flow under stress [125]. On the other hand, when hard, brittle materials cross this critical threshold, they tend to yield abruptly and catastrophically via crack, shear band, or avalanche. [119, 125]. Unfortunately, it remains unclear what micro- or meso-scopic features govern this brittle-to-ductile transition. Previous work on athermal avalanches have largely focused on systems under athermal quasistatic shear, where configurations are analyzed before and after the system spanning rearrangements [126, 127]. A few works have also focused on packings sheared under finite strain rate [127]. These studies evaluate the size, statistics, and shape distribution of these avalanches as a function of material preparation and material properties, with a specific focus on the ductility of the initial configuration [124, 127]. Avalanches in ductile systems are typically not well organized in space and can occur with relatively little energy imparted to the system. Brittle systems, however, exhibit shear bands, which can be viewed as avalanches that organize along a plane in three-dimensional systems or along a line in two-dimensional systems. Several studies of avalanches additionally analyze how the shape and size of these rearrangements depend on dynamic features such as strain rate or inertia [26, 127].

Phenomenological work has focused on understanding the transition from ductile to brittle failure in terms of macroscopic system parameters such as composition, temperature, or preparation [128–130]. Explanations of this brittle-to-ductile transition have been based on analysis from first order transitions in replica theory [129, 131] or directed percolation transitions [132, 133]. Recently some authors have used mesoscopic elastoplastic models to investigate the origin of the transition from a brittle-to-ductile behavior [129, 130]. In these models, it is assumed the system is comprised of independent, mesoscopic yielding regions and that the stress to yield in each region is taken from a specified distribution. This distribution reflects degree of annealing with which the system is prepared. In poorly annealed systems, the average value of this local yield stress distribution is expected to be small, while in well-annealed systems it is large. This hypothesis is strongly supported by work from Patinet et al. [55] who explicitly measure local yield stresses, with some assumptions and caveats, in simulated granular systems.

As an elastoplastic system is strained, the stress in each mesoscopic element increases until the stress in one region surpasses the yield stress and fails, potentially triggering other regions to fail according to a non-positive-definite elastic kernel. At this point, the stress and yield stress for the original failed region are resampled from another distribution. The resulting stress strain curves for different initial yield stress statistics reveal that the qualitative yielding behavior is dependent on the initial stability. Poorly-annealed systems, systems in the shallow minima, have a smooth, ductile yielding behavior while well-annealed systems exhibit brittle failure under the application of stress. As the degree of annealing is decreased, the discontinuous jump in stress at the point of brittle failure becomes weaker until it approaches zero at a particular value of the disorder [29]. This indicates that the variety of yielding behaviors of disordered materials are fairly generic across different types of particle interactions or microscopic dynamics; the transition from soft yielding to sudden catastrophic failure is controlled by the degree of annealing which controls the initial stability of the system [29, 30].

Other models such as Shear Transformation Zone (STZ) and Soft Glassy Relaxation (SGR) also describe localized regions that deform and fail within the glassy systems [25, 27]. These models make similar assumptions about the distribution of soft spots or yield stress throughout the system, but they are mean-field in the sense that the yielding of one region effects the stress everywhere else equally instead of via a non-positive elastic kernel. Moreover, in some versions of these models researchers postulate that there can be local diffusion of softness; rearrangements in one location can cause nearby locations to become soft [125]. At a microscopic level these models assume that plasticity is controlled by "shear transformations", the discrete localized events where a small number of particles rearrange locally, which release the accumulated stress [25, 134]. Similar to elsatoplastic models [130], this implies system-spanning rearrangements such as avalanches or shear bands are expected to occur in bursts of localized motion. The largest difference between models is how these defects are coupled dynamically during an avalanche. Elastoplastic models couple defects by explicitly quadrapolar elastic stress fields while the STZ/SGR models couple defects via local structural changes and noise. In order to test these predictions for coupling between soft spots during avalanches, we first need a robust method for extracting soft spots from unstable amorphous packings.

While plastic deformation in crystalline lattices occurs via dislocations and grain boundaries [135], this picture breaks down in amorphous systems where the concept of a defect is not well defined. However, recently tools have been developed that are fairly accurate in predicting the locations of small localized rearrangements, particularly in soft systems [35, 36, 55, 113, 136, 137]. Several of these measures focus on the linear response while more complex methods have gone beyond linear-order estimation of motion to evaluate the highly nonlinear response near a saddle point or instability.

For instance, the local yield stress developed by Patinet and collaborators quantifies the applied stress required to make a localized region fail. To compute this metric on a particular particle, all particles beyond a fixed distance are forced to move affinely, as in perfectly elastic deformation, while particles within that distance are allowed to relax to minimize their energy. When the particles within the relaxing region fail, the additional stress to failure can be recorded as a function of the angles associated with the applied external shear. The lowest of this set of "stresses to failure" for each region, called the local yield stress, is a direct, non-linear measure of the additional force to make a region fail [55]. Although this method is extremely good at predicting locations of material failure, it is time-intensive to compute and cannot be directly tied to the local structure.

To address these issues, other methods have focused on the linear response. Such measures are computed from the dynamical matrix which determines the linear equations of motion for a stable system and is defined as the matrix of second derivatives of the energy with respect to particle displacements [114]. One of the best measures is the nonaffine velocity, the nonaffine part of the deformation due to the force caused by additional strain [113].

Other structural metrics simply use the lowest energy eigenmodes of the dynamical matrix, or vibrational modes, which are the modes most emphasized in the nonaffine velocity [35, 36, 113]. For instance, the lowest energy vibrational mode just before the instability predicts the motion very well in these isolated rearrangements [36, 37]. Machine learning methods have also been investigated to predict this deformation, but rather than train on the actual motion, these methods have had better success training on this vibrational mode in an effort to find the defect-like structures that trigger rearrangements [112]. However, all of these predictions are notoriously bad at predicting the full deformation field during brittle failure event or a large scale system-spanning avalanches in ductile systems [113].

One obvious reason that linear response measures predict avalanches so poorly is that these measures are computed once before the avalanche, and do not evolve during the avalanche. This is because the dynamical matrix, which governs the linear response of stable systems, has traditionally been used to describe systems in mechanical equilibrium [114]. In this case, the eigenvalues of the dynamical matrix, which describe the curvature of the potential energy landscape are all positive [114]. However, if there is one or more negative eigenvalues, then the system is unstable along the associated eigenvectors. Under athermal quasistatic shear, a rearrangement or avalanche occurs when the lowest eigenvalue transitions from positive to negative at a saddle point in the potential energy landscape [4]. Therefore, it is obvious to ask whether some of the methods for identifying soft spots in positive-definite dynamical matrices can be extended to Hessians describing unstable systems with one or more negative eigenvalues.

In this Chapter, we develop such extensions and calculate soft spots in order to investigate how they evolve over the course of an avalanche. To understand whether we can really describe avalanches as bursts of localized motions, we develop a new method for isolating non-affine movements in the D^2_{min} field [26] described in more detail below using persistent homology to robustly separate an avalanche into a set of localized rearrangements. Finally, we compare these rearrangements to evolving soft spots to understand how soft spots are coupled to generate the observed dynamics. These methods would be useful not only for quasistatically sheared athermal systems, but potentially many other unstable systems such as active matter systems, which may be amenable to similar techniques, or thermal systems which are typically not in mechanical equilibrium.

4.2 Model

The system studied in this paper is a bidisperse granular packing. Particles in this system interact with a Hertzian contact potential where the potential energy as a function of distance is given by

$$V\left(r_{ij}\right) = \frac{2}{5}\left(1 - \frac{r_{ij}}{r_i + r_j}\right)^{\frac{5}{2}} \tag{43}$$

where r_{ij} is the distance between particle i and j, and r_i and r_j are the radii of particles i and j respectively [115]. This binary system is comprised of two species of particles with a size ratio of 1:1.4 in order to suppress crystallization [17]. Two-dimensional systems are initialized with random positions in a square periodic simulation box with equal parts small and large particles. The systems are then instantaneously quenched to zero temperature via FIRE energy minimization [138].

After the quench process, the systems are strained using Lees-Edwards boundary conditions. In this method, the periodic replicas above and below the system are shifted horizontally to impose a simple shear on the simulation box. The speed at which these replicas move relative to the size of the box determines the shear rate of the system. We simulate athermal quasistatic shear (AQS) by taking a small shear step and minimizing the total energy of the system using a FIRE minimization algorithm. Since the system is allowed to relax as long as necessary to find an energy minimum after each shear step, this approximates a strain rate that approaches zero in large systems.

Following each strain step, the shear stress of the minimized configuration is measured. If the instantaneous change in shear stress is larger than a specified threshold, which signifies an instability, we use a linear bisection algorithm to identify the precise strain at which the instability occurs. Using this procedure, we are able to isolate the system just before and just after an instability corresponding to a particle rearrangement.

Once we have identified a particle rearrangement event, we then wish to simulate the dynamics of that event. In athermal quasistatic shear, the minimum energy states are usually identified by fast algorithms that do not correspond to any realistic dynamics such as the conjugate gradient minimization scheme or the FIRE minimization algorithm. To simulate athermal dynamics during an avalanche, we minimize energy using a simple steepest descent algorithm with an adaptive timestep. Despite being one of the most computationally expensive minimization algorithms, this method is equivalent to a noiseless molecular dynamics simulation in the overdamped limit where the velocity is given by the force with some damping coefficient, which we use to define the natural time unit of the system.

4.3 Plastic motion in avalanches occurs in bursts

Plasticity in disordered systems is well captured by the D^2_{min}, a measure of the nonaffine motion [26]. D^2_{min} compares two configurations of a system by measuring the local motion. We choose "local" to be within five particle radii from a central particle because this captures next nearest neighbors, and previous work suggests the core of localized rearrangements typically involve 15-20 particles. This is computed as a scalar value on each particle, i, with

$$D^2_{min,i}\left(\overrightarrow{X}_1, \overrightarrow{X}_2\right) = \sum_{j: r_{ij} < 5\bar{r}} \left(\overrightarrow{r_{ij}}_2 - \mathbf{S}\overrightarrow{r_{ij}}_1\right)^2 , \tag{44}$$

where $\overrightarrow{X}_1$ and $\overrightarrow{X}_2$ represent the two configurations being compared, r_{ij} is the distance between particles i and j, $\bar{r}$ is the average particle radius, $\overrightarrow{r_{ij}}_1$ and $\overrightarrow{r_{ij}}_2$ are the vectors that separate particles i and j in the first and second configuration respectively, and $\mathbf{S}$ is the best fit affine transformation that minimizes $D^2_{min,i}$. The D^2_{min} is measured in units of distance squared.

Typically, for quasistatically sheared systems, the configurations to be compared are separated by strain where one configuration is obtained by straining some reference configuration. If the system has deformed elastically between the two configurations, the measured D^2_{min} is negligible as elastic motion is usually locally affine in granular materials. If, however, there is some plastic deformation between the two configurations, the D^2_{min} will highlight the region in which the deformation took place as plastic deformation cannot be well described by an affine transformation.

Unlike previous studies, our goal is to measure instantaneous plasticity over time. Therefore, we measure D^2_{min} between two configurations separated by a small time window throughout the minimization. The bursts of localized deformation we want to focus on have a duration on the order of one natural time unit, so we choose to measure the plasticity over a time window, Δt, of 0.2 time units to obtain good resolution. We denote the plasticity measured at time t with

$$D^2_{min,i}(t) = D^2_{min,i}\left(\overrightarrow{X}\left(t - \frac{\Delta t}{2}\right), \overrightarrow{X}\left(t + \frac{\Delta t}{2}\right)\right) \tag{45}$$

where $\overrightarrow{X}(t')$ is the configuration at time t'. This measure is a scalar field measured on each particle over space and time. Examples of the D^2_{min} during one avalanche are shown in Fig. 21 A, B, and C.

As shown in Fig. 21 D, the maximum value of the D^2_{min} shows clear bursts of motion where the maximum value increases by orders of magnitude rapidly and decreases just as quickly. Furthermore, the fields shown in Fig. 21 A, B, and C, chosen because they are the peaks of the three largest bursts of motion, show the location of the particles that are responsible to these bursts of motion are different for each burst.

One thing to note is the time at which these bursts start. The first burst doesn't begin, in this example, until 868 natural time units after minimization starts. Leading up to that point there is very little motion or interesting activity to note. The reason for this delay time is the system begins very near the saddle point instability that triggers rearrangement. Near this saddle point the net force on the system is very small and since the velocity in steepest descent is given by the force, the velocity is also small. It takes time for the system to leave the saddle point behind and approach the region of interest. Similarly, after all the

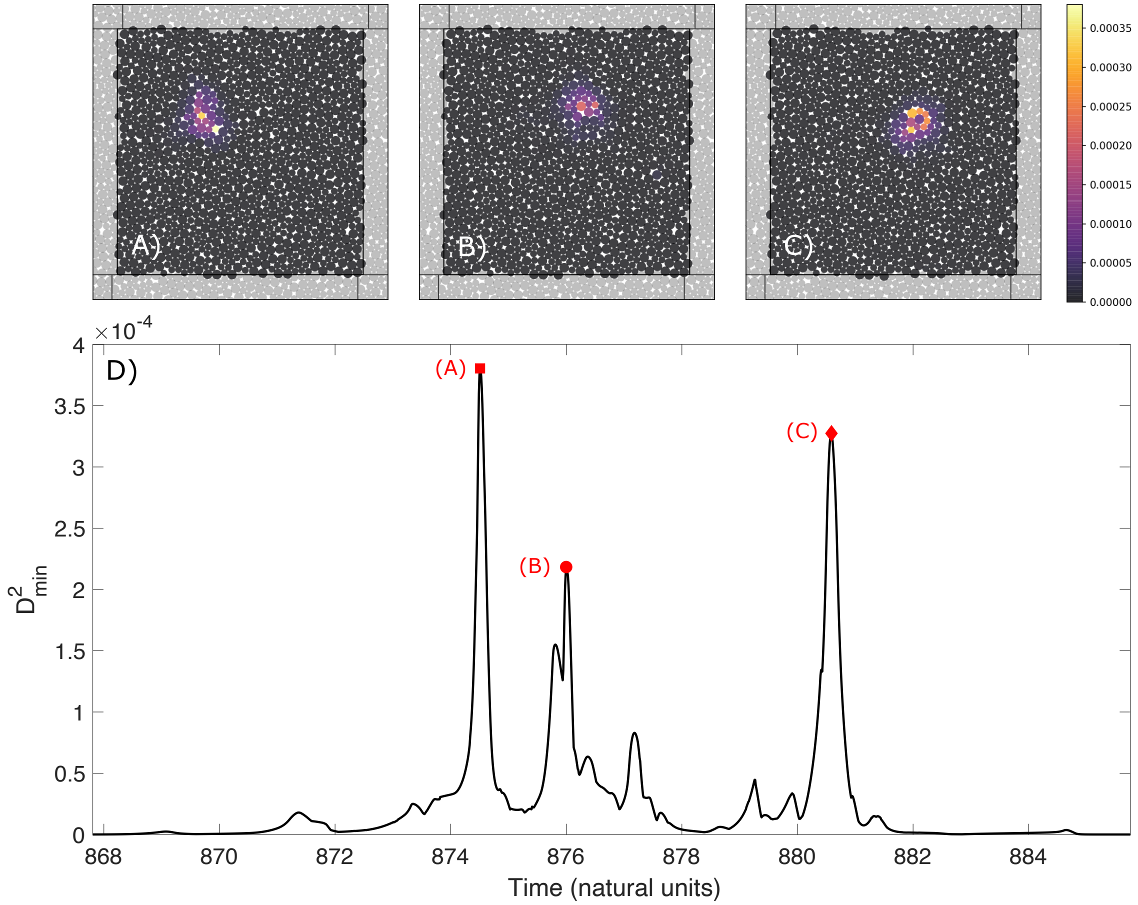

Figure 21: Snapshots of the D^2_{min} field over time are shown in A, B, and C. D) The maximum D^2_{min} as a function of time for an example avalanche. Red symbols indicate the times at which the snapshots were extracted.

rearrangements have finished, the system relaxes to a minimum and becomes increasingly slow as it approaches. These build-up and relaxation phases take up the bulk of the time during steepest descent minimization, taking on the order of hundreds or thousands of time units, while the system only rearranges for on the order of tens of time units for the system sizes we study.

4.4 Avalanches can be decomposed into bursts of localized deformation

It appears that the bursts of localized motion are localized to relatively small groups of particles. To investigate this, we introduce a novel clustering algorithm taking inspiration from Persistent Homology and hierarchical density-based clustering methods.

Our goal is to highlight isolated peaks in the nonaffine motion in this system over space and time to quantify whether the motion during an avalanche occurs in localized bursts. The simplest picture one could imagine is applying a plain threshold on the nonaffine motion. However, it is clear that applying a bare threshold to a function could easily lose important peaks and may not well separate the most active peaks and, furthermore, this kind of clustering is very sensitive to the threshold value which must be determined arbitrarily.

By contrast, persistent homology is a sophisticated analysis method for robust characterization of topological features of a set of data or a function over space. It can be used to characterize the height and spatial extent of topological features like local maxima and minima [139]. This method has typically been used to quantify the typical heights and sizes of the peaks in a test function and separate them from a noise level, but it has not routinely been used to identify isolated clusters. Here we introduce changes to the standard persistent homology method to identify these isolated clusters using features from hierarchical density-based clustering.

First, in order to determine whether two particles belong to the same cluster, we set a distance cutoff of five particle radii, $\zeta = 5\bar{r}$, the same distance used in the computation of the D^2_{min}. If the distance between particles is below this threshold then we consider them to be part of the same cluster. Furthermore, in order to cluster in space and time together, we make replicas at every time step, chosen to be 0.01 natural time units, so that we have good temporal resolution of the deformation. Additionally, we must set a conversion constant, c, between distances in time and distances in space. We choose this conversion such that a separation in time equal to half the Δt used in the D^2_{min} computation is equivalent to cutoff distance ζ or

$$c = \frac{2\zeta}{\Delta t}. \tag{46}$$

The distance between two particles in space-time is given by the usual distance in periodic boundary conditions, $d(\overrightarrow{x}_i, \overrightarrow{x}_j)$, modified by the temporal distance

$$\tilde{d}(i,j) = \sqrt{(}d^2(\overrightarrow{x}_i, \overrightarrow{x}_j) + c^2(t_j - t_i)^2), \tag{47}$$

where $\overrightarrow{x}_i$ and t_i are the position and time of particle i.

Next, we identify a lower-bound value for the cluster volume in space-time, and we will explore larger values later during an optimization procedure. This volume is the sum over the number of particles in each frame of the avalanche. By filtering on the volume, we eliminate small fluctuations near the maxima of the D^2_{min} field over space and time. We specify that when clusters above this size threshold merge they create a new cluster. We identify a region in threshold space where this minimum size does not have a strong effect on the clusters found as it is large enough to clear out noise but small enough to not lose information.

As we perform the persistent homology procedure, we track which events merge to form

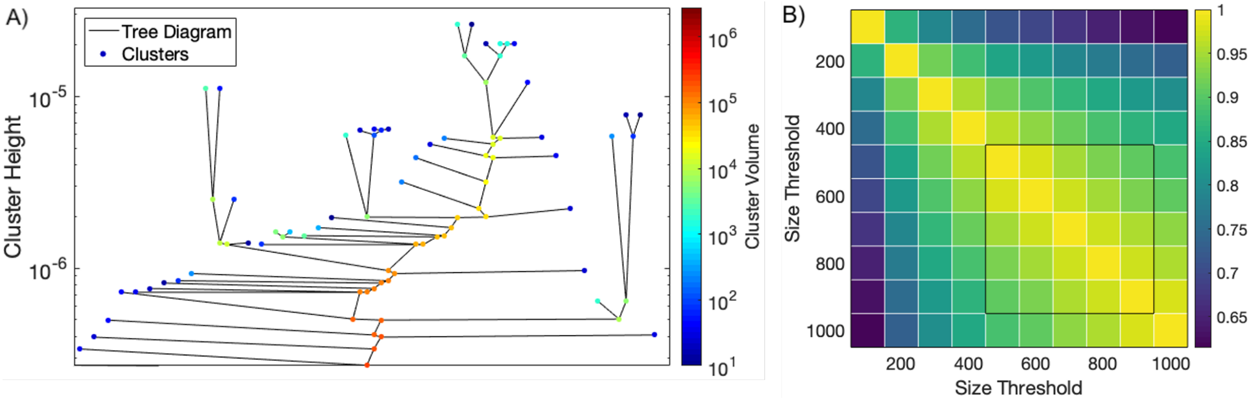

Figure 22: A) A portion of the persistent clustering tree diagram for a single avalanche. The y-coordinate indicates the D^2_{min} value at which the cluster forms. The clusters are colored by their volume. B) The mutual information between the clusters identified at different volume thresholds.

new events to generate a tree diagram. The clusters along a branch in this tree overlap each other in time and space since the merged cluster contains at least every particle in the initial clusters. Therefore, the leaves of this tree diagram do not overlap. We identify the leaves of this tree diagram as the set of isolated clusters. In Fig. 22 A, we show a portion of the tree diagram derived from the persistent clustering algorithm where the clusters are colored according to their volume.

Next, we can use this basic tree diagram to optimize the volume threshold. Specifically, we can define a new threshold on the volume of the clusters and prune this tree diagram to find the equivalent clusters as if we had run the whole analysis again with a new volume threshold. This allows us to rapidly generate and compare the results of different thresholds. In this work, we choose 500 as the value for this threshold as it is the beginning of a plateau where increasing the size has limited changes to the identified clusters. In Fig. 22 B, we show the relative mutual information between the clusters identified at different size thresholds. From a volume threshold 500 to 900, bounded by a black box, there is only a 10% variation in the relative mutual information.

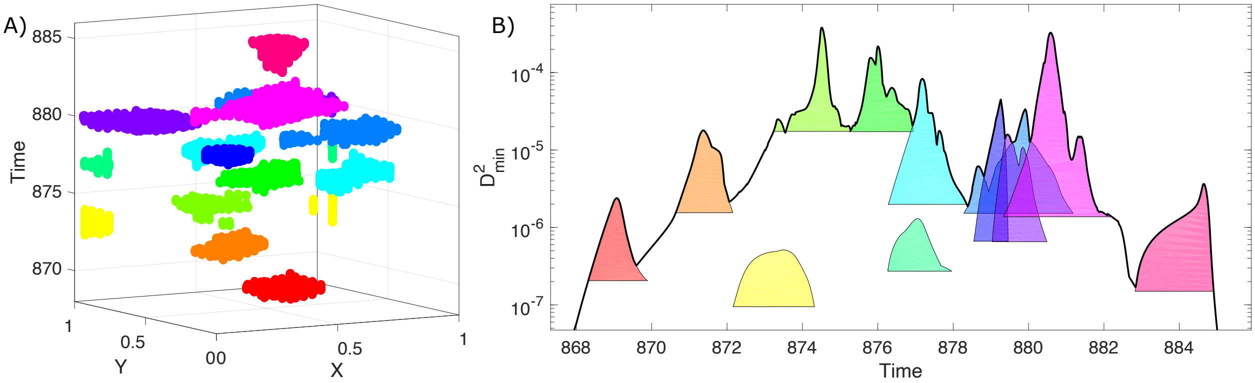

Figure 23: A) The clusters identified by the persistent clustering analysis in one example. B) The plot of the maximum D^2_{min} over time highlighting the D^2_{min} of each cluster in A.

In Fig. 23 A, we show a spacetime plot of the clusters of nonaffine motion, as measured by the D^2_{min}. Not that this system has periodic boundary conditions in the x and y directions. Some of the bursts of localized deformation cross this boundary but are indeed still one single cluster. These clusters meaningfully highlight nonaffine motion in the system during an avalanche. In Fig. 23 B, we show the nonaffine motion occurs in peaks over time, where the black curve shows the $D^2_{min,i}(t)$ maximized over particles, indicating that avalanches occur in bursts of motion. The localized clusters on this nonaffine motion are well separated in time and space and represent the local maxima as seen in Fig. 23 B, where the clusters clearly highlight the peaks in motion over time.

From the beginning of the first burst of localized deformation to the end of the last burst, on average the bursts of localized deformation account for $63 \pm 19\%$ of the nonaffine motion while only accounting for $4 \pm 2\%$ of the spacetime volume. These clusters are localized, typically involving less than 100 particles at any given time. The distribution of the spatial extent of the bursts of localized deformation is shown in Fig. 24 A. This distribution has a

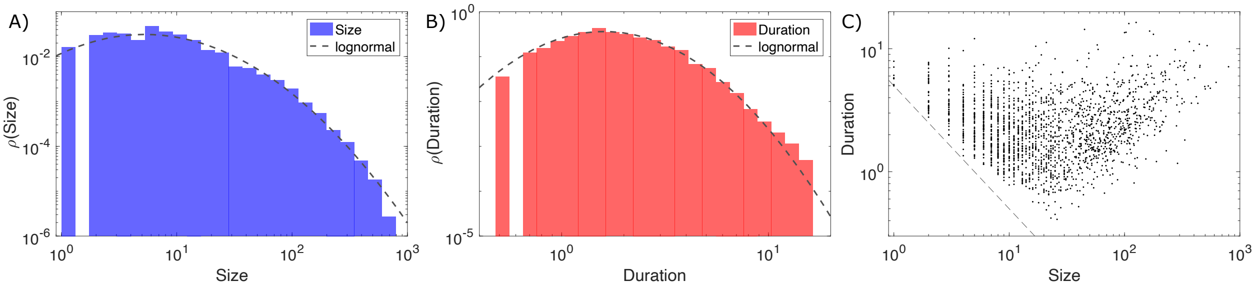

Figure 24: A) The distribution of the size of the identified bursts of localized deformation in 100 avalanches. The dashed line shows a log normal distribution. B) The distribution of the duration of bursts of localized deformation. The dashed line shows a lognormal distribution with the same mean and standard deviation as the duration histogram. C) The relationship between the duration and the size of the burst of localized deformation identified in 100 avalanches. The dashed line shows the threshold for the spacetime volume of the clustering algorithm.

heavy tail such that the majority of the bursts are relatively small, where the median of this distribution shows half of the bursts of localized deformation involve fewer than 61 particles. We have indicated a lognormal distribution to guide the eye and show this size distribution appears to be consistent with a log normal distribution.

Additionally, we investigate the duration of these bursts of localized deformation. In Fig. 24 B, we see that the duration of bursts of localized deformation are distributed around unity with a mean value of 2.7 natural time units. Since the duration has a mean that is comparable to the standard deviation but is required to be positive, we hypothesize the distribution of the duration of bursts of localized deformation follows a log-normal distribution. As can be seen by the dashed line in Fig. 24 B, we plot a log-normal distribution with the same mean and standard deviation and find an excellent consistency. Interestingly, the duration and the size of each burst of localized deformation does not appear to have a strong correlation, as shown in Fig. 24 C. In other words, larger bursts do not seem to take longer to complete than smaller bursts of localized deformation.

4.5 Effective linear response in unstable systems

First, we note that any structural measure which relies on changing the system and measuring the response, like the nonaffine velocity, are not particularly useful in the context of unstable systems because they are infinitely susceptible to perturbation in the unstable directions. Therefore, we focus on the Hessian matrix, an analogue to the dynamical matrix in unstable systems.

To linear order, the equations which govern the deformation of mechanically stable systems are given by the dynamical matrix, M, where the response force, $\overrightarrow{F}$, due to a transformation, $\overrightarrow{u}$, is given by

$$\overrightarrow{F} = M\overrightarrow{u}. \tag{48}$$

Explicitly the entries of the dynamical matrix are defined as the second derivatives of the energy with respect to particle displacements, $\overrightarrow{u}$, relative to a mechanically stable state. If there is no mechanically stable reference state, the dynamical matrix cannot be defined. However, the Hessian matrix, H, whose elements are defined as second derivatives of the energy with respect to particle positions, is always defined. Critically, the Hessian matrix can be defined in unstable systems where the force on at least one particle is nonzero.

To understand the relationship between these objects, it is prudent to inquire about the relationship between derivatives with respect to displacements from a reference state and derivatives with respect to positions. If we consider the derivative of displacing particle i in direction α, we can use the chain rule to find relationship to the positional derivatives in the system

$$\frac{\partial}{\partial u_{i\alpha}} = \frac{\partial}{\partial x_{j\beta}} \times \frac{\partial x_{j\beta}}{\partial u_{i\alpha}} \tag{49}$$

If we now choose an arbitrary reference state whose positions are given by $\overrightarrow{x}_0$, the positions of particles after displacements is given by

$$\overrightarrow{x} = \overrightarrow{x}_0 + \overrightarrow{u} \tag{50}$$

It is clear by construction that $\frac{\partial x_{j\beta}}{\partial u_{i\alpha}} = \delta_{ij}\delta_{\alpha\beta}$. Therefore, derivatives with respect to particle displacements are equivalent to derivatives with respect to particle positions.

$$\frac{\partial}{\partial u_{i\alpha}} = \frac{\partial}{\partial x_{i\alpha}} \tag{51}$$

Thus when the dynamical matrix is defined it is equivalent to the Hessian matrix. This is further illustrated in the Taylor series expansion of the response force due to some transformation, $\overrightarrow{u}$, from a reference configuration:

$$\overrightarrow{F} = \overrightarrow{F_0} - H\overrightarrow{u}. \tag{52}$$

Here $\overrightarrow{F_0}$ is the net force on the system due to interaction between particles, thermal noise, or active forces in the reference configuration. In the special case of mechanical equilibrium, where $\overrightarrow{F_0} = 0$, we recover the behaviour in Eq. 48 where the dynamical matrix is identical to the Hessian. In other words, the total response force is not given by the same equation in stable systems, but the change in force, $\Delta\overrightarrow{F} = \overrightarrow{F} - \overrightarrow{F_0}$, due to some deformation is given by an analogous equation: $\Delta\overrightarrow{F} = H\overrightarrow{u}$.

Therefore, we compute the normal modes of the Hessian in this unstable system to describe features analogous to the vibrational modes in stable systems. Structural measures derived from these modes have had good agreement with localized rearrangements in stable systems [35, 36, 113]. Typically, these structural measures normalize the modes with the inverse of the eigenvalues to highlight the lowest vibrational modes by the relative amount of energy to excite each mode [113]. However, in our unstable system, particularly when close to saddle points in the potential energy landscape, we expect to have negative eigenvalues of the Hessian. If we have negative eigenvalues, the inverse of the eigenvalues does not highlight the lowest energy modes, but only the modes close to zero.

Although we expect to start the minimization with at least one negative eigenmode, it is not required that there be a negative eigenmode throughout the avalanche. In fact, the system cannot reach a stable mechanical equilibrium without first passing through an inflection point such that all negative eigenvalues become positive since, when the system is near a minimum, all of the eigenvalues must be positive. Therefore, at least one eigenvalue must change sign during an avalanche, however it remains unclear how often or to what degree the eigenmodes will change sign.

In addition, since the Hessian is a random matrix, one generally expects there to be avoided eigenvalue crossings and eigenvalue mixing as the strain continuously changes during the avalanche. In practice, however, the low and negative eigenvalues in the spectrum experience very narrowly avoided eigenvalue crossings as a function of strain, and analysis of the eigenvector overlaps suggests that the eigenvectors are not mixing significantly and instead they are essentially switching rank. An interesting open question is how frequently these rank switching events occur for the lowest (most negative) eigenvalues, and how those switching events impact the system dynamics.

If the eigenmodes do not switch rank very often, we can predict the motion of the system using the unstable force and the eigenmodes of the Hessian. Since in the overdamped limit of our simulation the velocity is given by the force, we can find how the system evolves by taking a time derivative of the force,

$$\frac{d\overrightarrow{F}}{dt} = -H\overrightarrow{F}. \tag{53}$$

In the eigenbasis, we find the force or the velocity along each eigenmode is described by

$$\frac{dF_i}{dt} = -\lambda_i F_i, \tag{54}$$

where λ_i is the eigenvalue of the i^{th} mode. The solutions to this simple differential equation are exponential decays for positive eigenvalues and exponential growth for negative eigenvalues. Note that there is no oscillation. Since we use an inertia-free simulation, information does not propagate through the system via phonon modes, but rather deformation diffuses throughout the system. Since the lowest modes either decay the slowest or grow exponentially over time, ultimately the force is dominated by the lowest mode independent of whether the system is stable or unstable. Perhaps the simplest hypothesis for the avalanche dynamics is that each of the localized rearrangements follow the single lowest vibrational mode, and then changes in the structure caused by the rearrangement identify a new lowest eigenmode and the next localized rearrangement follows this new unstable mode. Below, we will show how and why this hypothesis fails in avalanches we observe in our simulations.

4.6 The lowest "vibrational" modes change rapidly throughout minimization

In our unstable system, we investigate the dynamic behavior of the eigenvalues of the Hessian during deformation in order to probe the curvature of the energy landscape along the minimization path. If the potential energy landscape was simple we would expect a single negative eigenvalue that becomes positive as the system approaches the energetic minimum. In fig. 25 A, we show the lowest ten eigenvalues over the course of an avalanche. Initially, there is only one negative eigenvalue before the main rearrangements occur and, after the rearrangements, all eigenvalues are positive as the system approaches the minimum, as expected. However, during the rearrangements, the eigenvalues change very dramatically–on the scale of an order of magnitude–in sudden jumps often to become more negative. Surprisingly, unlike in a simple picture of a single inflection point, many eigenvalues can become negative between the initial configuration, near a saddle point, and the final configuration at a local minimum in the energy landscape. As can be seen in Fig. 25 B, here can be as many as 5 or 6 negative eigenvalues as the system rearranges. This is indicative of the system passing nearby many saddle points or higher order saddle points during deformation, although our data do not distinguish between these two cases.

Contradicting the simplest hypothesis outlined above, we find that the lowest eigenmode changes significantly multiple times in each burst of localized deformation. In Fig 26 A and E, we show the dot product of the lowest eigenmode at time t with the lowest eigenmode at time $t + \delta t$, where δt is 0.01 time units, during two separate bursts of localized deformation. This measure is nearly 1 if there has been little change in the direction of the lowest mode

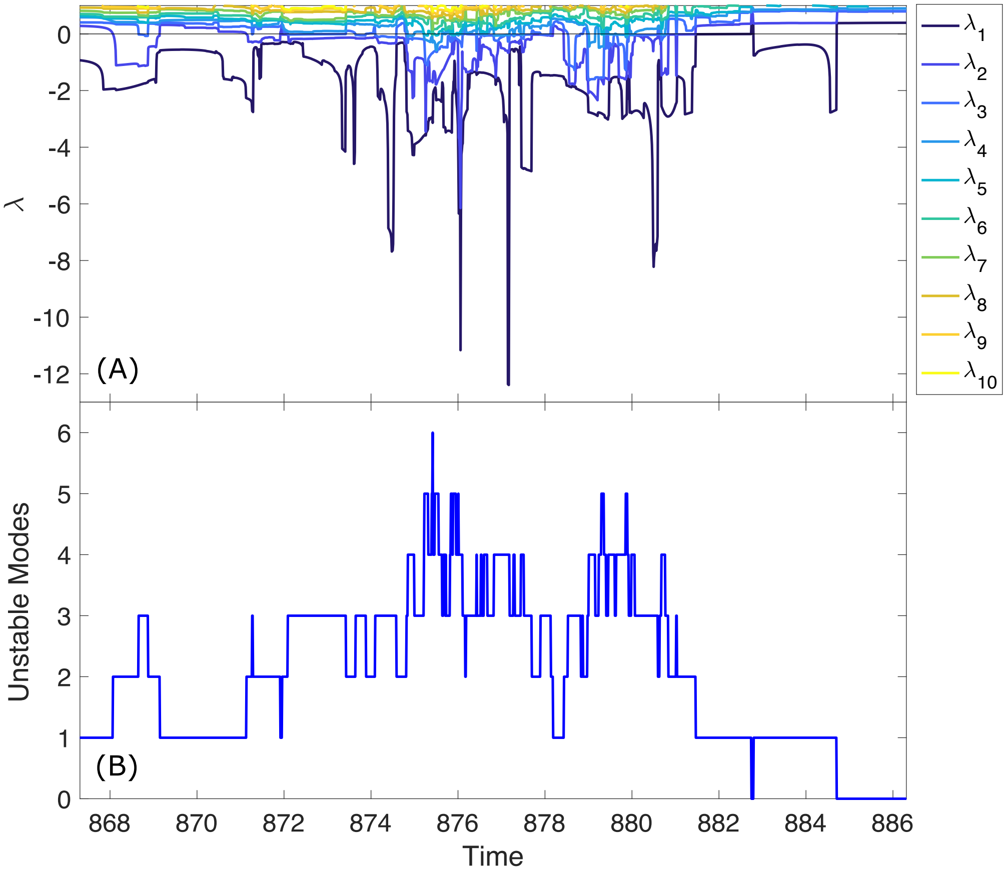

Figure 25: A) The lowest 10 eigenvalues of the Hessian as a function of time for a single avalanche simulation. B) The number of eigenvalues below zero as a function of time.

in this high-dimensional phase space. On the other hand, this measure will be smaller than 1 if there is a sudden change in the lowest mode, such as a change to which particles are most engaged in the mode or the directions in which the particles are engaged. The burst of localized deformation highlighted in Fig 26 A-D has few, relatively small changes to the lowest eigenmode as shown in Fig 26 A. This short burst of localized deformation is well-isolated in time from other deformations such that no other bursts occur simultaneously. On the other hand, the burst of localized deformation in Fig 26 E-H is much longer and occurs simultaneously in time with bursts in other locations. This burst of localized deformation is concurrent with many substantial changes to the lowest eigenmode, to the point where the lowest eigenmode can become nearly orthogonal to itself a short time later, on timescales much shorter than the duration of the bursts of localized deformation, as shown in Fig 26 E. These sudden changes are caused by motions that rapidly alter the Hessian, ie. motions not well captured by linear response. Most of these peaks of these large changes coincide with topological changes to the system such as contact changes, buckling in the contact network, and even T1 transitions in the Voronoi diagram.

However, despite these sudden changes in the eigenmode structure, the force, or velocity, does not change rapidly with these mode-switching events. If the burst of interest begins at time t_0, Fig 26 B and F show the evolution of the force in the direction of the lowest eigenmode at the beginning of the bursts of localized deformation, $|\hat{F}(t) \cdot \hat{v}_1(t_0)|$. As we only measure the unit force, this quantity is unity when the force is completely in the direction of the initial lowest eigenmode and near zero if the force is orthogonal to the initial lowest eigenmode. In both these bursts of localized deformation, the force is well aligned with the lowest eigenmode. Furthermore, the force near the beginning of the burst of localized deformation turns to become better aligned. The force in the well isolated burst of localized deformation shown in Fig. 26 B becomes almost perfectly aligned with the lowest eigenmode at the beginning of the burst of localized deformation. However, after the sudden changes to the eigenmodes, the force turns away from the initial lowest eigenmode. There is not a sudden change to the force in the initial lowest eigenmode or the slope, rather the turn is exponential as the force decays to the new lowest eigenmode. Note that the force in Fig. 26 B doesn't have far to turn since the lowest eigenmode changes relatively little. This turning effect is somewhat more pronounced in the green burst of localized deformation in Fig. 26 F which takes place over a longer timescale and involves much more substantial changes to the direction of lowest eigenmode. In this burst of localized deformation, the force becomes nearly orthogonal to the initial lowest eigenmode.

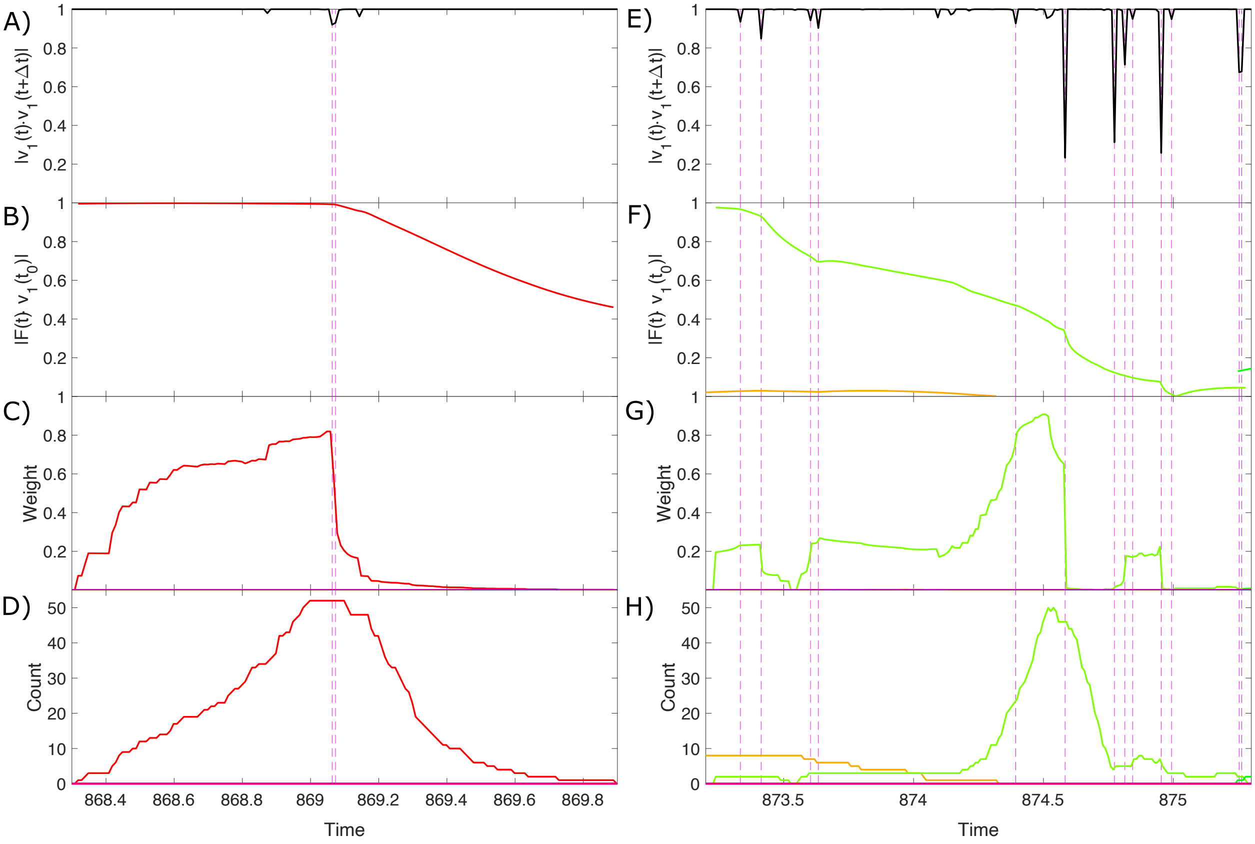

Figure 26: **A-D) Evolution of the eigenmode with the most negative eigenvalue in a simple event** A) The dot product of the lowest eigenmode at time t with the lowest eigenmode at time $t + \delta t$. The verticle pink lines indicate times when the lowest eigenmode has changed significantly, specifically when $|\hat{v}_1(t) \cdot \hat{v}_1(t+\delta t)| < 0.95$ for $\delta t = 0.01$. B) The dot product of the normalized force vector at time t with the eigenmode at the beginning of the burst of localized deformation, t_0. C) The weight of the lowest eigenmode in the deformation region. D) The number of particles in the deformation region as a function of time.
E-H Evolution of the eigenmode with the most negative eigenvalue in a complex event Parts E), F), G), and H) show the instantaneous change in the eigenmode, the force in the initial lowest eigenmode, and the weight and number of particles for another two bursts of localized deformation occurring simultaneously where the green curves indicate the burst of localized deformation we focus the time window on and the orange curves refer to another burst of localized deformation.

In Fig. 26 C we investigate the weight of the lowest eigenmode in the burst, defined by

$$W_I = \sum_{i \in B_I} \sum_{\alpha} v_{1,i\alpha}^2 \tag{55}$$

where B_I is burst of localized deformation I and v_1 is the lowest eigenmode of the Hessian. At the point where there is a sudden change in the lowest eigenmode, indicated by the dashed lines, there is a sudden shift in the weight of the lowest vibrational mode in this burst of localized deformation. However, in Fig. 26 D, we show the number of particles in the burst of localized deformation does not change instantaneously at that point. This suggests that lowest eigenmode was localized to the burst location, but, after structural changes during the deformation, the lowest vibrational mode moves out of the burst location. After this sudden change to lowest vibrational mode, the size of the burst of localized deformation begins to decay slowly. This behavior is reflected again in the burst of localized deformation focused on in Fig. 26 G, where the weight of the lowest vibrational mode in the burst location changes suddenly when there is a large sudden change to the vibrational mode. Again, the size of the burst does not change instantaneously Fig. 26 H. One distinction of this burst from the burst shown in Fig. 26 C is that the lowest vibrational mode jumps in and out of the burst location at the sudden changes to the lowest vibrational mode.

Other bursts of localized deformation have little to no interaction with the lowest eigenmode, but are potentially driven by other modes since we know that there are multiple unstable modes while the system is rearranging. For instance, the orange curve in Fig. 26 H indicates the size of another burst of localized deformation, but the weight of the lowest eigenmode in this burst of localized deformation is significantly lower than in other bursts maximizing at a value of 0.01. This value is too small to show by an orange curve in Fig. 26 G on the scale necessary to view the red and green curves in Fig. 26 C and G respectively.

4.7 Soft spots evolve during avalanches

As there are many changes the lowest eigenmode and the other modes, rather than measuring the overlap with each mode individually, we compute a softness field over space and time as a linear sum of the nonaffine part of the lowest eight modes. Here the nonaffinity of a mode is computed using the D^2_{min} algorithm on each eigenvector as if it were a displacement field, with the same lengthscale used to quantify deformation, five average particle radii.

We have chosen to use the eight lowest modes in order to ensure that all the unstable eigenmodes of a system are included in the structural measure. Furthermore, we have investigated how many of the lowest vibrational modes contribute significantly to other structural metrics. In particular, we focus on the vibrability, or thermal susceptibility of motion, measured just before the rearrangement. We find the total vibrability of the system is well-approximated by summing over a very small number of modes. Specifically, the vibrability summed over only the lowest eight modes approximates the true vibrability to within 98%. This measure is expected to capture important features of the eigenmodes while being less sensitive to structural changes than one eigenmode alone. We expect the number of modes needed to capture the salient features of the structure to increase linearly with system size.

Having chosen a softness field, we identify the soft spots in spacetime with the same persistent clustering algorithm used to compute the bursts of localized deformation. We choose a size threshold of 1000 to optimize correlation with the bursts of localized deformation

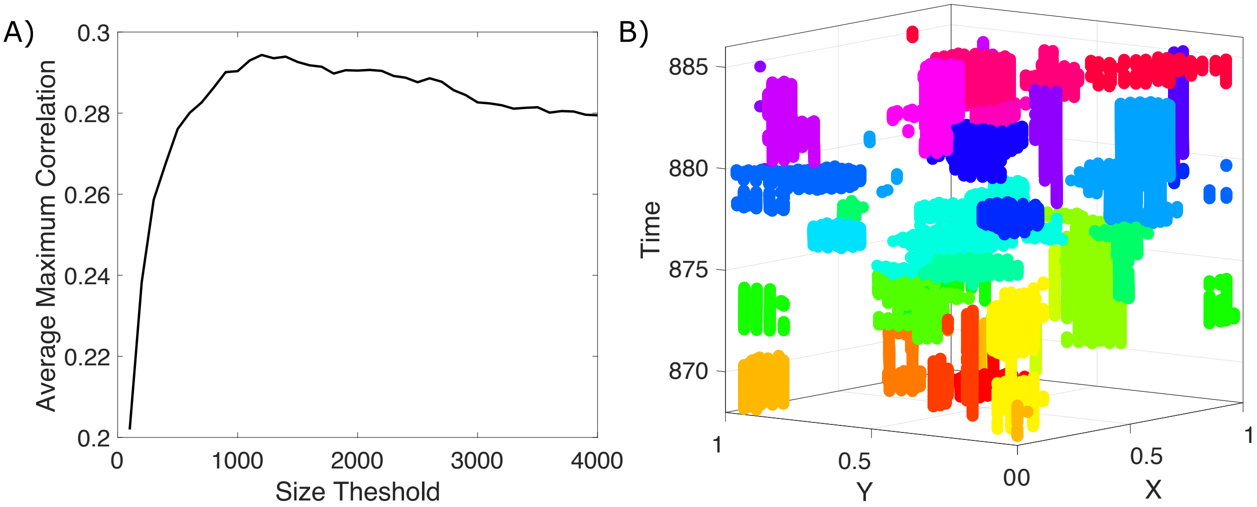

Figure 27: A) The average maximum correlation for each burst of localized deformation as a function of the volume threshold. B) A spacetime plot highlighting the localized soft spots found by clustering on the softness field over time for a volume threshold of 1000. Note the x- and y-directions in this system have periodic boundary conditions.

found previously, as shown by the maximum in Fig. 27 A, where we plot the average of the maximum correlation of soft spots with each burst of localized deformation. The space- and time-locations of these soft spots are shown in Fig. 27 B. These soft spots are much smaller in space than the bursts of localized deformation, with the largest soft spot on the order of 30 particles. Although the lowest eigenmodes change significantly on the order of 100 times across 12 localized bursts in this example, we measure only 25 unique soft spots, many of which exist simultaneously.

It is important to note that the soft spots, while localized in space, are mostly columnar in time, indicating there is relatively little change to the soft spot over time. Therefore, they are more stable in time than the lowest eigenmode, as they change comparatively few times in across the avalanche. This is also a radically different time profile than the bursts of localized deformation in the strain field such as those in Fig. 24 A.

One issue with the current method for clustering soft spots is disconnection over time.

Many times a soft spot will occur in the same place as another soft spot separated by small amount of time, indicating that these two soft spots are likely the same soft spot, but our persistent clustering method has separated them. However, applying larger size thresholds on the volume of the clusters often results in joining many soft spots together. Furthermore, there is a large variation in timescales of the soft spots with many long-lived soft spots existing simultaneously with a number of very short-lived soft spots. Increasing the thresholds will result in the removal of some number short-lived soft spots which have good correlation with bursts of localized deformation.

We have attempted multiple methods for correcting this error. For instance, we have developed a second clustering algorithm inspired by watershed image processing, which prunes clusters not by their space-time volume but rather by the persistence of the individual peaks. Further, we are investigating modifications to the filtration of the persistence tree to prune leaves with a threshold on features like the persistence of clusters rather than the volume alone. We are also currently testing using larger time windows for the clustering of the softness field rather than using the the same time windows as we used in the clustering of the D^2_{min}, which also may address this problem.

4.8 Dynamic soft spots correlate with bursts of localized deformation

The clustering analysis allows us to define the bursts of localized deformation and soft spots as discrete scalar fields. The mutual information between these fields is useful for determining how well one predicts the other [140]. Specifically, we use a normalized form of the mutual information called the proficiency, which measures how well each soft spot predicts the spatiotemporal location of each burst of localized deformation and is given by

$$\mathcal{P}_{IJ} = \frac{M(I,J)}{H(I)}, \tag{56}$$

where $M(I,J)$ is the mutual information between soft spot J and burst of localized deformation I and $H(I)$ is the information measure of the burst of localized deformation I.

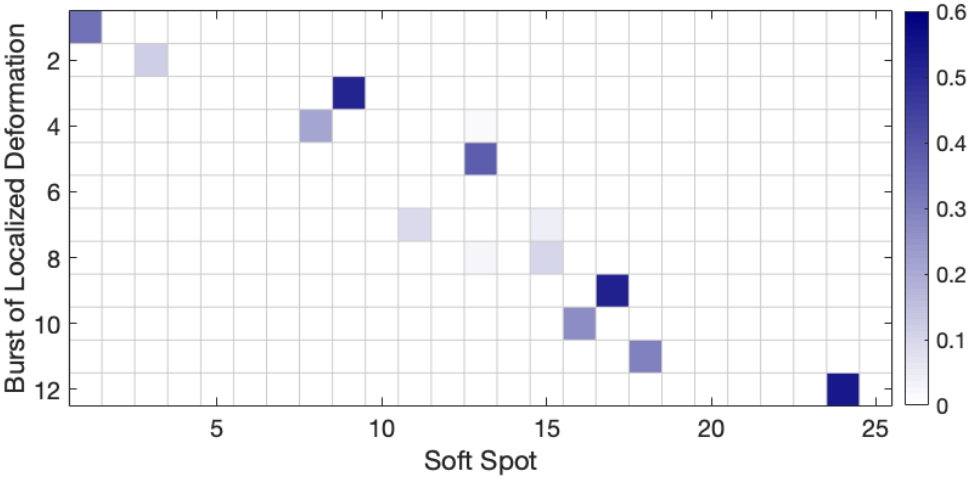

Figure 28: Proficiency between each soft spot with each burst of localized deformation in a single avalanche.

The mutual information between two discrete fields is computed with

$$M(I,J) = \sum_{x\in[I,\tilde{I}]} \sum_{y\in[J,\tilde{J}]} p_{x,y} \log_2 \left(\frac{p_{x,y}}{p_x p_y} \right), \tag{57}$$

where x is the discrete field of the burst of localized deformation, y is the discrete field of soft spots, and p_x, p_y and $p_{x,y}$ are the probabilities that an arbitrary point in the discrete fields is x in the discrete field formed from the bursts of localized deformation, or y in the soft spot field, or both, respectively. The information $H(I)$ is given by the mutual information with itself:

$$H(I) = M(I, I). \tag{58}$$

The proficiency is near unity when the spatial location of a soft spot overlaps very well with the spatial location of a burst of localized deformation and occurs at the same time. If the proficiency is very near zero, then the soft spot and the burst of localized deformation have little to no overlap in space and time.

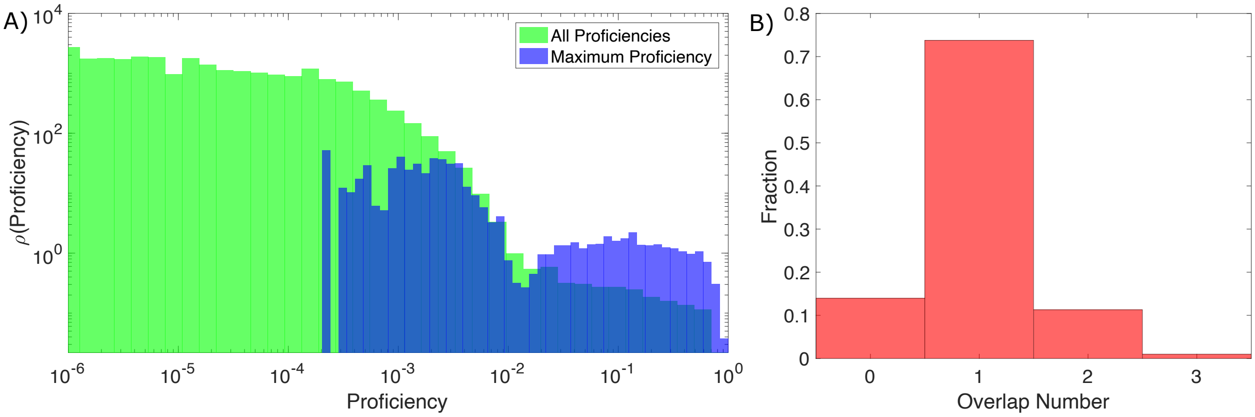

Figure 29: A) Statistics of proficiency across many avalanches for all bursts of localized deformation and soft spot (green) and the maximum proficiency for each burst of localized deformation (blue). B) The statistics of the number of soft spots with proficiency above 0.01 for each burst of localized deformation.

The soft spots identified by the persistent clustering analysis have strong correlations with the space time locations of the bursts of localized deformation. In Fig. 28, we show the proficiency between each burst of localized deformation and each soft spot. In this example, all but one burst of localized deformation have good correlation with at least one soft spot. This indicates that the structure probed by the soft spots is indeed probing some features relevant to the plastic motion. We further investigate the statistics of the proficiencies between soft spots and bursts of localized deformation shown in Fig. 29 A. There is a clear drop off in the proficiency of all soft spots with all bursts of localized deformation at about

$\mathcal{P}_{IJ} = 0.01$. This suggests that, as expected, most soft spots do not overlap with a plastic event at a given instant in time, and that values of $\mathcal{P}_{IJ}$ below 0.01 correspond to no overlap. In contrast, the maximum proficiency for each burst of localized deformation exhibits a clear peak beyond $\mathcal{P}_{IJ} = 0.01$, and so if a soft spot and burst of localized deformation have a proficiency greater than 0.01, we define these as being overlapped. In Fig. 29 B, we show statistics of how many soft spots overlap with each burst of localized deformation. We find that 74% of the bursts of localized deformation overlap with one soft spot, while only 14% of all bursts of localized deformation have no overlap with any soft spot. Taken together, these data suggest that bursts of localized deformation occur when a structural defect, or soft spot, reaches its yield stress and deforms. Moreover, we can now track the evolution of such defects during an avalanche.

4.9 Discussion

Under the application of stress, many disordered materials undergo large scale structural transformations or avalanches. Currently, structural indicators for the locations of deformation in amorphous systems are excellent at predicting small isolated rearrangements [113]. However, these methods cannot predict the full motion in an avalanche. Furthermore, the available tools have only been developed for analysis of mechanically stable states using perturbative expansions or involve transformation and minimization. An improved understanding of the structural evolution of avalanching disordered materials as well as extended methods for measuring softness of unstable systems are critical to improve prediction methods or develop novel prediction methods.

In this manuscript, we followed the deformation of avalanches in overdamped athermal disordered systems under applied shear to identify the patterns structural evolution through out the avalanche. We find that the plastic motion in avalanches occurs in bursts over time and, using a novel clustering algorithm, we robustly identify the bursts of localized deformation. This is consistent with phenomenological work of elastoplastic models which explicitly predict avalanches to be a sequence of localized rearrangements.

Using the normal modes of the Hessian, we probe the curvature of the unstable system. Our first major observation is that there are multiple negative eigenmodes that change rapidly with small subtle changes to the underlying structure. Localized soft spots generated from this eigenspectrum are more stable, and we find these localized soft spots have good correlation with the bursts of localized deformation. An obvious next step is to study how these localized soft spots couple to one another – via an elastic kernel, structural diffusion, or perhaps a combination. Such data will constrain and improve continuum models for plastic failure.

This study has been limited to two-dimensional packings generated via infinite temperature quench. Packings formed in this way have relatively low energy barriers to rearrangement compared to well annealed systems. The preparation protocol is expected to strongly impact the details of the rearrangement and the evolution of the avalanche. However, it is expected that these rearrangements and avalanches will qualitatively decompose into bursts of localized motion in the same way.

Although these methods have been applied to relaxing athermal disordered systems, other unstable systems could also benefit from similar analyses. For instance, studies of the structural evolution of thermal systems have focused on the inherent, or energy minimized, states or on free-energy minimized configurations. Similarly, active systems, like crowds of human people or dense packings of driven colloidal particles have relied on structural evaluations of mechanically stable reference states. However, instantaneous evaluation of the structure of these mechanically unstable systems have previously been unavailable. Moving forward it will be interesting to extend the methods developed here to other unstable or active systems.

5 Future directions

In Chapter 2, we analyzed a sparse random matrices where disorder is controlled by the distribution of bond weights and network coordination. We find a unique ω^3 low frequency regime and recapitulate an ω^4 region, as seen in simulated models of glasses. The salient features of the networks that mimic the density of states in glassy systems are that 1) the system is close to isostaticity, and 2) the probability density of bond weights near zero is finite. However, this work was limited to a one-dimensional model which could have pathological results. For instance, the ω^3 regime in the density of states is reliant on the segmentation of the system at the two weakest bonds.

However, in a higher-dimensional system, such segmentation requires the participation of a number of bonds proportional to the surface area of the segmented region. This implies that the ω^3 regime is a feature of the one-dimensional model alone. One avenue of research open for investigation is finding similar random matrix models representative of higher-dimensional glassy systems. In such systems, we would not only have to consider the network coordination and scalar bond weights, but also bond orientation. The relative orientations of bonds could result in effective bond weights near zero without the scalar bond weights approaching zero relative to some transformation. Investigations into such behavior could be extremely enlightening towards the behavior of elastic networks and glassy systems in which the scalar bond weights are finite.

In Chapter 3, we investigated the structure and behavior of a unique, symmetry-broken self-propelled particle system. We are currently investigating the effects of pressure gradients in amorphous systems especially how the structure rearranges. Through modification of the dynamical matrix used to evaluate linear response measures with a simple external potential,we also found these packings demonstrate strong radial gradients in structural measures of softness such as in the vibrability and nonaffine vibrability. In addition to applying these methods to the study of human crowd behavior, this is representative of a larger class of systems in which we can investigate the amorphous structure. Specifically, for any system which can be modeled as affected by an external potential, we can extend structural analysis methods for static packings in the absence of an external potential to investigate the regions that are likely to rearrange with the application of additional external force or thermal excitation. For instance, these methods could prove useful in systems such as grain in silos to investigate the jamming to unjamming transition as grain flows.

In Chapter 4, we demonstrated that avalanches of large-scale plastic deformation in athermal, amorphous systems of soft spheres are decomposable into bursts of localized deformation, a result which is consistent with predictions from elastoplastic models. One obvious path forward, now that we have identified the locations of the bursts of localized deformation, is to identify the methods by which these bursts communicate with one another. For instance, can we track the elastic propagation of structural changes from the location of one burst of localized deformation to find how one burst explicitly triggers other bursts of localized deformation? Is it consistent with propagation via an elastic kernel as predicted by elastoplastic models or does structural disorder propagate via local structural diffusion as proposed by STZ models or something else entirely?

Additionally, the clustering algorithm discussed in Chapter 4 has applications beyond the clustering of motion and softness in athermal avalanches. Specifically, we are working with collaborators to evaluate collective cell migration in epithelial tissue. We are also interested in evaluating the melting behavior in thermal systems, where the Hessian is also not positive definite and preparation protocol can dictate the evolution of the phase transition. Amorphous materials formed via vapor deposition, or the slow addition of material, melt from the surface towards the center. On the other hand, glasses formed by annealing or the novel swap methods, melt via droplet formation. The new persistent clustering algorithm we propose could be helpful for identification of bursts of motion during the melting phase and investigation of flow in the liquid phase.

Finally, we have extended methods for measuring softness to systems that need not necessarily be mechanically stable. In conjunction with the extensions we discuss in Chapter 3, we have developed tools for investigating the structure of unstable systems in the presence of external fields. These methods allow for the structural evaluation of many kinds of systems which previously required investigation relative to a stable reference state or inherent state. In other words, from a snapshot of a system, these tools can evaluate the regions that are likely to experience plastic deformation without relying on reference states which could prove helpful in predicting the mechanical response in thermal, active, or driven systems.

References

1. Degryse, P. *Glass Making in the Greco-Roman World: Results of the ARCHGLASS project* ISBN: 9789462700079. `https://books.google.com/books?id=I194BgAAQBAJ` (Leuven University Press, 2015).
2. Asimov, I. *The History of Physics* ISBN: 9780802707512. `https://books.google.com/books?id=PdpzQgAACAAJ` (Walker, 1984).
3. Zanotto, E. D. Do cathedral glasses flow? *American Journal of Physics* **66,** 392–395 (1998).
4. Debenedetti, P. G. & Stillinger, F. H. Supercooled liquids and the glass transition. *Nature* **410,** 259–267. `https://doi.org/10.1038/35065704` (Mar. 2001).
5. Warren, B. E. & Biscce, J. The structure of silica glass by x-ray diffraction studies. *Journal of the American Ceramic Society* **21,** 49–54 (1938).
6. Zachariasen, W. H. The atomic arrangement in glass. *Journal of the American Chemical Society* **54,** 3841–3851 (1932).
7. Ritland, H. N. Density phenomena in the transformation range of a borosilicate crown glass. *Journal of the American Ceramic Society* **37,** 370–377 (1954).
8. Mizuno, Y., Kofu, M. & Yamamuro, O. X-ray Diffraction Study on Simple Molecular Glasses Created by Low-Temperature Vapor Deposition. *Journal of the Physical Society of Japan* **85,** 124602. `https://doi.org/10.7566/jpsj.85.124602` (Dec. 2016).
9. Warren, B. E. *X-ray Diffraction* (Courier Corporation, 1969).

10. Bernal, J. D. A Geometrical Approach to the Structure Of Liquids. *Nature* **183,** 141–147. `http://dx.doi.org/10.1038/183141a0` (Jan. 1959).
11. Warren, B. X-ray Diffraction Study of the Structure of Glass. *Chemical Reviews* **26,** 237–255 (1940).
12. Uhlmann, D. & Kreidl, N. *Elasticity and Strength in Glasses* ISBN: 9780127067056. `https://books.google.com/books?id=7useAQAAIAAJ` (Academic Press, 1980).
13. Kardar, M. *Statistical Physics of Fields* ISBN: 9781139855884. `https://books.google.com/books?id=%5C_XQgAwAAQBAJ` (Cambridge University Press, 2007).
14. Debenedetti, P. G., Truskett, T. M., Lewis, C. P. & Stillinger, F. H. Theory of supercooled liquids and glasses: Energy landscape and statistical geometry perspectives (2001).
15. Parisi, G. & Sciortino, F. Flying to the bottom. *Nature Materials* **12,** 94–95. `https://doi.org/10.1038/nmat3540` (Jan. 2013).
16. Van Hecke, M. Jamming of soft particles: geometry, mechanics, scaling and isostaticity. *Journal of Physics: Condensed Matter* **22,** 033101 (2009).
17. O'Hern, C. S., Silbert, L. E., Liu, A. J. & Nagel, S. R. Jamming at zero temperature and zero applied stress: The epitome of disorder. *Physical Review E* **68.** `https://doi.org/10.1103/physreve.68.011306` (July 2003).
18. Haxton, T. K., Schmiedeberg, M. & Liu, A. J. Universal jamming phase diagram in the hard-sphere limit. *Phys. Rev. E* **83,** 031503. `https://link.aps.org/doi/10.1103/PhysRevE.83.031503` (3 Mar. 2011).

19. Bi, D., Yang, X., Marchetti, M. C. & Manning, M. L. Motility-driven glass and jamming transitions in biological tissues. *Physical Review X* **6,** 021011 (2016).

20. Wang, W.-H., Dong, C. & Shek, C. Bulk metallic glasses. *Materials Science and Engineering: R: Reports* **44,** 45–89 (2004).

21. Merkel, M. & Manning, M. L. A rigidity transition and glassy dynamics in a model for confluent 3D tissues. *Bulletin of the American Physical Society* **62** (2017).

22. Bottinelli, A., Sumpter, D. T. & Silverberg, J. L. Emergent structural mechanisms for high-density collective motion inspired by human crowds. *Physical review letters* **117,** 228301 (2016).

23. Telford, M. The case for bulk metallic glass. *Materials today* **7,** 36–43 (2004).

24. Pudasaini, S. P. & Hutter, K. *Avalanche dynamics: dynamics of rapid flows of dense granular avalanches* (Springer Science & Business Media, 2007).

25. Sollich, P. in *Molecular Gels* 161–192 (Springer, 2006).

26. Falk, M. & Langer, J. Dynamics of viscoplastic deformation in amorphous solids. *Physical Review E* **57,** 7192 (1998).

27. Manning, M. L., Langer, J. S. & Carlson, J. M. Strain localization in a shear transformation zone model for amorphous solids. *Physical Review E* **76.** `https://doi.org/10.1103/physreve.76.056106` (Nov. 2007).

28. Falk, M. L., Toiya, M. & Losert, W. *Shear transformation zone analysis of shear reversal during granular flow* 2008. eprint: `arXiv:0802.1752`.

29. Ozawa, M., Berthier, L., Biroli, G., Rosso, A. & Tarjus, G. Random critical point separates brittle and ductile yielding transitions in amorphous materials. *Proceedings of the National Academy of Sciences* **115,** 6656–6661 (2018).

30. Popović, M., de Geus, T. W. & Wyart, M. Elastoplastic description of sudden failure in athermal amorphous materials during quasistatic loading. *Physical Review E* **98,** 040901 (2018).

31. Freeman, J. & Anderson, A. Thermal conductivity of amorphous solids. *Physical Review B* **34,** 5684 (1986).

32. Ashcroft, N. & Mermin, N. *Solid State Physics* ISBN: 9780030839931. `https://books.google.com/books?id=1C9HAQAAIAAJ` (Holt, Rinehart and Winston, 1976).

33. Gal'perin, Y. M., Karpov, V. & Solov'ev, V. Density of vibrational states in glasses. *Zh. Eksp. Teor. Fiz* **94,** 384 (1988).

34. Anderson, A. C. *et al. Amorphous solids: low-temperature properties* (Springer Science & Business Media, 2012).

35. Wijtmans, S. & Manning, M. L. Disentangling defects and sound modes in disordered solids. *arXiv preprint arXiv:1502.00685* (2015).

36. Manning, M. L. & Liu, A. J. Vibrational modes identify soft spots in a sheared disordered packing. *Physical Review Letters* **107,** 108302 (2011).

37. Rottler, J., Schoenholz, S. S. & Liu, A. J. Predicting plasticity with soft vibrational modes: From dislocations to glasses. *Physical Review E* **89,** 042304 (2014).

38. Charbonneau, P., Corwin, E. I., Parisi, G., Poncet, A. & Zamponi, F. Universal non-Debye scaling in the density of states of amorphous solids. *Physical Review Letters* **117,** 045503 (2016).

39. Lerner, E., Düring, G. & Bouchbinder, E. Statistics and properties of low-frequency vibrational modes in structural glasses. *Physical Review Letters* **117,** 035501 (2016).

40. Franz, S., Parisi, G., Urbani, P. & Zamponi, F. Universal spectrum of normal modes in low-temperature glasses. *Proceedings of the National Academy of Sciences* **112,** 14539–14544 (2015).

41. Buchenau, U., Galperin, Y. M., Gurevich, V. L. & Schober, H. R. Anharmonic potentials and vibrational localization in glasses. *Physical Review B* **43,** 5039–5045. `https://doi.org/10.1103/physrevb.43.5039` (Feb. 1991).

42. Parshin, D. Soft potential model and universal properties of glasses. *Physica Scripta* **1993,** 180 (1993).

43. Gurevich, V., Parshin, D. & Schober, H. Anharmonicity, vibrational instability, and the Boson peak in glasses. *Physical Review B* **67,** 094203 (2003).

44. Wyart, M., Nagel, S. R. & Witten, T. Geometric origin of excess low-frequency vibrational modes in weakly connected amorphous solids. *EPL (Europhysics Letters)* **72,** 486 (2005).

45. Goodrich, C. P., Liu, A. J. & Nagel, S. R. Finite-size scaling at the jamming transition. *Physical review letters* **109,** 095704 (2012).

46. Zeravcic, Z., van Saarloos, W. & Nelson, D. R. Localization behavior of vibrational modes in granular packings. *EPL (Europhysics Letters)* **83,** 44001 (2008).

47. Manning, M. L. & Liu, A. J. A random matrix definition of the boson peak. *EPL (Europhysics Letters)* **109,** 36002 (2015).

48. Parisi, G. & Zamponi, F. Mean-field theory of hard sphere glasses and jamming. *Reviews of Modern Physics* **82,** 789 (2010).

49. Rainone, C., Urbani, P., Yoshino, H. & Zamponi, F. Following the evolution of hard sphere glasses in infinite dimensions under external perturbations: compression and shear strain. *Physical review letters* **114,** 015701 (2015).

50. Torquato, S. & Stillinger, F. H. Jammed hard-particle packings: From Kepler to Bernal and beyond. *Reviews of modern physics* **82,** 2633 (2010).

51. Singh, S., Ediger, M. D. & de Pablo, J. J. Ultrastable glasses from in silico vapour deposition. *Nature Materials* **12,** 139–144. `https://doi.org/10.1038/nmat3521` (Jan. 2013).

52. Ninarello, A., Berthier, L. & Coslovich, D. Models and Algorithms for the Next Generation of Glass Transition Studies. *Physical Review X* **7.** `https://doi.org/10.1103/physrevx.7.021039` (June 2017).

53. Kapteijns, G., Ji, W., Brito, C., Wyart, M. & Lerner, E. Fast generation of ultrastable computer glasses by minimization of an augmented potential energy. *Physical Review E* **99,** 012106 (2019).

54. Spaepen, F. *Structural Imperfections in Amorphous Metals.* tech. rep. (HARVARD UNIV CAMBRIDGE MA DIV OF APPLIED SCIENCES, 1978).

55. Patinet, S., Vandembroucq, D. & Falk, M. L. Connecting Local Yield Stresses with Plastic Activity in Amorphous Solids. *Physical Review Letters* **117.** `https://doi.org/10.1103/physrevlett.117.045501` (July 2016).

56. Liao, Q. & Xu, N. Criticality of the zero-temperature jamming transition probed by self-propelled particles. en. *Soft Matter* **14,** 853–860. ISSN: 1744-6848. `http://pubs.rsc.org/en/content/articlelanding/2018/sm/c7sm01909b` (2018) (Jan. 2018).

57. Henkes, S., Fily, Y. & Marchetti, M. C. Active Jamming: Self-propelled soft particles at high density. *Physical Review E* **84.** arXiv: 1107.4072. ISSN: 1539-3755, 1550-2376. `http://arxiv.org/abs/1107.4072` (2018) (Oct. 2011).

58. Fily, Y., Henkes, S. & Marchetti, M. C. Freezing and phase separation of self-propelled disks. *Soft Matter* **10.** arXiv: 1309.3714, 2132–2140. ISSN: 1744-683X, 1744-6848. `http://arxiv.org/abs/1309.3714` (2018) (2014).

59. Agoritsas, E., Biroli, G., Urbani, P. & Zamponi, F. Out-of-equilibrium dynamical mean-field equations for the perceptron model. en. *Journal of Physics A: Mathematical and Theoretical* **51,** 085002. ISSN: 1751-8121. `http://stacks.iop.org/1751-8121/51/i=8/a=085002` (2018) (2018).

60. Agoritsas, E., Maimbourg, T. & Zamponi, F. Out-of-equilibrium dynamical equations of infinite-dimensional particle systems. II. The anisotropic case under shear strain. en. *Journal of Physics A: Mathematical and Theoretical* **52.** Publisher: IOP Publishing,

334001. ISSN: 1751-8121. `https://doi.org/10.1088%2F1751-8121%2Fab2b68` (2020) (July 2019).

61. Agoritsas, E., Maimbourg, T. & Zamponi, F. Out-of-equilibrium dynamical equations of infinite-dimensional particle systems I. The isotropic case. en. *Journal of Physics A: Mathematical and Theoretical* **52.** Publisher: IOP Publishing, 144002. ISSN: 1751-8121. `https://doi.org/10.1088%2F1751-8121%2Fab099d` (2020) (Mar. 2019).

62. Olsson, P. & Teitel, S. Critical Scaling of Shear Viscosity at the Jamming Transition. *Physical Review Letters* **99,** 178001. `https://link.aps.org/doi/10.1103/PhysRevLett.99.178001` (2018) (Oct. 2007).

63. Ikeda, A., Berthier, L. & Sollich, P. Disentangling glass and jamming physics in the rheology of soft materials. en. *Soft Matter* **9,** 7669–7683. `https://pubs.rsc.org/en/content/articlelanding/2013/sm/c3sm50503k` (2019) (2013).

64. Bi, D., Lopez, J. H., Schwarz, J. M. & Manning, M. L. A density-independent rigidity transition in biological tissues. en. *Nature Physics* **11,** 1074–1079. ISSN: 1745-2481. `https://www.nature.com/articles/nphys3471` (2018) (Dec. 2015).

65. Vicsek, T., Czirók, A., Ben-Jacob, E., Cohen, I. & Shochet, O. Novel Type of Phase Transition in a System of Self-Driven Particles. *Physical Review Letters* **75.** Publisher: American Physical Society, 1226–1229. `https://link.aps.org/doi/10.1103/PhysRevLett.75.1226` (2020) (Aug. 1995).

66. Szabó, B. *et al.* Phase transition in the collective migration of tissue cells: Experiment and model. *Physical Review E* **74.** Publisher: American Physical Society, 061908. `https://link.aps.org/doi/10.1103/PhysRevE.74.061908` (2020) (Dec. 2006).

67. Bi, D., Yang, X., Marchetti, M. C. & Manning, M. L. Motility-Driven Glass and Jamming Transitions in Biological Tissues. *Physical Review X* **6,** 021011. `https://link.aps.org/doi/10.1103/PhysRevX.6.021011` (2018) (Apr. 2016).

68. Merkel, M. & Manning, M. L. A geometrically controlled rigidity transition in a model for confluent 3D tissues. en. *New Journal of Physics* **20.** Publisher: IOP Publishing, 022002. ISSN: 1367-2630. `https://doi.org/10.1088%2F1367-2630%2Faaaa13` (2020) (Feb. 2018).

69. Malandro, D. L. & Lacks, D. J. Relationships of shear-induced changes in the potential energy landscape to the mechanical properties of ductile glasses. *The Journal of Chemical Physics* **110,** 4593–4601. ISSN: 0021-9606. `https://aip.scitation.org/doi/abs/10.1063/1.478340` (2018) (Feb. 1999).

70. Maloney, C. E. & Lemaître, A. Amorphous systems in athermal, quasistatic shear. *Physical Review E* **74,** 016118. `https://link.aps.org/doi/10.1103/PhysRevE.74.016118` (July 2006).

71. Manning, M. L. & Liu, A. J. Vibrational Modes Identify Soft Spots in a Sheared Disordered Packing. *Physical Review Letters* **107.** `https://doi.org/10.1103/physrevlett.107.108302` (Aug. 2011).

72. O'Hern, C. S., Silbert, L. E., Liu, A. J. & Nagel, S. R. Jamming at zero temperature and zero applied stress: The epitome of disorder. *Physical Review E* **68.** `https://doi.org/10.1103/physreve.68.011306` (July 2003).

73. DeGiuli, E., Laversanne-Finot, A., Düring, G., Lerner, E. & Wyart, M. Effects of coordination and pressure on sound attenuation, boson peak and elasticity in amorphous solids. *Soft Matter* **10,** 5628. `https://doi.org/10.1039/c4sm00561a` (June 2014).

74. Silbert, L. E., Liu, A. J. & Nagel, S. R. Vibrations and Diverging Length Scales Near the Unjamming Transition. *Physical Review Letters* **95.** `https://doi.org/10.1103/physrevlett.95.098301` (Aug. 2005).

75. Manning, M. L. & Liu, A. J. A random matrix definition of the boson peak. *EPL (Europhysics Letters)* **109,** 36002. `https://doi.org/10.1209/0295-5075/109/36002` (Feb. 2015).

76. Mizuno, H., Shiba, H. & Ikeda, A. Continuum limit of the vibrational properties of amorphous solids. *Proceedings of the National Academy of Sciences* **114,** E9767–E9774. `https://doi.org/10.1073/pnas.1709015114` (Oct. 2017).

77. Kapteijns, G., Bouchbinder, E. & Lerner, E. *Universal non-phononic density of states in 2D, 3D and 4D glasses* 2018. eprint: `arXiv:1803.11383`.

78. Parisi, G. & Zamponi, F. Mean-field theory of hard sphere glasses and jamming. *Reviews of Modern Physics* **82,** 789–845. `https://doi.org/10.1103/revmodphys.82.789` (Mar. 2010).

79. Baity-Jesi, M., Martın-Mayor, V., Parisi, G. & Perez-Gaviro, S. Soft Modes, Localization, and Two-Level Systems in Spin Glasses. *Physical Review Letters* **115.** `https://doi.org/10.1103/physrevlett.115.267205` (Dec. 2015).

80. Wijtmans, S. & Manning, M. L. Disentangling defects and sound modes in disordered solids. *Soft Matter* **13,** 5649–5655. `https://doi.org/10.1039/c7sm00792b` (2017).

81. Tanguy, A., Mantisi, B. & Tsamados, M. Vibrational modes as a predictor for plasticity in a model glass. *EPL (Europhysics Letters)* **90,** 16004. `https://doi.org/10.1209/0295-5075/90/16004` (Apr. 2010).

82. Tsamados, M., Tanguy, A., Léonforte, F. & Barrat, J. .-.-L. On the study of local-stress rearrangements during quasi-static plastic shear of a model glass: Do local-stress components contain enough information? *The European Physical Journal E* **26,** 283–293. `https://doi.org/10.1140/epje/i2007-10324-y` (May 2008).

83. Ashton, D. J. & Garrahan, J. P. Relationship between vibrations and dynamical heterogeneity in a model glass former: Extended soft modes but local relaxation. *The European Physical Journal E* **30.** `https://doi.org/10.1140/epje/i2009-10531-6` (Oct. 2009).

84. Brito, C. & Wyart, M. Heterogeneous dynamics, marginal stability and soft modes in hard sphere glasses. *Journal of Statistical Mechanics: Theory and Experiment* **2007,** L08003–L08003. `https://doi.org/10.1088/1742-5468/2007/08/l08003` (Aug. 2007).

85. Mehta, M. *Random Matrices* ISBN: 9780080474113. `https://books.google.com/books?id=Kp3Nx03%5C_gMwC` (Elsevier Science, 2004).

86. Parisi, G. Euclidean random matrices, the glass transition and the boson peak. *The European Physical Journal E - Soft Matter* **9,** 213–218. `https://doi.org/10.1140/epje/i2002-10088-x` (Nov. 2002).

87. Gurarie, V. & Chalker, J. T. Bosonic excitations in random media. *Physical Review B* **68.** `https://doi.org/10.1103/physrevb.68.134207` (Oct. 2003).

88. Merris, R. Laplacian matrices of graphs: a survey. *Linear Algebra and its Applications* **197-198,** 143–176. `https://doi.org/10.1016/0024-3795(94)90486-3` (Jan. 1994).

89. Aspelmeier, T. & Zippelius, A. The Integrated Density of States of the Random Graph Laplacian. *Journal of Statistical Physics* **144,** 759–773. `https://doi.org/10.1007/s10955-011-0271-2` (July 2011).

90. Cicuta, G. M., Krausser, J., Milkus, R. & Zaccone, A. Unifying model for random matrix theory in arbitrary space dimensions. *Physical Review E* **97.** `https://doi.org/10.1103/physreve.97.032113` (Mar. 2018).

91. Xu, N., Vitelli, V., Liu, A. J. & Nagel, S. R. Anharmonic and quasi-localized vibrations in jammed solids—Modes for mechanical failure. *EPL (Europhysics Letters)* **90,** 56001. `https://doi.org/10.1209/0295-5075/90/56001` (June 2010).

92. Ellenbroek, W. G. *Response of Granular Media near the Jamming Transition* ISBN: 9789085930297 (Leiden Institute of Physics, Institute-Lorentz for Theoretical Physics, Faculty of Science, Leiden University, 2007).

93. Lerner, E. & Bouchbinder, E. Frustration-induced internal stresses are responsible for quasilocalized modes in structural glasses. *Physical Review E* **97.** `https://doi.org/10.1103/physreve.97.032140` (Mar. 2018).

94. Benetti, F. P. C., Parisi, G., Pietracaprina, F. & Sicuro, G. *Mean-field model for the density of states of jammed soft spheres* 2018. eprint: `arXiv:1804.02705`.

95. Dyson, F. J. The Dynamics of a Disordered Linear Chain. *Physical Review* **92,** 1331–1338. `https://doi.org/10.1103/physrev.92.1331` (Dec. 1953).

96. Dean, P. Vibrations of glass-like disordered chains. *Proceedings of the Physical Society* **84,** 727–744. `https://doi.org/10.1088/0370-1328/84/5/310` (Nov. 1964).

97. Facoetti, D., Vivo, P. & Biroli, G. From non-ergodic eigenvectors to local resolvent statistics and back: A random matrix perspective. *EPL (Europhysics Letters)* **115,** 47003. `https://doi.org/10.1209/0295-5075/115/47003` (Aug. 2016).

98. Gentle, J. E. *Computational Statistics (Statistics and Computing)* (Springer, 2009).

99. Camazine, S. *et al. Self-organization in biological systems* (Princeton university press, 2003).

100. Helbing, D., Johansson, A. & Al-Abideen, H. Z. Dynamics of crowd disasters: An empirical study. *Physical review E* **75,** 046109 (2007).

101. Sumpter, D. J. *Collective animal behavior* (Princeton University Press, 2010).

102. Vicsek, T. & Zafeiris, A. Collective motion. *Physics Reports* **517,** 71–140. `https://doi.org/10.1016/j.physrep.2012.03.004` (Aug. 2012).

103. Bricard, A., Caussin, J.-B., Desreumaux, N., Dauchot, O. & Bartolo, D. Emergence of macroscopic directed motion in populations of motile colloids. *Nature* **503,** 95–98. `https://doi.org/10.1038/nature12673` (Nov. 2013).

104. Silverberg, J. L., Bierbaum, M., Sethna, J. P. & Cohen, I. Collective motion of humans in mosh and circle pits at heavy metal concerts. *Physical review letters* **110,** 228701 (2013).

105. Murino, V., Cristani, M., Shah, S. & Savarese, S. *Group and crowd behavior for computer vision* (Academic Press, 2017).

106. Moussaid, M., Helbing, D. & Theraulaz, G. How simple rules determine pedestrian behavior and crowd disasters. *Proceedings of the National Academy of Sciences* **108,** 6884–6888. `https://doi.org/10.1073/pnas.1016507108` (Apr. 2011).

107. Vicsek, T., Czirók, A., Ben-Jacob, E., Cohen, I. & Shochet, O. Novel type of phase transition in a system of self-driven particles. *Physical review letters* **75,** 1226 (1995).

108. Helbing, D. & Molnár, P. Social force model for pedestrian dynamics. *Physical Review E* **51,** 4282–4286. `https://doi.org/10.1103/physreve.51.4282` (May 1995).

109. Duives, D. C., Daamen, W. & Hoogendoorn, S. P. State-of-the-art crowd motion simulation models. *Transportation Research Part C: Emerging Technologies* **37,** 193–209. `https://doi.org/10.1016/j.trc.2013.02.005` (Dec. 2013).

110. Bezain, L. *Stadium stampede in Madagascar's capital kills 15, wounds 80* June 2019. `https://abcnews.go.com/International/wireStory/stadium-stampede-madagascars-capital-kills-15-wounds-80-63965681`.

111. Henkes, S., Brito, C. & Dauchot, O. Extracting vibrational modes from fluctuations: a pedagogical discussion. *Soft Matter* **8,** 6092–6109 (2012).

112. Cubuk, E. *et al.* Identifying Structural Flow Defects in Disordered Solids Using Machine-Learning Methods. *Physical Review Letters* **114.** `https://doi.org/10.1103/physrevlett.114.108001` (Mar. 2015).

113. Richard, D. *et al.* Predicting plasticity in disordered solids from structural indicators (Feb. 2020).

114. Ellenbroek, W. G. *et al. Response of granular media near the jamming transition* (Leiden Institute of Physics, Institute-Lorentz for Theoretical Physics, Faculty of Science, Leiden University, 2007).

115. Johnson, K. L. & Johnson, K. L. *Contact mechanics* (Cambridge university press, 1987).

116. Merriam, J. Atmospheric pressure and gravity. *Geophysical Journal International* **109,** 488–500 (1992).

117. Tong, H., Hu, H., Tan, P., Xu, N. & Tanaka, H. Revealing Inherent Structural Characteristics of Jammed Particulate Packings. *Physical review letters* **122,** 215502 (2019).

118. Sussman, D. M., Schoenholz, S. S., Cubuk, E. D. & Liu, A. J. Disconnecting structure and dynamics in glassy thin films. *Proceedings of the National Academy of Sciences* **114,** 10601–10605. `https://doi.org/10.1073/pnas.1703927114` (Sept. 2017).

119. SCHUH, C., HUFNAGEL, T. & RAMAMURTY, U. Mechanical behavior of amorphous alloys. *Acta Materialia* **55,** 4067–4109. `https://doi.org/10.1016/j.actamat.2007.01.052` (July 2007).

120. Schall, P., Weitz, D. A. & Spaepen, F. Structural rearrangements that govern flow in colloidal glasses. *Science* **318,** 1895–1899 (2007).

121. Lauridsen, J., Twardos, M. & Dennin, M. Shear-Induced Stress Relaxation in a Two-Dimensional Wet Foam. *Physical Review Letters* **89.** `https://doi.org/10.1103/physrevlett.89.098303` (Aug. 2002).

122. Bonn, D., Denn, M. M., Berthier, L., Divoux, T. & Manneville, S. Yield stress materials in soft condensed matter. *Reviews of Modern Physics* **89.** `https://doi.org/10.1103/revmodphys.89.035005` (Aug. 2017).

123. Zhang, Y. & Greer, A. L. Thickness of shear bands in metallic glasses. *Applied Physics Letters* **89,** 071907. `https://doi.org/10.1063/1.2336598` (Aug. 2006).

124. Maloney, C. E. & Lemaıtre, A. Amorphous systems in athermal, quasistatic shear. *Physical Review E* **74.** `https://doi.org/10.1103/physreve.74.016118` (July 2006).

125. Nicolas, A., Ferrero, E. E., Martens, K. & Barrat, J.-L. Deformation and flow of amorphous solids: Insights from elastoplastic models. *Reviews of Modern Physics* **90.** `https://doi.org/10.1103/revmodphys.90.045006` (Dec. 2018).

126. Lemaıtre, A. & Caroli, C. Rate-Dependent Avalanche Size in Athermally Sheared Amorphous Solids. *Physical Review Letters* **103.** `https://doi.org/10.1103/physrevlett.103.065501` (Aug. 2009).

127. Salerno, K. M., Maloney, C. E. & Robbins, M. O. Avalanches in Strained Amorphous Solids: Does Inertia Destroy Critical Behavior? *Physical Review Letters* **109.** `https://doi.org/10.1103/physrevlett.109.105703` (Sept. 2012).

128. Nicolas, A., Ferrero, E. E., Martens, K. & Barrat, J.-L. Deformation and flow of amorphous solids: An updated review of mesoscale elastoplastic models. eprint: `arXiv:1708.09194` (2017).

129. Ozawa, M., Berthier, L., Biroli, G., Rosso, A. & Tarjus, G. Random critical point separates brittle and ductile yielding transitions in amorphous materials. *Proceedings*

of the National Academy of Sciences **115,** 6656–6661. `https://doi.org/10.1073/pnas.1806156115` (June 2018).

130. Popović, M., de Geus, T. W. J. & Wyart, M. Elastoplastic description of sudden failure in athermal amorphous materials during quasistatic loading. *Physical Review E* **98.** `https://doi.org/10.1103/physreve.98.040901` (Oct. 2018).

131. Jaiswal, P. K., Procaccia, I., Rainone, C. & Singh, M. Mechanical yield in amorphous solids: A first-order phase transition. *Physical review letters* **116,** 085501 (2016).

132. Shrivastav, G. P., Chaudhuri, P. & Horbach, J. Yielding of glass under shear: A directed percolation transition precedes shear-band formation. *Physical Review E* **94,** 042605 (2016).

133. Ghosh, A. *et al.* Direct observation of percolation in the yielding transition of colloidal glasses. *Physical review letters* **118,** 148001 (2017).

134. Barlow, H. J., Cochran, J. O. & Fielding, S. M. *From ductile to brittle yielding in amorphous materials* 2019. eprint: `arXiv:1912.07457`.

135. Kocks, U. The relation between polycrystal deformation and single-crystal deformation. *Metallurgical and Materials Transactions B* **1,** 1121–1143 (1970).

136. Zylberg, J., Lerner, E., Bar-Sinai, Y. & Bouchbinder, E. Thermal energy as structural indicator in glasses: From universal anomalous statistics to predicting plastic rearrangements. *arXiv preprint arXiv:1703.09014* (2017).

137. Ding, J., Patinet, S., Falk, M. L., Cheng, Y. & Ma, E. Soft spots and their structural signature in a metallic glass. *Proceedings of the National Academy of Sciences* **111,** 14052–14056. `https://doi.org/10.1073/pnas.1412095111` (Sept. 2014).

138. Bitzek, E., Koskinen, P., Gähler, F., Moseler, M. & Gumbsch, P. Structural Relaxation Made Simple. *Physical Review Letters* **97.** `https://doi.org/10.1103/physrevlett.97.170201` (Oct. 2006).

139. Edelsbrunner, H. & Harer, J. *Persistent homology—a survey* 2008. `https://doi.org/10.1090/conm/453/08802`.

140. White, J., Steingold, S. & Fournelle, C. Performance metrics for group-detection algorithms. *Proceedings of Interface 2004* (2004).

Vita

Title of Dissertation

Investigating the Relationships Between Disorder, Structure, and Dynamics in Amorphous Systems

Full Name

Ethan Stanifer

Place and Date of Birth

Hamilton, Ohio April 18, 1991

Colleges and Universities	Years attended and degrees
Miami University	2009-2013 B.S, B.S., B.A.
Syracuse University	2014-2020 M.S., Ph.D.

Major Department

Physics